NUREG/CR-2424
PNL-5088-1
Vol. 1

Mathematical Simulation of Sediment and Radionuclide Transport in Coastal Waters

Vol. 1: Testing of the Sediment/Radionuclide Transport Model, FETRA

Prepared by Y. Onishi, F. L. Thompson

Pacific Northwest Laboratory

Prepared for
U.S. Nuclear Regulatory Commission

GPO Printed copy price: $5.00

NUREG/CR--2424-Vol.1

DE84 013535

Mathematical Simulation of Sediment and Radionuclide Transport in Coastal Waters

Vol. 1: Testing of the Sediment/Radionuclide Transport Model, FETRA

Manuscript Completed: April 1984
Date Published: May 1984

Prepared by
Y. Onishi, F. L. Thompson

Pacific Northwest Laboratory
Richland, WA 99352

Prepared for
Division of Health, Siting and Waste Management
Office of Nuclear Regulatory Research
U.S. Nuclear Regulatory Commission
Washington, D.C. 20555
NRC FIN B2271

GPO Printed copy price: 500

ABSTRACT

The finite element model, FETRA, is an unsteady, two-dimensional (longitudinal and lateral) model for simulating the transport of sediment and contaminants (e.g., radionuclides, heavy metals, pesticides) in coastal waters. FETRA includes major transport and fate mechanisms explicitly, including sediment/contaminant interactions. The purpose of the study was to test FETRA model with available field data and was not intended to assess the potential impact of the Windscale Nuclear Fuel Reprocessing Plant on the Irish Sea. The model was tested by applying it to the Irish Sea to simulate wind-generated waves and the migration of sediment and ^{137}Cs. The model predicted distributions of suspended sand; suspended silt; suspended clay; ^{137}Cs sorbed by each of the three sizes of suspended sediments; dissolved ^{137}Cs; bed sediment size fractions; and ^{137}Cs sorbed by bed sand, bed silt, and bed clay over a two-month period in 1974.

During 1974, the rate of ^{137}Cs release from the plant was about five times greater than that during 1973. Because of this large increase, we used this particular period for the simulation. However, available field data for the period were not complete enough to define the initial conditions for the simulation. Therefore, we assumed that no contamination existed at the beginning of the simulation period, and model predictions were compared with the incremental difference between dissolved ^{137}Cs concentrations measured in 1973 and 1974. FETRA predicted that approximately 82%, 0.002%, and 18% of the total ^{137}Cs remaining in this study area were dissolved, suspended sediment-sorbed, and bed-sediment-sorbed radionuclides, respectively. Past measurement of ^{137}Cs in the study area showed that over 80% of the total ^{137}Cs was in the dissolved form.

Although many of the necessary field data (especially raw field data) were not available to us for validating the model, FETRA nonetheless generally predicted reasonable migration patterns for the sediments and ^{137}Cs. The prediction of ^{137}Cs distributions can be further improved by using a finer grid near the radionuclide release point. The study results indicate that FETRA can simulate the complex phenomena involved in sediment and contaminant transport in coastal waters. However, we recommend that FETRA be tested further at other field sites where the necessary field data are available to validate the model.

Detailed laboratory flume testing should be conducted to study cohesive sediment transport, deposition, and erosion. Our current lack of understanding of these phenomena is one of the major factors in hindering the accurate prediction of the migration of radionuclides sorbed by fine sediments (silt and clay). We also recommend that FETRA be coupled with a geochemical model to better handle adsorption and precipitation mechanisms.

CONTENTS

FIGURES

TABLES

ACKNOWLEDGMENTS

Volumes 1 and 2 of this report summarize the results of research performed by Pacific Northwest Laboratory for the U.S. Nuclear Regulatory Commission on "Mathematical Simulation of Sediment and Radionuclide Transport in Coastal Waters". The authors wish to acknowledge the guidance and patience provided by Dr. Phillip R. Reed of the U.S. Nuclear Regulatory Commission.

The authors also express their gratitude to the United Kingdom's Fisheries Radiobiological Laboratory, in the Ministry of Agriculture, for supplying available published reports on the Irish Sea.

SUMMARY

The ultimate goal of this study was to provide the U.S. Nuclear Regulatory Commission with a site assessment tool to accurately predict radionuclide transport, deposition, and erosion in coastal waters. To achieve this goal, Pacific Northwest Laboratory (PNL) applied the FETRA model and the hydrodynamic model, CAFE, to the Irish Sea. The Irish Sea was selected because coastal current, sediment, and radionuclide distributions have been extensively monitored. The purpose of the study was to test FETRA model with available field data and was not intended to assess the potential impact of the Windscale Nuclear Fuel Reprocessing Plant on the Irish Sea.

The finite element sediment/contaminant transport model, FETRA, was modified to include the wave mechanisms that suspend marine sediment. FETRA is an unsteady, two-dimensional (longitudinal and lateral) model and consists of three submodels that simulate the sediment/contaminant interactions. These submodels simulate 1) sediment transport for three sediment size fractions, 2) dissolved contaminant transport, and 3) particulate (those sorbed by sediment) contaminant transport associated with the three sediment size fractions.

During 1974, the rate of ^{137}Cs release from the plant was about five times greater than that during 1973. Because of this large increase, we used this particular period for the simulation. However, available field data for the period were not complete enough to define the initial conditions for the simulation. Therefore, we assumed that no contamination existed at the beginning of the simulation period, and model predictions were compared with the incremental difference between dissolved ^{137}Cs concentrations measured in 1973 and 1974. FETRA simulated wind-generated waves; transport of sand, silt, and clay; dissolved ^{137}Cs transport; and transport and accumulation of ^{137}Cs sorbed by sand, silt, and clay for 62.5 days. The model predicted that approximately 82%, 0.002%, and 18% of the total ^{137}Cs remaining in the Irish Sea study area were dissolved, suspended-sediment-sorbed, and bed-sediment-sorbed radionuclides, respectively. Past measurement of ^{137}Cs in the study area showed that over 80% of the total ^{137}Cs was in the dissolved form.

In the hydrodynamic modeling using CAFE, we compared simulated and observed general flow patterns and simulated and observed velocity ellipses; in the latter comparison, we focused on the amplitude, direction, and phase of the maximum flood and ebb currents. The CAFE results for the calibration period showed good agreement with the general circulation pattern and showed reasonable agreement with flow velocities. To improve our hydrodynamic model results, we would probably need to 1) use a finer grid, and 2) investigate more fully how changes in the boundary conditions would affect the flow field.

Although many of the necessary field data, especially raw field data (such as distributions of suspended sediment concentrations and their size fractions, and distributions of ^{137}Cs sorbed by suspended and bed sediment), were not available to us to validate the FETRA model, we could still evaluate FETRA's behavior under a fairly realistic environment for the Irish Sea.

In general, FETRA predicted reasonable migration patterns for the sediment and radionuclides, demonstrating a capability to simulate the complex phenomena of sediment and radionuclide transport in coastal waters. Note that the FETRA model is general enough to also simulate the transport of other contaminants (e.g., heavy metals, pesticides, and other toxic chemical compounds).

We recommend that

- FETRA be applied to other sites where the field data necessary to validate the model are available
- FETRA be coupled to a geochemical model to improve its handling of adsorption and precipitation of radionuclides
- FETRA's capability to simulate marine sand transport by waves be further improved
- laboratory hydraulic-flume testing be performed to carefully investigate the mechanisms of transport, deposition, and erosion of fine sediments of silt and clay.

1.0 INTRODUCTION

Many nuclear facilities release radionuclides into costal waters under normal and accidental conditions. To assess the potential dangers that these radionuclides may pose to the environment and humans, the migration and fate of these radionuclides in costal waters must be determined. The distributions of radionuclides in coastal waters are controlled by the following transport/transformation processes:

- radionuclide transport resulting from
  - water movement caused by coastal currents, wind shear, and surface waves
  - sediment movements caused by coastal currents and surface waves
  - bioturbation
- radionuclide intermedia transfer resulting from
  - adsorption/desorption
  - precipitation/dissolution
  - volatilization (if applicable)
- radionuclide decay
- radionuclide transformation resulting from
  - yield of radionuclide decay products

If a coastal water has very small concentrations of fine sediments, then for radionuclides with no or low affinity to sediment (e.g., ^{3}H and ^{90}Sr), the most important transport mechanism is the water movement. However, for radionuclides with high affinity to sediment, we must also consider the radionuclide adsorption to the sediment, and thus sediment transport affected by both coastal currents and surface waves must be considered (Noshkin and Bowen 1973; Nevissi and Schell 1974; Livingston and Bowen 1976; Schell 1977). This is especially true if a coastal water has high concentrations of suspended fine sediments and/or a high fraction of fine sediments in the sea bed.

Measurements conducted in the Irish Sea near the Windscale Nuclear Fuel Reprocessing Plant in England indicate that approximately 95% of ^{239}Pu discharged from the plant to the Irish Sea was adsorbed by marine sediment and only 5% remained in solution in sea water (Hetherington 1976). Plutonium sorbed onto bed sediment then becomes a long-term source of contamination. These data also revealed that ^{106}Ru and ^{144}Ce behave in a manner similar to ^{239}Pu. Hetherington (1976) further reported that subsequent deposition of radioactively contaminated suspended sediment to the sea bed is the major factor causing the accumulation of radionuclides in the Irish Sea bed.

Schell (1977) reported that in the near coastal waters of Washington State more than 75% of ^{210}Pb present is associated with sediments. Furthermore, Schell mentioned that ^{210}Po is also generally found in the sediments of Washington State coastal waters.

Historically, contaminant (e.g., radionuclides, heavy metals) transport modeling in coastal waters has been performed without considering nonaqueous forms of contaminants (Leenderste 1970; Leenderste et al 1973; Eraslan 1975, 1977). Although a contaminant may be substantially precipitated or sorbed to a solid matrix, the aqueous-only modeling approach remains popular because it is much simpler and in many cases predicts conservative concentrations of dissolved contaminants. However, recent concern about the accumulation of contaminants in the environment as well as general demands for more accurate predictions has prompted the development and testing of more sophisticated surface water contaminant transport models (Onishi et al. 1982; Onishi and Trent 1982).

FETRA (the Finite Element Transport Model), a computer program for sediment/contaminant (e.g., radionuclides, pesticides, heavy metals) transport was developed in response to the need for a site assessment methodology that realistically addresses the governing mechanisms of contaminant transport and fate in surface waters (Onishi 1981; Onishi et al. 1979). FETRA uses the finite element computational method to produce time-varying longitudinal and lateral distributions of sediments and contaminants using three coupled submodels. The following three coupled submodels describe sediment/contaminant interactions:

- a sediment transport submodel
- a dissolved contaminant transport submodel
- a particulate (sediment-sorbed) contaminant transport submodel.

The FETRA model was tested by

- numerical experiments to solve problems with known analytical solutions for comparison
- checking mass balance
- applying the model in the field.

To field test the model, FETRA was applied to the Irish Sea to simulate surface waves generated by wind, sediment transport affected by the flows and waves, dissolved ^{137}Cs, and particulate (sediment-sorbed) ^{137}Cs in water columns and the sea bed over a two-month period of 1974. The hydrodynamic input data required by FETRA was obtained from a compatible finite element hydrodynamic model, CAFE (Wang and Connor 1975).

This report discusses the performance testing of FETRA. Conclusions and recommendations are presented in Chapter 2. Chapter 3 provides the FETRA model description and Chapter 4 discusses the simulation results from the application of FETRA and CAFE to the Irish Sea. Volume 2 of this report contains a brief user's guide and a program listing for FETRA.

2.0 CONCLUSIONS AND RECOMMENDATIONS

The sediment/contaminant transport model, FETRA is undergoing model application tests prior to its distribution as a site assessment tool. The application of FETRA to the Irish Sea study area is intended to test its capabilities.

Although the Irish Sea has been extensively monitored for distributions of current, sediment, and radionuclides, we were not able to obtain much of the field data (especially raw field data) necessary to validate the model. Hence, this study focuses on evaluating the behavior of FETRA under reasonably realistic conditions for the Irish Sea.

2.1 CONCLUSIONS

FETRA generally predicts reasonable distribution patterns of sand, silt, clay, dissolved ^{137}Cs, and ^{137}Cs sorbed by sand, silt, and clay in the Irish Sea as influenced by tides and wind. However, there is some discrepancy between the predicted dissolved ^{137}Cs distribution and that estimated from the measured ^{137}Cs distribution. The model predicted that approximately 82% and 0.002% of the total ^{137}Cs remained in the Irish Sea study area as dissolved radionuclides and suspended-sediment-sorbed radionuclides, respectively, while approximately 18% remained in the bed sorbed on bed sediments. The model predicted much lower radionuclide concentrations in the vicinity of the radionuclide release point than measured concentrations. This is attributed to the use of a coarse finite element grid near the source. Better predictions of radionuclide distribution can be achieved by using a finer grid near the radionuclide release point. The simulation results indicate that FETRA can simulate the complex phenomena involved in radionuclide migration in coastal waters. The model is general enough to also simulate transport of other contaminants, such as heavy metals, pesticides, or toxic chemical compounds.

2.2 RECOMMENDATIONS

We recommend that

1. FETRA be applied to at least one more field site where the necessary field data are available to validate the model

2. a geochemical model be coupled with FETRA, so that adsorption and precipitation are more accurately estimated to produce a better prediction of radionuclide distributions

3. FETRA's capability to simulate marine sand transport affected by surface waves be further tested

4. carefully controlled laboratory flume testing be conducted to improve the current understanding of cohesive sediment transport, deposition and erosion. The current lack of understanding of these basic phenomena prohibits a reliable prediction of sediment-sorbed radionuclides, thus also affecting the prediction of dissolved radionuclides in surface waters.

3.0 MODEL DESCRIPTION OF FETRA

FETRA is an unsteady, two-dimensional model that uses the finite element computation method with the Galerkin-weighted residual technique (Onishi 1981). The following three submodels were coupled to account for the sediment/contaminant interactions: 1) a sediment transport submodel; 2) a dissolved contaminant transport submodel; and 3) a particulate contaminant transport submodel. (Particulate contaminants are those adsorbed by sediments.)

The following is the description of the modified model.

3.1 SEDIMENT TRANSPORT SUBMODEL

Important sediment characteristics such as fall velocity, critical shear stresses of erosion and deposition, and adsorption capacity vary significantly with sediment sizes and types. Accordingly, sediment movements and particulate contaminant transport are modeled separately for each sediment size fraction or sediment type. (FETRA currently handles three sediment size fractions or sediment types.) The sediment transport submodel includes the mechanisms of

1. advection and diffusion/dispersion of sediments
2. fall velocity and cohesiveness
3. deposition on the sea bed or riverbed
4. erosion from the sea bed or riverbed (bed erosion and armoring)
5. sediment contributions from point/nonpoint sources and subsequent mixing.

Sediment mineralogy and water quality effects are implicitly included in Items 2, 3, and 4 above. This submodel also calculates the changes in the ocean bed or riverbed conditions, including bed elevation changes that result from scouring or deposition or both, and three-dimensional distribution of sediment sizes within the bed.

The governing equation of the vertically averaged, two-dimensional sediment transport for jth sediment size fraction or sediment type was obtained from the following three-dimensional mass conservation equation (Daily and Harelmann 1966; Sayre 1966):

$$\frac{\partial C_j}{\partial t} + \frac{\partial}{\partial x}(UC_j) + \frac{\partial}{\partial y}(VC_j) + \frac{\partial}{\partial z}(W - W_{sj})\,C_j = \frac{\partial}{\partial x}\left(\varepsilon_x \frac{\partial C_j}{\partial x}\right) + \frac{\partial}{\partial y}\left(\varepsilon_y \frac{\partial C_j}{\partial y}\right) + \frac{\partial}{\partial z}\left(\varepsilon_z \frac{\partial C_z}{\partial z}\right) + Q_{sj} \quad (1)$$

where

C_j = concentration of sediment of jth size fraction, (weight of sediment per unit volume of water)
Q_{sj} = source strength of jth sediment contribution
t = time
U = velocity component of longitudinal (x) direction
V = velocity component of lateral (y) direction
W = velocity component of vertical (z) direction
W_{sj} = fall velocity of sediment particle of jth size fraction or type
x,y,z, = longitudinal, lateral, and vertical directions in Cartesian coordinates, respectively, and
$\epsilon_x,\epsilon_y,\epsilon_z$ = diffusion coefficients of longitudinal, lateral, and vertical directions.

The boundary conditions were

$$(W - W_{sj})\, C_j - \epsilon_z \frac{\partial C_j}{\partial z} = 0 \qquad \text{at } z = h \qquad (2)$$

$$(1 - \gamma)\, W_{sj}\, C_j + \epsilon_z \frac{\partial C_j}{\partial z} = S_{Dj} - S_{Rj} \qquad \text{at } z = 0 \qquad (3)$$

$$VC_j - \epsilon_y \frac{\partial C_j}{\partial y} = q_{sj} \quad \text{or} \quad C_j = C_{jo} \qquad \text{at } y = 0 \text{ and } B \qquad (4)$$

where

B = width of the river
C_{jo} = constant concentration of jth sediment
h = depth
S_{Dj} = sediment deposition rate per unit bed surface area for jth sediment size
S_{Rj} = sediment erosion rate per unit bed surface area for jth sediment size
γ = coefficient, i.e., probability that particle settling to the bed is re-entrained, and
q_{sj} = lateral influx of jth sediment.

The vertical flow velocity, W, was assumed to be negligible.

Equation (1) was vertically integrated to obtain the two-dimensional sediment-transport equation. Since velocity components and sediment concentration are generally not uniform vertically, we used the following approach similar to the one used by Fischer (1967).

$$C_j = \overline{C}_j + c_j'' \qquad (5)$$

$$U = \overline{U} + u" \tag{6}$$

$$V = \overline{V} + v" \tag{7}$$

$$\frac{\partial W_{sj}}{\partial z} = 0 \tag{8}$$

in which $\overline{C}_j, \overline{U}, \overline{V}$ = depth averaged values of concentration of jth sediment, longitudinal velocity, and lateral velocity, respectively; and c",u",v" = fluctuations from the depth averaged values of concentration of jth sediment, longitudinal velocity, and lateral velocity, respectively. Note that c",u", and v" are spatial deviations, not temporal deviations as are usual in turbulence analysis; all of the temporal averaging has been carried out before writing Equation (1).

As in the Boussinesq diffusion coefficient concept let

$$\int_0^h u"c"_j \, dz = (\overline{u"c"_j})\, h = -hD_x \frac{\partial \overline{C}_j}{\partial x} \tag{9}$$

and

$$\int_0^h v"c"_j \, dz = (\overline{v"c"_j})\, h = -hD_y \frac{\partial \overline{C}_j}{\partial y} \tag{10}$$

in which D_x and D_y = the dispersion coefficients of x and y directions.

The dispersion coefficients of x and y directions were assumed to be the same for all sediments and contaminants. Noting the equation of continuity, the kinetic water surface boundary condition, and Equations (2), (3), (9), and (10), the following final expression of sediment transport was obtained by substituting the aforementioned expressions into Equation (1) and by integrating Equation (1) over the entire river depth:

$$h\frac{\partial \overline{C}_j}{\partial t} + hU\frac{\partial \overline{C}_j}{\partial x} + hV\frac{\partial \overline{C}_j}{\partial y} = \frac{\partial}{\partial x}\left(K_x h \frac{\partial \overline{C}_j}{\partial x}\right) + \frac{\partial}{\partial y}\left(K_y h \frac{\partial \overline{C}_i}{\partial y}\right)$$

$$+ hQ_\ell \overline{C}_j + (S_{Rj} - S_{Dj} + Q_{sj}h) \tag{11}$$

where

$K_x = \varepsilon_x + D_x \simeq D_x$
$K_y = \varepsilon_y + D_y \simeq D_y$
Q_ℓ = lateral flux of flow

The finite element method was used to solve Equations (4) and (11). To solve these equations, sediment erosion and deposition rates, S_{Rj} and S_{Dj}, must be evaluated for each sediment-size fraction in various water bodies. These rates were calculated separately for surface water bodies with and without wave, as discussed below.

3.1.1 Coastal Waters with Surface Waves

In most environments occurring in coastal areas, marine sediments are mostly suspended by waves, which themselves can transport only small amounts of suspended sediment. The sediment suspended by wave action is then transported mostly by a current that usually is too small to suspend sediment by itself.

The following concept was used to compute the erosion and deposition rates of noncohesive sediment in this case. If the amount of sand being transported is less than what the flow and wave can carry, the current and waves will scour sediment from the sea bed to increase the sediment transport rate. The scouring takes place until an actual sediment load is equal to the carrying capacity of the flow and waves, or until the available bed sediments are all scoured, whichever occurs first. Conversely, the flow deposits sand if its actual sediment load is above the flow and wave capacity to carry sediment.

When surface waves are present, wave motion is assumed to be a dominant mechanism for suspension of sediment, which is then transported by a combination of an ambient velocity of incidental flow (those other than ones included by wave motion) and the second-order velocity components of waves. Hence, if the total sediment capacity per unit width at a down-current point is Q_T and an actual amount of sand being transported in the coastal water per unit width at an up-current point is Q_{TA}, then

$$S_{Rj} = \frac{Q_T - Q_{TA}}{\Delta L} \tag{12}$$

$$S_{Dj} = \frac{Q_{TA} - Q_T}{\Delta L} \tag{13}$$

in which ΔL = distance between the up-current and down-current locations and Q_{TA} = is obtained as a product of sand concentration and a flow rate per unit width.

Because formulations are not available to calculate rates of cohesive sediment (e.g., silt and clay) erosion and deposition by waves, the following formulas developed by Partheniades (1962) and Krone (1962) were used:

$$S_{Rj} = M_j \left(\frac{\tau_b}{\tau_{cRj}} - 1 \right) \tag{14}$$

$$S_{Rj} = W_{sj} C_j \left(1 - \frac{\tau_b}{\tau_{cDj}}\right) \tag{15}$$

in which M_j = erodibility coefficient for jth sediment; τ_{cDj} = critical shear stress for sediment deposition for jth sediment; and τ_{cRj} = critical shear stress for sediment erosion for jth sediment. Since these two formulas were originally developed for estuaries and have not been tested in coastal zones, M, τ_{cDj} and τ_{cRj} in Equations (14) and (15) must be selected with great care through model calibration. Similar to erosion of sand, cohesive sediment will be eroded with the rate of S_{Rj} or until all the available cohesive sediment in the bed is scoured, whichever results in a smaller amount of eroded sediment.

Some studies (Dawson 1978; EPA 1978) reveal that because of its large adsorption capacity, organic matter is a very important carrier of contaminants. Unfortunately, there have not been enough studies to quantify the rates of transport, deposition, and erosion of organic materials when these materials are transported other than by attaching to cohesive sediments. Since the mechanisms governing the erosion and deposition of organic matter are somewhat similar to those for cohesive sediments, Equations (14) and (15) were also used to solve for the erosion and deposition rates of organic matter. The selection of the values of W_{sj}, M_j, τ_{cDj} and τ_{cRj} in Equations (14) and (15) should reflect the characteristics of these materials in terms of their density, size, cohesiveness, and consolidation.

Offshore Zone. With the wave energy spectrum as a starting point, results obtained by Einstein (1972) and Liang and Wang (1973) were used to obtain the wave-induced noncohesive sediment suspension in offshore zones through calculation of Q_{TA} in Equation (12). Both the wave-induced bed load and suspended sediment concentrations are calculated. For the bed load, the following approach was used: the probability that a sediment particle is set into motion is the same as the probability that the instantaneous lift on the particle is greater than its submerged weight. This probability, denoted by p, is given as follows (Liang and Wang 1973):

$$p = \frac{1}{\sqrt{2\pi}} \int_{B^*\psi}^{\infty} e^{-z^2/2} dz \qquad -1/\zeta_o \tag{16}$$

where

$$\psi = \frac{(\rho_s - \rho)}{\rho u^{-2}} gD$$

$B^* = 4$

$1/\zeta_o = 1.5$

ρ_s = sediment density

ρ = water density

γ_s = unit weight of sediment

g = gravitational acceleration
D = equivalent sediment-particle diameter
$\overline{u}$ = average horizontal velocity in the boundary layer.

The average bed concentration, C_o, is given by the following equation

$$\overline{C}_o = A_o p \gamma_s \tag{17}$$

where A_o is a constant that must be determined by experiment. Thus, with a known A_o value, C_o can be calculated if $\overline{u}$ is also known (see the expression for ψ).

The velocity $\overline{u}$ is obtained by treating the flow field in the turbulent boundary layer as a superposition of all the components in the random wave train. Thus, $\overline{u}^2$ can be written as

$$\overline{u}^2 = \sum_i (u_{oi}^2)\ (1 - 2\ f_{1i}\ \cos\ f_{2i} + f_{1i}^2) \tag{18}$$

where

$$f_{1i} = 0.5 \exp \frac{[-133 \sinh (k_i h)\ z]}{a_i \beta_i D}$$

$f_{2i} = 0.3\ (\beta_i z)$

$\beta_i = \frac{\omega_i}{2\nu}$

a_i = wave amplitude
ω_i = wave frequency (rad/sec)
h = water depth
k_i = wave number
z = vertical coordinate
$u_{oi} = a_i \omega_i / \sinh (k_i h)$
ν = kinematic viscosity of water.

The average bed load transport Q_B is obtained by integrating as follows:

$$Q_B = \overline{C}_o \int_0^{2D} (U_B + U_{AB})\ dz \tag{19}$$

where

U_{AB} = velocity component of incidental flow (those other than ones induced by a wave action) near the ocean bed

U_B = mass transport velocity (second-order velocity components) of a wave near the ocean bed.

U_B is calculated by an expression obtained by Liang and Wang (1973). The distribution of vertical velocity, U_{AB} of the incidental flow is assumed to follow the 1/7-th-power law (Schlichting 1968). Hence, the bed load is transported by both wave-induced velocity and the incidental flow.

The suspended sediment concentration at elevation, z, with no depth restriction is given by Liang and Wang (1973).

$$\frac{C}{\overline{C}_o} = \left[\frac{\tanh\ (kz/2)}{\tanh\ (kz_o/2)}\right]^{R_i} , \qquad z_o = 2D \tag{20}$$

$$R_i = \frac{W_s \sinh k_i h}{\gamma\sigma\ k_i\ a_i\ \omega_i} \tag{21}$$

where

ω_i = frequency
h = water depth
k_i = wave number
γ = $3/(2\ \rho_s/\rho + 1)$
σ = constant
a_i = wave amplitude
W_s = sediment-settling velocity
z = vertical coordinate.

For the case of shallow water, the suspended sediment concentration, C, at the elevation, z, is given by Liang and Wang (1973):

$$\frac{C}{\overline{C}_o} = \left(\frac{2D}{z}\right)^{|R_i|} \tag{22}$$

$$R_i = \frac{W_s h}{\gamma\sigma\ a_i\ \omega_i} \tag{23}$$

For this study, Equations (22) and (23) for a shallow-water case were used. The rate of suspended sediment transport in the interior zone, Q_S, is then obtained as

$$Q_S = \int_{2D}^{h} C\ (U_S + U_{IS})\ dz \tag{24}$$

where

U_{IS} = velocity component of incidental flow (those other than ones induced by wave action) in the interior zone

U_S = mass-transport velocity (second-order velocity component) of a wave in the interior zone.

The mass-transport velocity, U_S, is calculated using Liang and Wang's expression (Liang and Wang 1973). The vertical-velocity distribution of the incidental flow, U_{IS}, is assumed to follow the 1/7-th-power law. Hence, suspended sediment is also transported by both wave-induced velocity and the incidental flow.

Hence, the sediment transport capacity of flow for noncohesive sediment, Q_T, is:

$$Q_T = Q_B + Q_S \tag{25}$$

Q_T, thus obtained, can then be used to calculate the erosion and/or deposition rates of sand by Equations (12) and (13).

Surf Zone. The formulations discussed above are only applicable to regions well beyond the surf zone. The following expressions are used in the FETRA code to include the littoral (longshore) transport of sediments in the surf zone induced by the energy and momentum expended by breaking waves. The work of Komar (1977) and some of his associates was adopted for this study. The volumetric littoral transport rate S_ℓ and the immersed-weight littoral transport rate I_ℓ are given

$$S_\ell = \frac{I_\ell}{(\rho_s - \rho)\, g a'} \tag{26}$$

$$I_\ell = 0.28\, (ECn)_b \frac{\overline{v}_\ell}{u_m} \tag{27}$$

$$u_m = \left[\frac{2E_b}{\rho h_b}\right]^{1/2} \tag{28}$$

where

$(ECn)_b$ = the energy flux of the waves evaluated at the breaker zone
E_b = the energy of the breaking waves
h_b = the water depth at breaking
$\overline{v}_\ell$ = velocity caused by the combination of waves and currents, ($\overline{v}_\ell = 2.7\, U_m \sin \alpha_b \cos \alpha_b + U_i$)
α_b = breaker angle with the shoreline

U_I = velocity of incidental flow (those other than one induced by waves) in a surf zone
a' = an empirical constant ($\simeq 0.6$).

In the case where the mass transport is induced by wave action alone (in the absence of other currents, i.e., $U_I = 0$), the longshore velocity becomes

$$\overline{v}_\ell = 2.7 U_m \sin\alpha_b \cos\alpha_b \tag{29}$$

Hence, the transport rates for this particular case are given by:

$$S_\ell = (6.85 \times 10^{-5}) (EC_n)_b \sin\alpha_b \cos\alpha_b \tag{30}$$

$$I_\ell = 0.77 (EC_n)_b \sin\alpha_b \cos\alpha_b \tag{31}$$

The total sediment transport capacity, Q_T, is then calculated by

$$Q_t = a \cdot S_\ell \tag{32}$$

where a = unit conversion constant.

Rates of erosion and deposition of noncohesive sediment in a surf zone are then calculated using Equations (12) and (13).

To use the above formulas for the offshore and littoral transport of sediment, temporal and spacial variations of wave characteriscs, including the wave angle at breaking, α_b, must be calculated. This was accomplished by 1) including wind-induced wave mechanisms in FETRA and 2) a wave refraction program, which is used in conjunction with FETRA.

To calculate wave characteristics induced by wind, FETRA uses the following empirical formulations (U.S. Army Corps of Engineers 1962): waves generated by wind over fetches of known lengths can be computed by a method reported in Sverdrup and Munk (1947), Bretschneider (1953), and the Coastal Engineering Research Center's, Shore Protection Manual (U.S. Army Corps of Engineers 1973).

$$H_s = \frac{0.283\ U_w^2}{g} \tanh\left[0.530\left(\frac{gd_m}{U_w^2}\right)^{0.75}\right] \tanh\left\{\frac{0.0125\left(\frac{g\ F_{eff}}{U_w^2}\right)^{0.42}}{\tanh\left[0.530\left(\frac{gd_m}{U_w^2}\right)^{0.75}\right]}\right\} \tag{33}$$

$$T_s = \frac{1.2\ (2\ \pi U_w)}{g} \tanh \left[0.833 \left(\frac{g d_m}{U_w^2} \right)^{0.375} \right] \tanh \left\{ \frac{0.077 \left(\frac{g\ F_{eff}}{U_w^2} \right)^{0.25}}{\tanh \left[0.833 \left(\frac{g d_m}{U_w^2} \right)^{0.375} \right]} \right\} \quad (34)$$

where

H_s = significant wave height (feet)
U_w = wind velocity (feet per second)
g = acceleration due to gravity (32.2 ft/sec^2)
d_m = mean fetch depth (feet)
F_{eff} = effective fetch length (feet)
T_s = significant wave period (seconds)

The significant wave height, H_s, is defined as the average of the one-third highest waves and can be related to the maximum wave height (H_{max}), highest one percent (H_1) wave, and highest ten percent (H_{10}) wave, by the following relationships (U.S. Army Corps of Engineers 1973).

$$H_{max} = 1.77\ H_s$$
$$H_1 = 1.67\ H_s$$
$$H_{10} = 1.27\ H_s$$

The wave amplitude, a, was calculated by

$$H_{RMS} = H_s/1.416 \quad (35)$$

$$a = H_{RMS}/2 \quad (36)$$

The wave number was calculated by Equation (38) through an iteration process.

$$\omega = \frac{2\pi}{T_s} \quad (37)$$

$$k = \frac{\omega^2}{[g \cdot \tanh (k\ d_m)]} = \frac{2\pi}{L} \quad (38)$$

where

ω = wave frequency
k = wave number
L = wave length

The other method to obtain the necessary wave characteristics is to use the wave refraction program, L03D, in conjunction with FETRA. This program was developed by Dobson (1967), and later modified by Ecker and Degraca (1974). The theoretical basis of the wave-refraction program is derived from geometrical optics, and uses the Snell's Law. The program uses wave hindcast data to obtain the representative deepwater waves for all wave directions and periods. From these deepwater waves, the program simulates the process by which each appropriate deepwater wave ray is generated toward shore. Starting from a known point on a contour grid with a given period and an initial direction, the computer program constructs a single wave ray step by step across the grid. At wave breaking, the program calculates the refraction coefficient, K_R; shoaling coefficient, K_S; the wave angle at breaking, α_b; the depth at breaking, d_b; and the wave height, h_b. The program also computes the longshore component of wave power at designated stations along the shoreline. The wave characteristics thus obtained by the wave refraction program are then used by FETRA.

3.1.2 Coastal Waters Without Surface Waves

This is the case if FETRA is to be applied to surface water bodies where sediment erosion and deposition are dominated by currents, as in rivers, estuaries, and possibly certain coastal waters. Because FETRA is a vertically averaged model, it may be applicable to well-mixed estuaries but not well-suited to stratified estuaries.

Similar to the computation of the erosion and deposition rates of noncohesive sediments in coastal waters with surface waves, the following concept was used. Both erosion and deposition of noncohesive sediments are affected by the amount of sediment the flow can carry (e.g., if the amount of sand being transported is less than the flow can carry for given hydrodynamic conditions, the flow will scour sediment from the stream bed to increase the sediment transport rate). This process occurs until the actual sediment transport rate becomes equal to the carrying capacity of the flow or until all the available bed sediments are scoured, whichever happens first. Conversely, the flow deposits sand if its actual sediment transport rate is above its capacity to carry sediment. Because of the simplicity of the formulation, DuBoy's formula (Vanoni 1975) was used to estimate the total sediment transport capacity of flow per unit width, Q_T:

$$Q_T = \psi_D \tau_b (\tau_b - \tau_c) \tag{39}$$

in which τ_b = bed shear stress; τ_c = critical shear stress, defined and determined by DuBoy (Vanoni 1975) as a function of sediment size; and τ_D = coefficent defined and determined by DuBoy (Vanoni 1975) as a function of sediment size. Although the DuBoy's formula is sometimes classified as a bed-load formula, it has been widely used to calculate the total sediment load because of its simplicity (Vanoni 1975). Comparisons of computed and measured sediment loads for the Niobrara River near Cody, Nebraska, and the Colorado River at Taylor's Ferry, Colorado, reveal that DuBoy's formula tends to overestimate a total sediment load under low flows, but provides better estimates under high flows (Vanoni 1975).

The total sediment capacity, Q_T, per unit width at a down-current point was then compared with the actual amount of sand, Q_{TA}, being transported per unit width at an up-current point. Thus, using Equations (12) and (13) from p. 3.5,

$$S_{Rj} = \frac{Q_T - Q_{TA}}{\Delta L}$$

$$S_{Dj} = \frac{Q_{TA} - Q_T}{\Delta L}$$

in which ΔL = distance between the up-current and down-current locations; and Q_{TA} = is obtained as a product of sand concentration and a flow rate per unit width, as defined previously.

As discussed before, for cohesive sediments (e.g., clay and silt), the following formulas [Equations (14) and (15) from p. 3.6] developed by Partheniades (1962) and Krone (1962) were also used for this case:

$$S_{Rj} = M_j \left(\frac{\tau_b}{\tau_{cRj}} - 1 \right)$$

$$S_{Dj} = W_{sj} C_j \left(1 - \frac{\tau_b}{\tau_{cDj}} \right)$$

where

M_j = erodibility coefficient for jth sediment
τ_{cDj} = critical shear stress for sediment deposition for jth sediment, and
τ_{cRj} = critical shear stress for sediment erosion for jth sediment.

Values of M_j, τ_{cDj}, and τ_{cRj} must be determined by field or laboratory tests, or both (Krone 1962; Partheniades 1962; Vanoni 1975). Similar to erosion of sand, cohesive sediment will be eroded with the rate of S_{Rj} or until all the available cohesive sediment in the bed is scoured, whichever results in a smaller amount of eroded sediment.

3.1.3 Bed Computations

To simulate sea bed or riverbed conditions as regards the bed's elevation change, sediment distribution, and armoring, FETRA divides the sea bed or riverbed--except for the top layer--into a number of layers with a standard thickness. The thickness of the top layer is equal to or less than the standard thickness at any given time. Each layer consists of a combination of clean or contaminated sediments of three sizes (or types), or both, selected

for sediment transport as mentioned previously. Based on the sediment erosion or depositon rate [S_{Rj} or S_{Dj}, as calculated by Equations (12) through (15)], sediments of each size fraction (or type) will be scoured from or deposited to the bed, changing the thickness of the top layer and possibly the number of bed layers. When the top bed layer thickness reaches more than the standard thickness due to sediment deposition, a new top layer will be formed. On the other hand, when all the sediment in the top bed layer is scoured, the bed layer immediately below the original top layer becomes the new top layer. This process will continue until the actual sediment transport rate becomes equal to the carrying capacity of the flow or until the available bed sediment is completely scoured, whichever occurs first.

For the sediments of the second and third size fractions (or types), the number of bed layers eroded cannot exceed the number of layers eroded for the sediment of the first size fraction (or type). In other words, sediments of the first sediment size fraction (or type) cover and protect the sediments of the second and the third size fractions (or types) in lower layers from erosion, thus exhibiting armoring of the bed.

Contaminant distributions associated with each sediment size fraction (or type) within the sea bed or riverbed were also obtained. We kept track of the amount of contaminants removed from or added to each bed layer during a simulation period due to erosion or deposition of contaminated sediment, or both, and direct adsorption/desorption between bed sediment and dissolved contaminants in overlaying water.

3.2 DISSOLVED CONTAMINANT TRANSPORT SUBMODEL

Dissolved contaminants interact both with sediments in motion (suspended and bed-load sediments) and with stationary sediments in the sea bed or riverbed. To account for these interactions, this submodel includes the mechanisms of

- advection and diffusion/dispersion of dissolved contaminants
- adsorption (uptake) of dissolved contaminants by both moving and stationary sediments or desorption from the sediments into water
- radionuclide decay, or chemical and biological degradation of contaminants, and
- contaminant contribution from point/nonpoint sources, and subsequent mixing.

Contributions from wastewater discharges, overland runoff flow, fallout, and ground water to a coastal water or a river system may be treated as a part of the point/nonpoint source contributions. Effects of water quality (e.g., pH, water temperature, and salinity), and sediment characteristics (e.g., clay minerals), can be included by changing the distribution (or partition) coefficients of contaminants.

The governing equation of dissolved contaminant transport for the three-dimensional case is

$$\frac{\partial G_w}{\partial t} + \frac{\partial}{\partial x}(UG_w) + \frac{\partial}{\partial y}(VG_w) + \frac{\partial}{\partial z}(WG_w) = \frac{\partial}{\partial x}\left(\varepsilon_x \frac{\partial G_w}{\partial x}\right)$$

$$+ \frac{\partial}{\partial y}\left(\varepsilon_y \frac{\partial G_w}{\partial y}\right) + \frac{\partial}{\partial z}\left(\varepsilon_z \frac{\partial G_w}{\partial z}\right) - \lambda G_w - \sum_i K_j(C_j K_{dj} G_w - G_j) + Q_w \qquad (40)$$

In addition to the previously defined symbols:

K_{dj} = distribution (or partition) coefficient between dissolved contaminant and particulate contaminant associated with jth sediment

K_j = transfer rate of contaminant adsorption or desorption to reach an equilibrium condition with jth sediment in motion

G_j = particulate contaminant concentration associated with jth sediment in motion (weight of contaminant or radioactivity of contaminant or radioactivity per unit volume of water)

G_w = dissolved contaminant concentration (weight of contaminant or radioactivities per unit volume of water)

Q_w = source strength of dissolved contaminant, and

λ = radionuclide decay rate, or chemical and biological degradation rates of contaminant.

The distribution coefficient, K_{dj}, for the jth sediment, is defined by

$$K_{dj} = \frac{\dfrac{f_{sj}}{M'_j}}{\dfrac{f_w}{V_w}} = \frac{f_{sj}}{f_w C_j} \qquad (41)$$

where

f_{sj} = fraction of contaminant sorbed by jth sediment
f_w = fraction of contaminant left in solution
M'_j = weight of jth sediment
V_w = volume of water, and
$f_{sj}/f_w = G_j/G_w$.

Equation (41) may be rewritten as

$$G_j = K_{dj} C_j G_w \tag{42}$$

Adsorption of contaminants by sediments or desorption from sediments are assumed to occur toward an equilibrium condition with the contaminant transfer rate, K_j (unit of reciprocal of time), if the particulate and dissolved contaminant concentrations differ from their equilibrium values as expressed in Equation (42). The boundary conditions for dissolved contaminant transport are

$$WG_w - \varepsilon_z \frac{\partial G_w}{\partial z} = 0 \qquad \text{at } z = h \tag{43}$$

$$\varepsilon_z \frac{\partial G_w}{\partial z} = \sum_j \gamma_j (1 - P) D_B K_{Bj} (K_{dj} G_w - G_{Bj}) \qquad \text{at } z = 0 \tag{44}$$

$$VG_w - \varepsilon_y \frac{\partial G_w}{\partial y} = q_w \quad \text{or } G_w = G_{wo} \qquad \text{at } y = 0 \text{ and } B \tag{45}$$

where

D_B = averaged bed sediment diameter

G_{Bj} = particulate contaminant concentration associated with the jth sediment in the sea bed or riverbed (weight of contaminant or radioactivity per unit weight of bed sediment)

K_{Bj} = transfer rate of contaminant adsorption or desorption to reach an equilibrium condition with jth bed sediment

G_{wo} = constant concentration of dissolved contaminant

P = porosity of the sea bed or riverbed

γ_j = density of jth bed sediment, and

q_w = lateral influx of dissolved contaminant.

Equation (44) expresses the direct adsorption or desorption between a dissolved contaminant and stationary jth sediment in the bed, or both. The distribution coefficients for both moving and stationary sediments were assumed to be the same as long as these sediments have the same characteristics, e.g., diameters, clay minerals, organic content. The difference in the adsorption/desorption mechanism between these two sediments is the time required to reach equilibrium. We also assumed that direct adsorption or desorption, or both, from bed sediments occurs only with sediments on the bed surface.

In order to vertically integrate Equation (40) let

$$G_w = \overline{G}_w + G_w'' \tag{46}$$

$$G_j = \overline{G}_j + G_j'' \tag{47}$$

where

$\overline{G}_j$ = depth averaged value of particulate contaminant concentration associated with jth sediment

G_j'' = fluctuation from the depth averaged value of particulate contaminant concentration

$\overline{G}_w$ = depth averaged value of dissolved contaminant concentration, and

G_w'' = fluctuation from the depth averaged value of dissolved contaminant concentration.

Integrating Equation (40) over the entire flow depth yields the following final transport equation of dissolved contaminants:

$$h\frac{\partial \overline{G}_w}{\partial t} + h\overline{U}\frac{\partial G_w}{\partial x} + h\overline{V}\frac{\partial \overline{G}_w}{\partial y} = \frac{\partial}{\partial x} K_x h\frac{\partial \overline{G}_w}{\partial x} + \frac{\partial}{\partial y} K_y h\frac{\partial \overline{G}_w}{\partial y}$$

$$- \left[\lambda h + Q_\ell h + \sum_i K_j K_{dj} \overline{C}_j + \sum_j K_{Bj}\lambda_j (1 - P) D_B K_{dj}\right] \overline{G}_w$$

$$+ \left(\sum_j K_j \overline{G}_j h + \sum_j K_{Bj}\gamma_j (1 - P) D_B G_{Bj} + Q_w h\right) \tag{48}$$

The boundary conditions for this equation are the same as those in Equation (45).

3.3 PARTICULATE CONTAMINANT TRANSPORT SUBMODEL

The transport of sediment-attached contaminants is solved separately according to sediment size fraction (or types). This submodel also includes the mechanisms of

- advection and diffusion/dispersion of particulate contaminants
- adsorption (uptake) of dissolved contaminants by sediment or desorption from sediment into water
- radionuclide decay, or chemical and biological degradation of contaminants

- deposition of particulate contaminants on the sea bed or riverbed or erosion from the ocean bed or riverbed

- contaminant contribution from point/onpoint sources and subsequent mixing.

Again, contributions to a water body from wastewater discharges, overland runoff flow, fallout, and ground water may be treated as a part of the point/nonpoint sources contributions. The three-dimensional distribution of the particulate contaminant within the bed is also computed, as mentioned earlier.

As in the transport of sediment and dissolved contaminants, the three-dimensional transport equation for contaminants adsorbed by the jth sediment may be expressed as

$$\frac{\partial G_j}{\partial t} + \frac{\partial}{\partial x}(UG_j) + \frac{\partial}{\partial y}(VG_j) + \frac{\partial}{\partial z}[(W - W_{sj})\,G_j]$$

$$= \frac{\partial}{\partial x}\left(\varepsilon_x \frac{\partial G_j}{\partial x}\right) + \frac{\partial}{\partial y}\left(\varepsilon_y \frac{\partial G_j}{\partial y}\right) + \frac{\partial}{\partial z}\left(\varepsilon_z \frac{\partial G_j}{\partial z}\right)$$

$$= \lambda G_j - K_j\left(G_j - C_j K_{dj} G_w\right) + Q_j \qquad (49)$$

in which Q_j = source strength of particulate contaminant associated with jth sediment. The boundary conditions for this case are

$$(W - W_{sj})\,G_j - \varepsilon_z \frac{\partial G_j}{\partial z} = 0 \qquad \text{at } z = h \qquad (50)$$

$$(1 - \gamma)\,W_{sj} G_j + \varepsilon_z \frac{\partial G_j}{\partial z} = G_j S_{Dj} - G_{Bj} S_{Rj} \qquad \text{at } z = 0 \qquad (51)$$

$$VG_j - \varepsilon_y \frac{\partial G_j}{\partial y} = q_j \;, \quad \text{or} \quad G_j = G_{jo} \qquad \text{at } y = 0 \text{ and } B \qquad (52)$$

in which q_j = lateral influx of particulate contaminant associated with jth sediment; and G_{jo} = constant particulate contaminant concentration associated with jth sediment.

Integrating Equation (49) over the entire depth yields the following final expression of the particulate contaminant transport equation:

$$h\frac{\partial \bar{G}_j}{\partial t} + h\bar{U}\frac{\partial \bar{G}_j}{\partial x} + h\bar{V}\frac{\partial \bar{G}_j}{\partial y} = \frac{\partial}{\partial x}\left(K_x\, h\frac{\partial \bar{G}_j}{\partial x}\right)$$

$$+ \frac{\partial}{\partial y}\left(K_y\, h\frac{\partial \bar{G}_j}{\partial y}\right) - \left(S_{Dj} + \lambda h + Q_\ell h + K_j h\right)\bar{G}_j$$

$$+ \left(K_j K_{dj} \bar{C}_j \bar{G}_w h + G_{Bj} S_{Rj} + Q_j h\right) \qquad (53)$$

The boundary conditions for this case are the same as those expressed in Equation (52).

3.3.1 Finite Element Method

Because of its increased solution accuracy and ready accommodation to complex boundary geometry, the finite element solution technique with the Galerkin weighted residual method (Desai and Abel 1972) was used in this study to solve Equations (11), (48), and (53) with the boundary conditions of Equations (4), (44), and (51). The version of the FETRA used for the Irish Sea simulation uses the upwind scheme to treat the advection terms in the governing equations. The flow domain was divided into a series of triangular elements interconnected at nodal points. Six nodes were associated with each triangle, three at the vertices and three on the midsides. A quadratic approximation was made for the sediment and contaminant concentrations with each element. Linear interpolation was used for variations of flow depth and velocity within an element. The computer program was written in FORTRAN IV language.

4.0 MODEL APPLICATION TO THE IRISH SEA

The Irish Sea was selected as a FETRA application test site because extensive data sampling had been conducted there by the Fisheries Radiobiological Laboratory of the United Kingdom's Ministry of Agriculture. Note that this study was conducted to test the FETRA model with available field data and is not intended to assess the potential impact of the Windscale Nuclear Fuel Reprocessing Plant on the Irish Sea.

To validate the FETRA model, we needed extensive data to calibrate the model during one simultion period and then to validate it for simulations without changing model coefficients and/or parameters. Unfortunately, we could not obtain many of the field data (especially raw field data) necessary to validate the model. Data were lacking for concentration distributions of suspended sediments and their size fractions, and of radionuclides sorbed by suspended and bed sediments especially for different sediment size fractions. Thus, this study focused on evaluating the behavior of FETRA under fairly realistic Irish Sea conditions rather than validating the model.

Two models were used to simulate ^{137}Cs migration and fate in the Irish Sea over two months of 1974. These are the hydrodynamic model, CAFE, (Wang and Connor 1975) and FETRA. Both models are depth-averaged, two-dimensional models using the finite element method with the Galerkin-weighted residual technique. CAFE simulated time-varying velocities and depths to supply the necessary hydrodynamic data to the transport model, FETRA. The sediment/contaminant transport model, FETRA, was then used to predict wind-generated waves, sediment transport, and the distribution of dissolved ^{137}Cs and sediment-sorbed ^{137}Cs in the water column and sea bed. For this model application, both CAFE and FETRA used exactly the same finite element grid discretization of the Irish Sea study area. Note that the CAFE formulations use linear interpolations of velocity and depth. FETRA used linear interpolations for velocity and depth to be compatible with CAFE output, but used quadratic interpolations for sediment and contaminant concentrations.

4.1 DESCRIPTION OF THE STUDY AREA

The Windscale Nuclear Fuel Reprocessing Plant in England has been discharging a low-level radionuclide liquid effluent into the Irish Sea since 1957 (Hetherington 1976). The annual rate of ^{137}Cs discharged from the Windscale plant to the Irish Sea is shown in Figure 4.1 (Smith et al. 1980). Because of the large increase in the ^{137}Cs discharge rate from 20,762 curies in 1973 to 109,765 curies in 1974, the ^{137}Cs migration that occurred in 1974 was selected as a test case for the FETRA model application.

Figure 4.2 shows the location of the Irish Sea. The box indicates the study area: the northern part of the Irish Sea. Windscale is located on the northwest coast of England. Figure 4.3 shows the study area in more detail. The dotted lines represent the open boundaries of our simulation region. The northern boundary extends between Donaghadee, Northern Ireland and Port Patrick, Scotland, while the southern boundary is bordered by Dun Laoghaire,

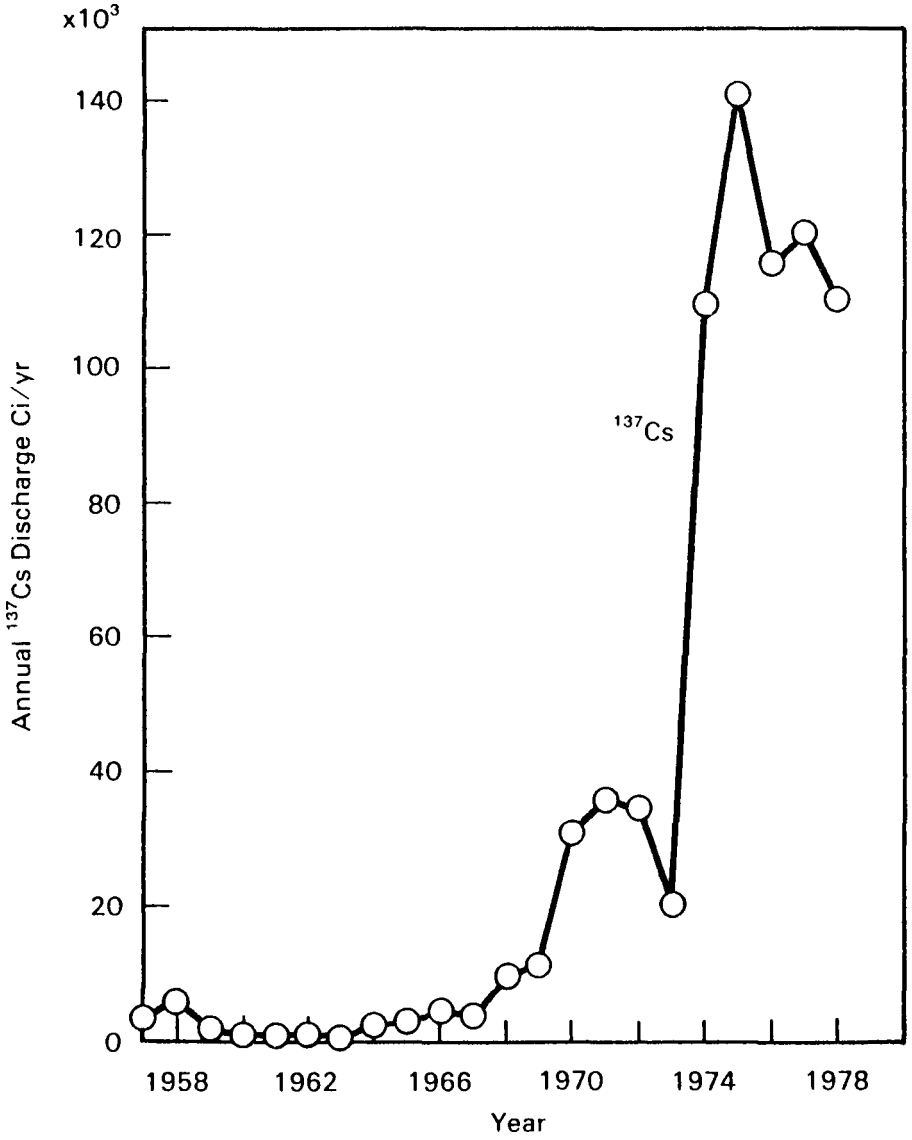

FIGURE 4.1. Annual ^{137}Cs Discharge Rate Released to the Irish Sea

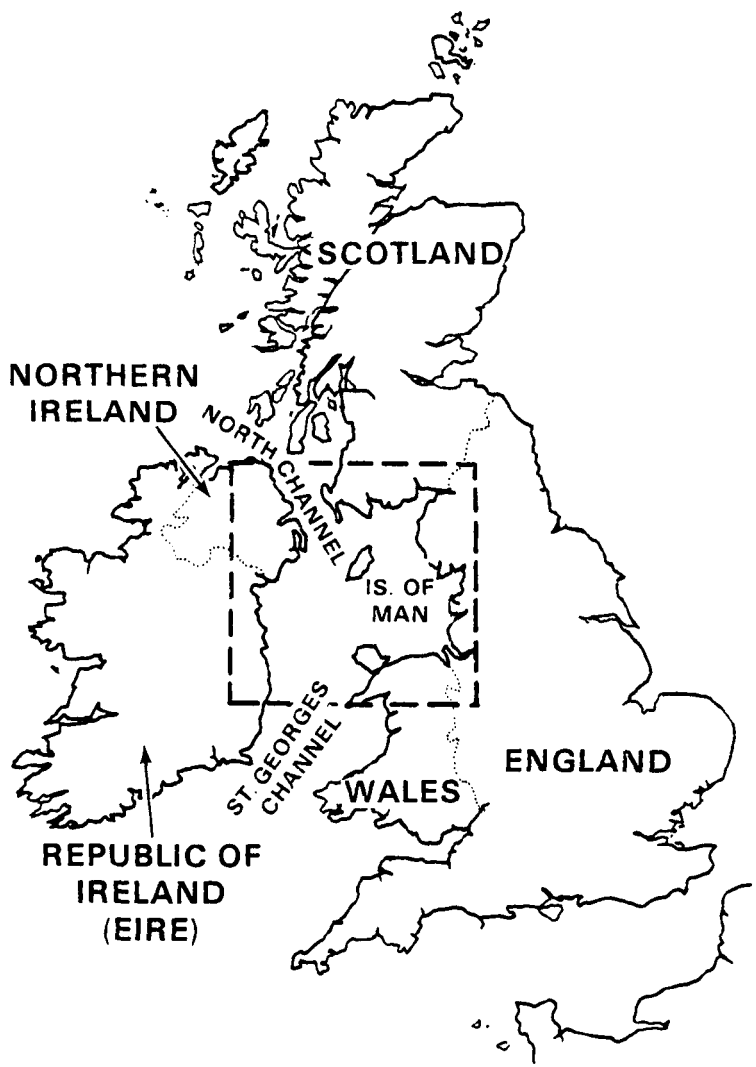

FIGURE 4.2. Location of the Irish Sea (box indicates the study area)

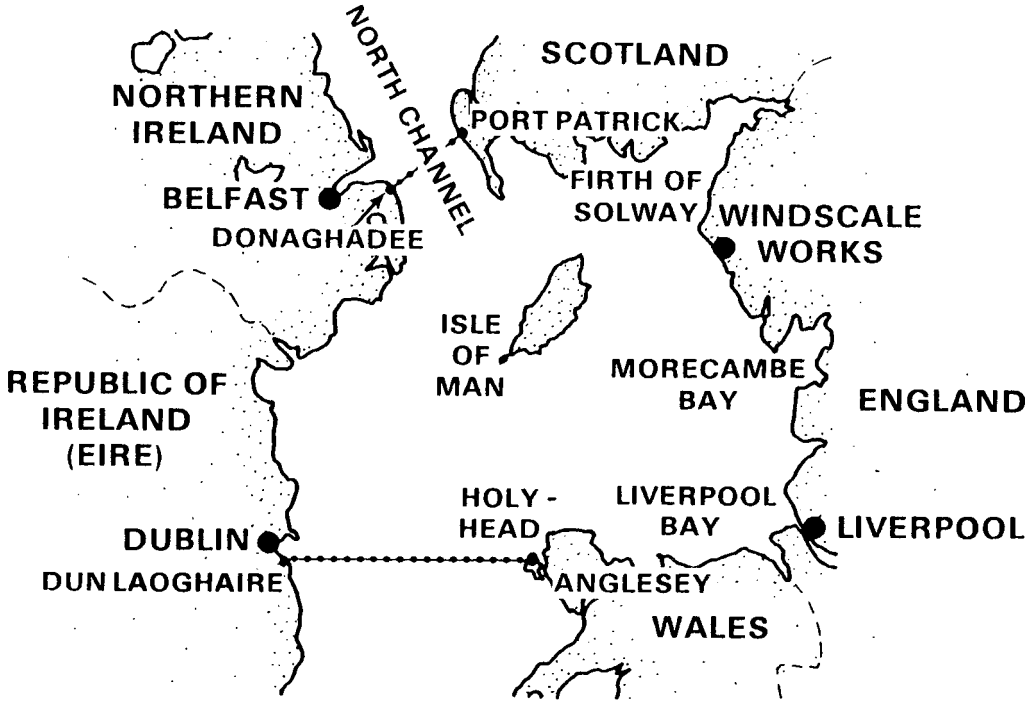

FIGURE 4.3. The Irish Sea Study Area

Eire and Holyhead, Wales. The dimensions are approximately 182 km (98 nautical miles) from north to south and 223.5 km (121 nautical miles) from west to east. The western part of the study area has depths of 70 to 100 m (230 to 328 ft) while the eastern part has an average depth of about 40 m (131 ft).

4.2 HYDRODYNAMIC SIMULATION

The FETRA model includes the equations for sediment and contaminant transport. These equations contain the variables of flow velocity and flow depth, which are not calculated in FETRA. Therefore, a hydrodynamic model is required to provide, as input to FETRA, the flow velocities and flow depths required at each node of the finite element grid for each time step in the simulation. In this application, we have used the hydrodynamic model, CAFE (Circulation Analysis with Finite Elements).

CAFE is a two-dimensional (vertically-averaged), finite-element model that uses the Galerkin residual technique (Wang and Connor 1975). The model simulates tide- and wind-driven circulation. The output includes the flow velocity and flow depth at each node of the grid for each time step.

In previous applications of CAFE and FETRA to coastal sites, we have also used the wave-refraction model, LO3D (Ecker and Degraca 1974). We did not use the LO3D model for this application because the water is very deep in most of the Irish Sea, and, thus, wave refraction is not important. Instead, we used equations in FETRA to calculate wave characteristics of wind-induced waves.

This section on hydrodynamic modeling is divided into two sections. The input data used in this application of CAFE are presented in the first section. The second section describes the simulation results for both the calibration period and the period selected for the FETRA application. The hydrodynamics of the study area will be presented in the discussion on simulation results.

4.2.1 Input Data Used in CAFE Application

The following input data are required to run the CAFE model:

- Discretization of the flow region
- Bathymetry
- Boundary conditions (for flow)
- Initial conditions (for flow)
- Bottom roughness
- Wind velocity
- Eddy viscosities

The data used for each of these model elements are discussed in this section. The discretization (i.e., the finite-element grid), the bathymetry (i.e., water depths), the bottom roughness, and the eddy viscosities do not depend on the selected simulation period. In contrast, the initial conditions, the time-varying boundary conditions, and the time-varying wind velocity must be appropriate for the selected simulation period. Therefore, we first discuss the simulation periods that were used in our application.

4.2.1.1 Simulation Periods

Two time periods were simulated in this study: 1) April 1968 and 2) July and August 1974. The former period was selected for calibrating CAFE, since this period contained the most complete set of flow velocity field data available to us at the time of our investigation. Model calibration involves adjusting various model parameters (in this case, bottom roughness and eddy viscosities) to achieve reasonable agreement between model output (i.e., predicted flow velocities) for a specific time period and field data collected during that same period. Model calibration gives the user confidence in using the computer model in a predictive mode. This confidence results from the calibration process demonstrating that the model simulates the flow field reasonably well when appropriate values are selected for the parameters. The selected values are then used for all simulations of the flow region.

The second period - July and August 1974 - was considered to be a good choice for the FETRA runs, since a significant increase in ^{137}Cs discharge rates during this period produced much higher dissolved ^{137}Cs concentrations in the Irish Sea as compared to previous years (See Figure 4.1).

4.2.1.2 Discretization of the Flow Region

Figure 4.4 shows the finite-element grid used for our CAFE runs. As discussed in the introduction, this same grid is also used for the FETRA runs but with additional nodes; FETRA uses midside nodes on the triangles as well as

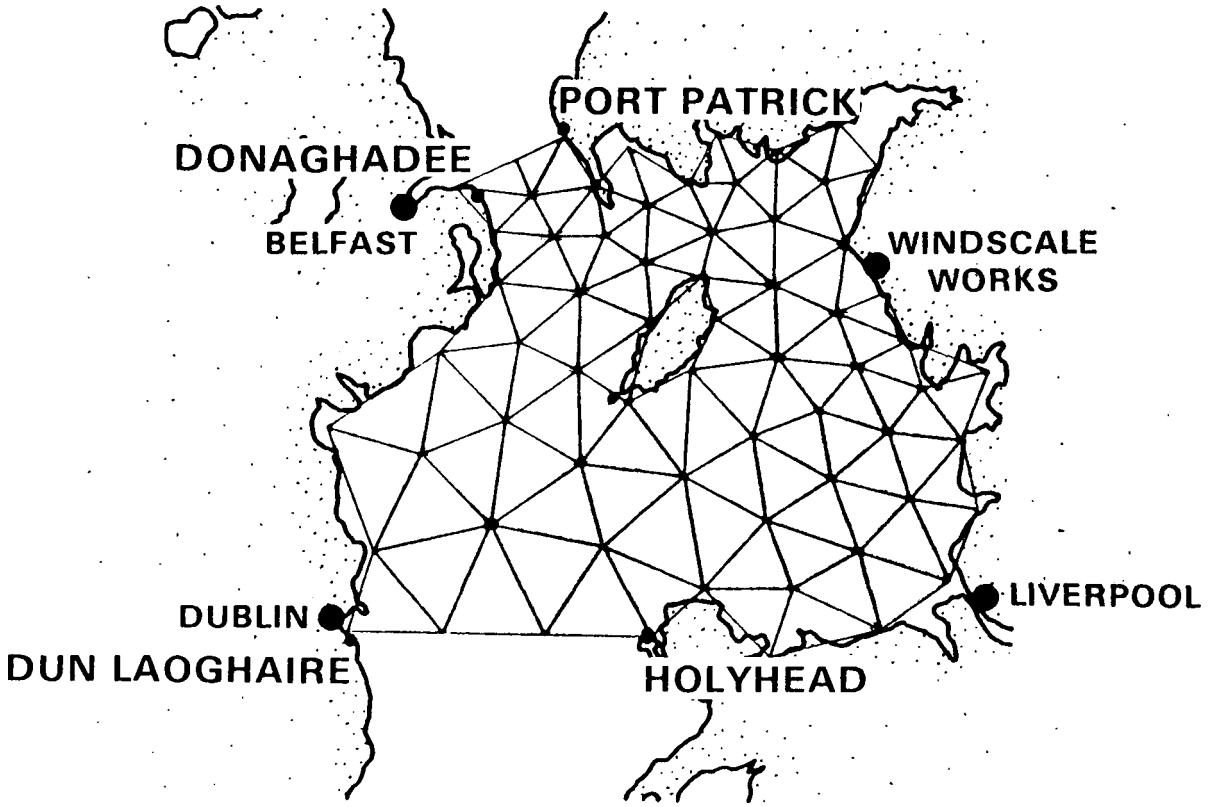

FIGURE 4.4. Discretization of the Study Region

corner nodes because it uses a quadratic approximation for sediment and contaminant concentrations. (However, FETRA uses a linear approximation for velocity and depth to be compatible with the CAFE output.)

Because the same grid would be used for the FETRA runs, we designed a coarse grid - 96 elements and 65 nodes - to minimize the cost of running FETRA. The computer time required to run FETRA is affected by the grid size in two ways: 1) the smallest triangle leg (ΔX) determines the largest time step (ΔT) that can be used (because of stability criteria defined by the Courant and diffusion numbers or numerical accuracy) and 2) the computer time increases significantly with an increase in the number of nodes, because the band widths of resulting solution matrices become greater. To minimize the matrix band widths for both the CAFE and the FETRA applications, we used a computer program to optimize the node numbering and thereby minimize the required computer time.

A six-minute time step was used for all CAFE simulation runs. (A one-hour time step was used for all FETRA simulation runs, as discussed in Section 4.3.)

4.2.1.3 Bathymetry

The CAFE model requires an estimate of the water depth at each node of the grid. The bathymetric data were derived from navigation charts.[a] Figure 4.5 shows depth contours (in fathoms) for the study area. The north entrance is

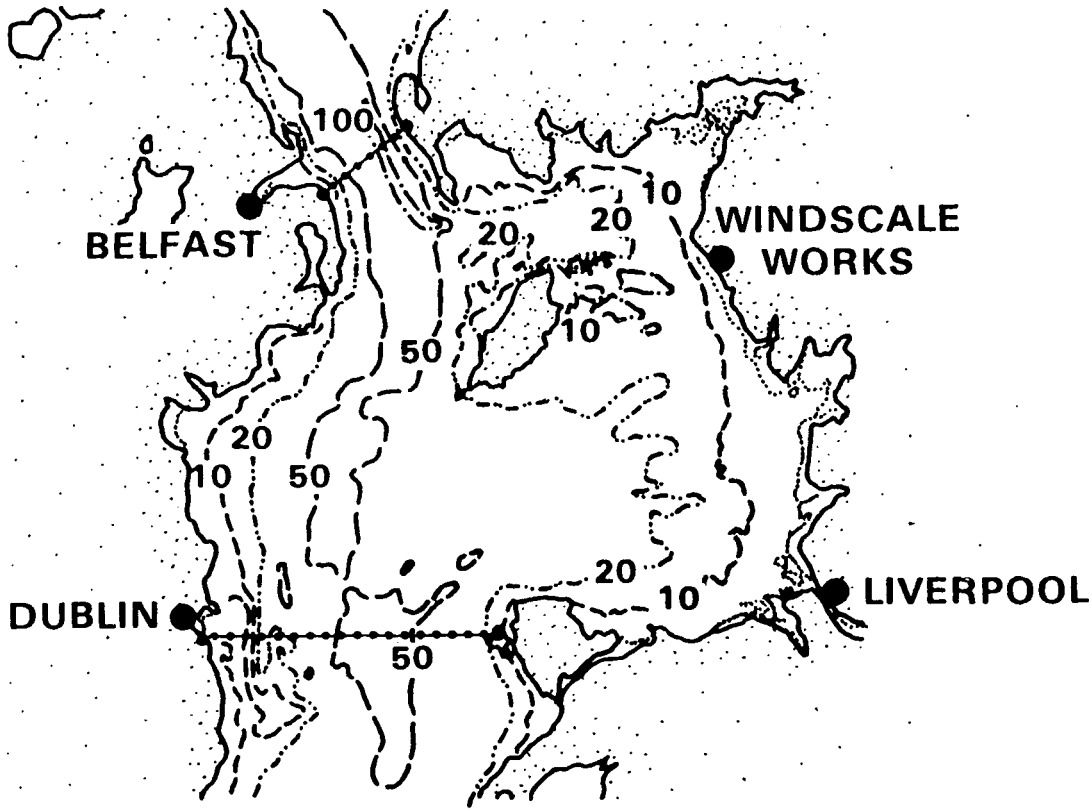

FIGURE 4.5. Bottom Contours (Fm) (after Bowden 1955)

the deepest part of the study area, with depths as great as 100 fm (600 ft or 183 m). The western part of the region averages 50 fm (300 ft or 91 m). The other parts are slightly shallower, with 20-fm (120-ft or 37-m) depths in the region's eastern part and north of the Isle of Man, and 20- to 40-fm (120- to 140-ft or 37- to 43-m) depths south of the Isle of Man.

4.2.1.4 Boundary Conditions

Water surface elevations must be specified at all open boundary nodes for each time step of the simulation. For the stations located on either side of the two open boundaries, water surface elevations were obtained from National Ocean Survey (NOS) tide tables (U.S. Department of Commerce 1967, 1973). Water surface elevations at other open boundary nodes were estimated by linear interpolation.

Figure 4.6 shows the average range of tide (in feet) for the study area.[(a)] The tidal range is the difference in height between consecutive high and low waters. As shown in Figure 4.6, the tidal range at the open boundaries

(a) Admiralty Chart No. 1411, 1824a, 1826, Hydrographic Office, United Kingdom.
(a) The ranges in Figure 4.6 are based on the M_2 tidal constituent, which is the dominant tidal influence in the Irish Sea. This is discussed in more detail in the Results section.

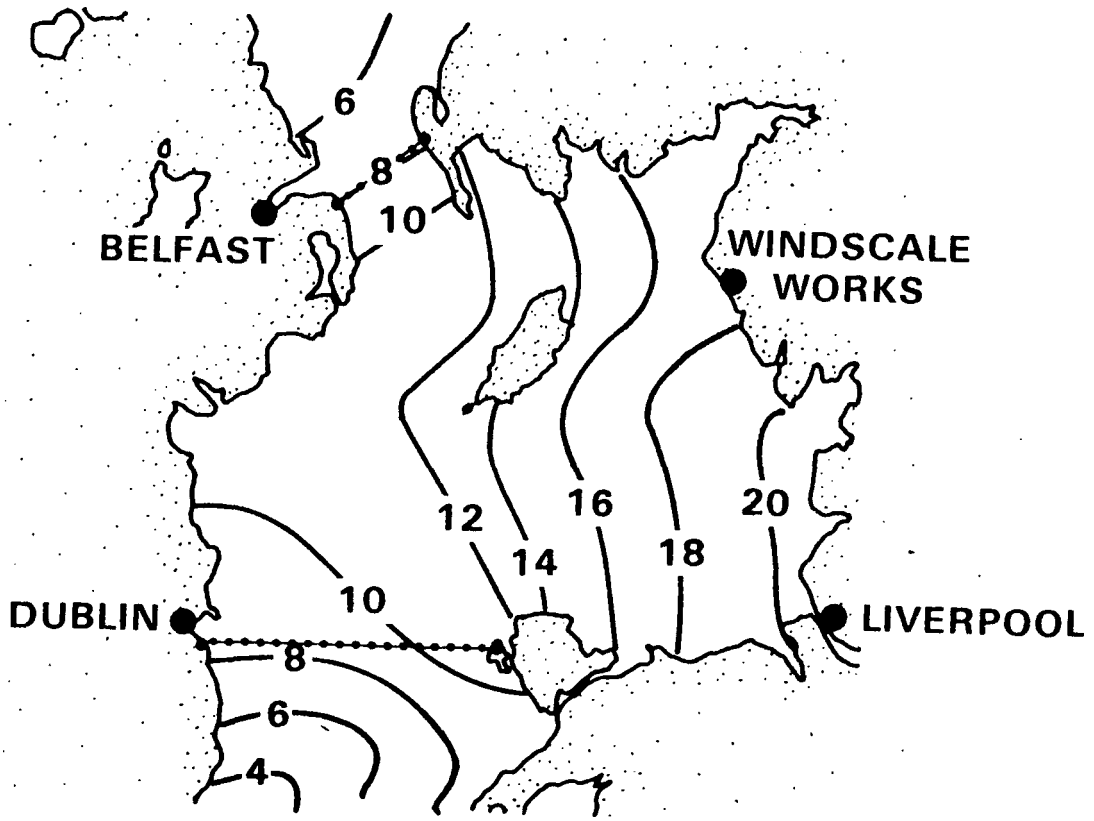

FIGURE 4.6. Average Range of Tide (Corange Lines) in Feet for the Major Lunar Constituent, M_2 (after Bowden 1955)

of our simulation region is 8 to 9 ft (2.4 to 2.7 m). The range increases in the interior of the region, reaching 20 ft (6.1 m) in the vicinity of Morecambe Bay and Liverpool Bay.

4.2.1.5 Initial Conditions

The initial water surface elevation at each node in the grid is required for each simulation run. To overcome the effect of the assigned initial conditions, the model was run for two tidal cycles before output was saved for either the calibration (comparison with field data) or for the FETRA runs.

4.2.1.6 Bottom Roughness

CAFE requires a bottom roughness value for each element. Simulations were made for Manning coefficients of 0.025 and 0.040. The same value was assigned at all locations as there was no rigorous way of assigning spatially varying values. A limited sensitivity analysis indicated that this change in bottom roughness had no appreciable effect on either predicted flow velocities or predicted water surface elevations. A value of 0.040 was used for all simulation runs.

4.2.1.7 Wind Velocity

A wind velocity value is required for each time step in the simulation. The version of the CAFE code used in this application assigns the specified value to all the nodes in the grid (i.e., the wind velocity is spatially uniform) for a given time step. A limited sensitivity analysis showed that the simulated flow velocities were not very sensitive to wind, as would be expected because of the large water depths. A southwesterly wind of magnitude 1.0 m/s was used in the simulations. As a result, the changing water surface elevation due to tides was the sole driving force for the simulated hydrodynamics.

4.2.1.8 Eddy Viscosities

The eddy viscosity coefficients help limit numerically generated short wave noise (Wang and Connor 1975). They affect the predicted currents and have little effect on tidal ranges (Wang and Connor 1975). For our grid a value of 1000 m^2/s resulted in numerical instability, probably because of the coarseness of the grid. Thus, a larger value (we used 5000 m^2/s) was required for a stable simulation. A further increase in the value of the eddy diffusivity coefficients (to 9000 m^2/s) was necessary to obtain reasonable hodographs (or velocity ellipses), again probably because of the coarseness of the grid.

4.2.2 Simulation Results

This section will focus on the calibration results. The model results will be evaluated qualitatively and quantitatively. The qualitative evaluation will be based on the general flow pattern and will introduce basic information contained in the literature on the hydrodynamics of the Irish Sea. The quantitative evaluation will be based on a comparison of simulated and measured velocity ellipses (or hodographs) and an examination of the maximum flood and ebb currents. Hydrodynamic information that is specific to the April 1968 calibration period will be introduced in the quantitative evaluation discussion. Information regarding the 1974 simulation period is presented at the end of this section.

4.2.2.1 Qualitative Evaluation

The literature contains a significant amount of information regarding the hydrodynamics of the Irish Sea. For example, it is known that the astronomical tide is the primary driving force for the circulation of the Irish Sea. The dominant tidal influence is the lunar semidiurnal tidal wave, M_2, having a period of 12 hour 25 minutes of solar time.[a] In the Irish Sea, residuals (e.g., from wind, horizontal density gradients, tidal nonlinearity, or differences in mean water level between the North and South exits) are typically 1 to

---

(c) M_2 is known as a partial tide. The subscript 2 refers to the fact that it is a semi-diurnal tide, so it results in 2 high tides and 2 low tides per day. Partial tides are used to analyze the tide at any given locality. Any tide can be shown to consist of a number of partial tides. Each partial tide has a different period and angular velocity and is related to the motion of the earth relative to the moon and the sun.

2 orders of magnitude less than the maximum tidal streams (Robinson 1979). The information presented below is based on the dominance of the M_2 tidal constituent.

Figure 4.7 shows the average time of maximum flood streams as found in Bowden (1955). Ippen (1966) presents similar information. The numbers represent lunar hours (1 hour 2 minutes of solar time). The figure shows that the maximum flood streams occur at approximately the same time over the entire area (Bowden 1955).

Figure 4.8 shows the average time of high water (Bowden 1955). The time of high water is the same at all points on a given cotidal line. Ippen (1966) presents similar information. Again, the numbers represent lunar hours. The figure shows that high tide occurs within one hour over the entire region.

Figure 4.9 shows current lines of the M_2 tidal constituent. Tidal water enters from both the north and the south (at approximately the same time), dividing upon entering to go on either side of the Isle of Man. The flood tides meet on the east side of the Isle of Man, somewhere across a line from the Isle of Man to Morecambe Bay (Ippen 1966; Mauchline and Templeton 1963). The flow velocities will be relatively low where the flood tides meet.

Figure 4.10 shows the maximum current velocities resulting from the M_2 tidal streams. In the flow region north of the Isle of Man, maximum velocities are 0.8 m/s or slightly larger. Velocities are smallest west of the Isle of Man, ranging from less than 0.1 m/sec to 0.3 m/sec. Velocities east of the Isle of Man are generally less than 0.4 m/sec. In the flow region south of the Isle of Man, velocities range from 0.4 m/sec to greater than 0.9 m/sec.

Figures 4.11 and 4.12 show maximum flow velocities simulated by CAFE for two different times in April 1968. Our simulation results indicate the following:

1. Maximum simulated velocities occur within one hour over the whole region.

2. High water also occurs within one hour over the entire study region.

3. The flow velocities east of the Isle of Man meet in the region between the Isle of Man and Morecambe Bay.

4. The velocity magnitudes compare well with those shown in Figure 4.10 except for the following: a) simulated velocities are significantly lower northeast of the Isle of Man and b) simulated velocities are higher just south of the Isle of Man.

Thus, the above qualitative comparison shows reasonable agreement between simulated flow velocities and patterns and general hydrodynamic information that is available for the Irish Sea.

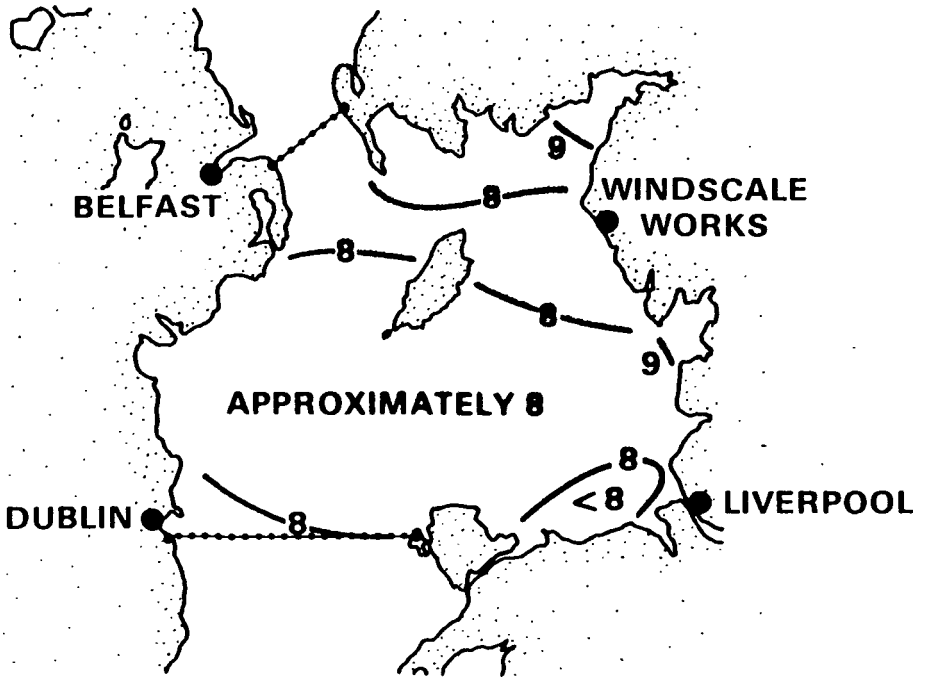

FIGURE 4.7. Average Time of Maximum Flood Streams for the Major Lunar Constituent, M_2 (the numbers represent lunar hours after moon's transit at the meridian of Greenwich) (after Bowden 1955)

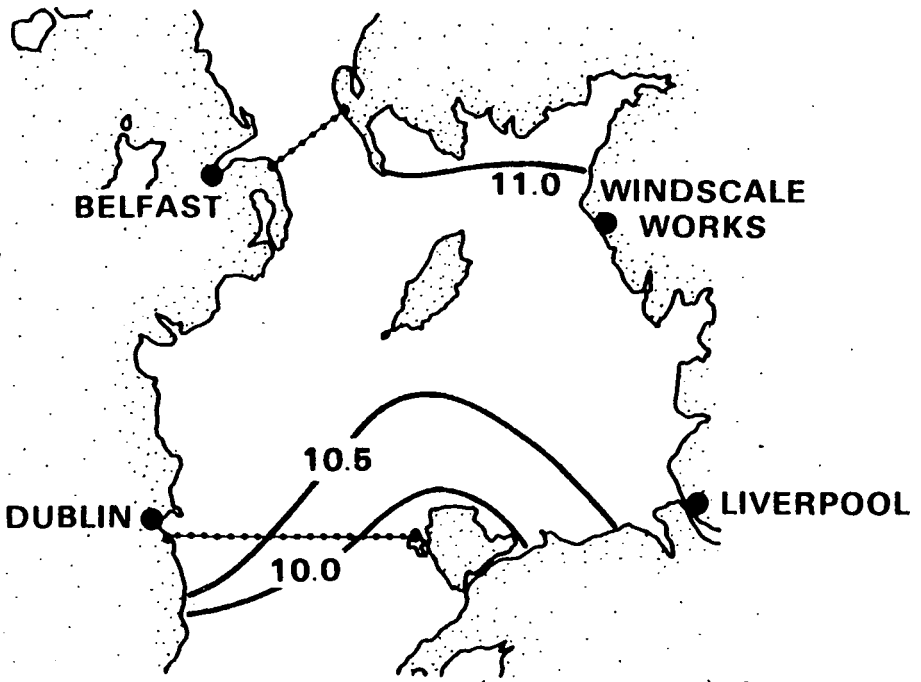

FIGURE 4.8. Average Time of High Water (Cotidal Lines) for the Major Lunar Constituent, M_2 (the numbers represent lunar hours after moon's transit at the meridian of Greenwich) (after Bowden 1955)

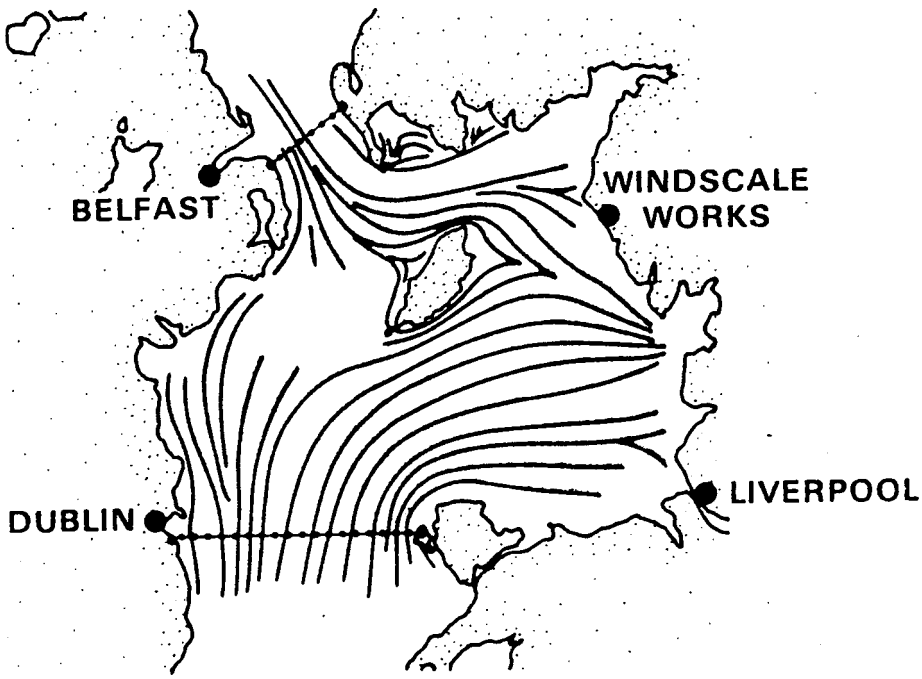

FIGURE 4.9. Current Lines at Mean Tide Level for the M_2 Tidal Constituent (after Ippen 1966)

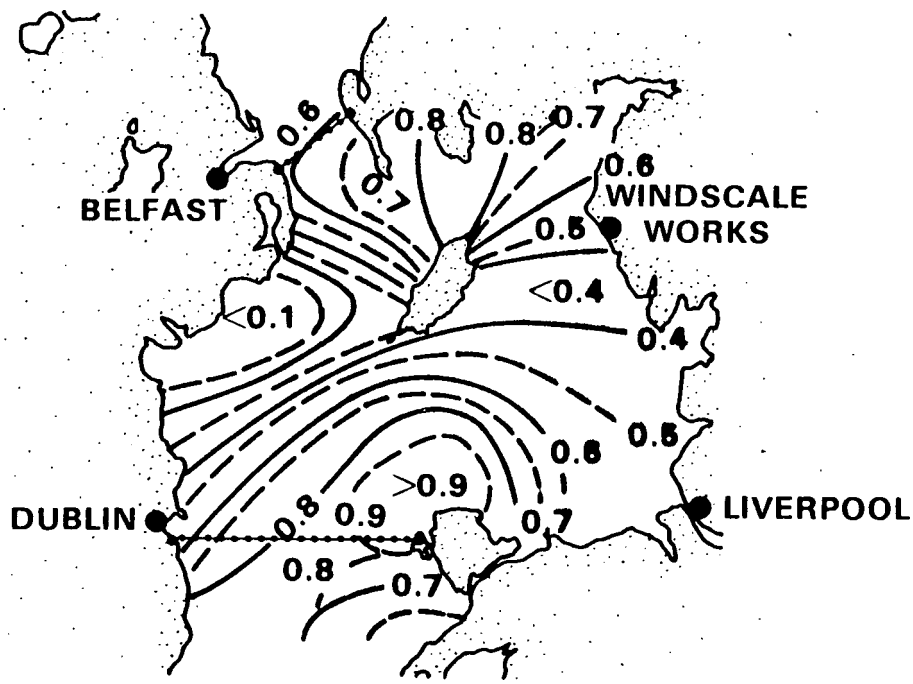

FIGURE 4.10. Maximum Current Velocities in m/s Resulting from the M_2 Tidal Streams (after Robinson 1979)

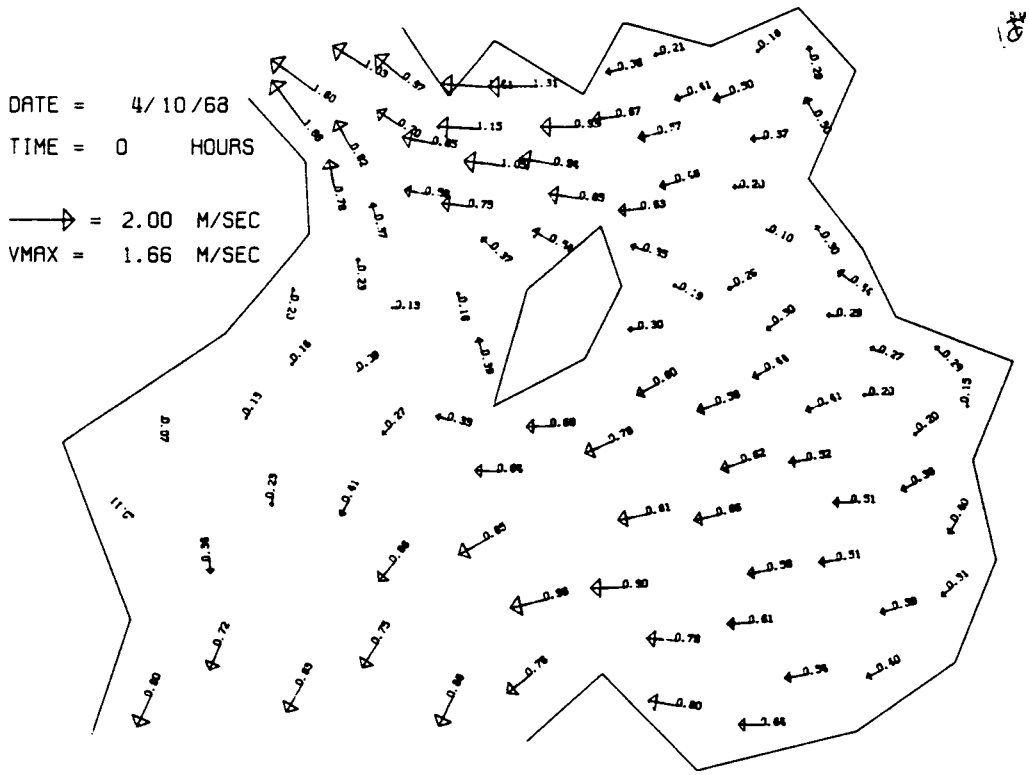

FIGURE 4.11. Maximum Ebb Currents Predicted by CAFE During One Tidal Cycle

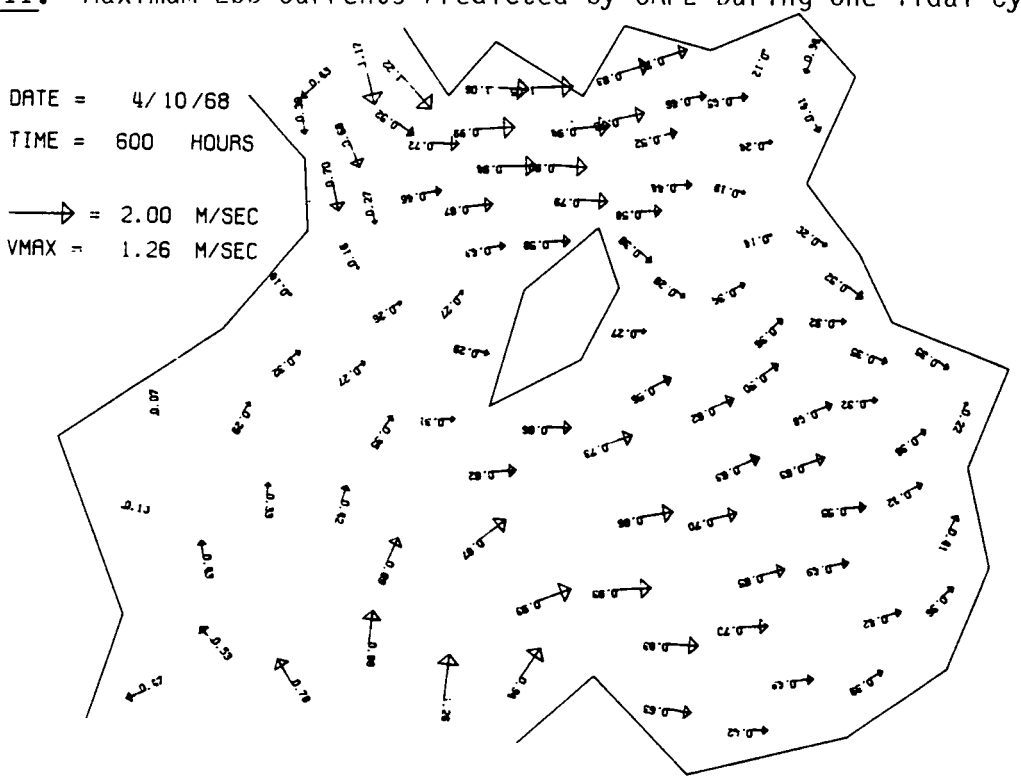

FIGURE 4.12. Maximum Flood Currents Predicted by CAFE During One Tidal Cycle

4.2.2.2 Quantitative Evaluation

Velocity ellipses provide a more quantitative means of comparing simulation results with measured data. For the quantitative evaluation we compared our simulation results with flow velocity field data that were obtained from the Institute of Oceanographic Sciences in the United Kingdom. Figure 4.13 shows the locations of the five flow velocity stations at which measurements were made in April 1968. Each station was sampled at more than one depth, generally at about 13 m from the surface, mid-water depth, and 5 m above the bottom. (The sea floor depth at current meter station 1 is 46 m; stations 2 to 5 range from 29 to 35 m in depth.) Velocities were recorded (at 10-min intervals) for 10 to 12 days at four of the stations and for 3 to 4 days at the remaining station (station 1).

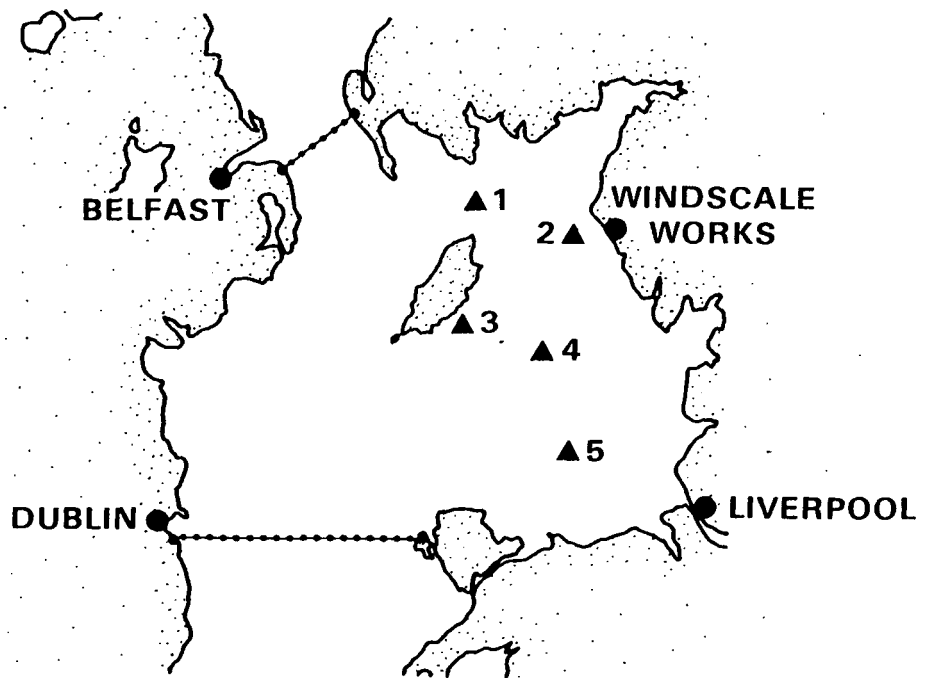

FIGURE 4.13. Locations of Recording Current Meters

Figures 4.14 and 4.15 indicate the change in flow velocity magnitude and direction with depth at each of the sampling stations. The figures show the maximum flood and ebb velocities, respectively, during one tidal cycle. The actual magnitudes are listed in Table 4.1. The flow directions are not significantly different at the various depths at a given point and thus the vertically-averaged velocities predicted by CAFE should be fairly representative of actual velocities at a given point. Note that the maximum velocity north of the Isle of Man is 0.8 m/sec to 0.9 m/sec, which is consistent with the velocity shown in Figure 4.10 for that flow region.

FIGURE 4.14. Change in Flow Velocities with Depth for Maximum Flood Current

FIGURE 4.15. Change in Flow Velocities with Depth for Maximum Ebb Current

TABLE 4.1. Flow Velocities Measured at Different Depths for Maximum Flood Current and Maximum Ebb

Station	Depth	Flow Velocities (m/sec) Ebb	Flood
1	.3-.4 D[(d)]	0.876	0.750
	.6-.7 D	0.745	0.781
	.8-.9 D		
2	.3-.4 D	0.222	0.187
	.6-.7 D	0.180	0.018
	.8-.9 D	0.186	0.130
3	.3-.4 D	0.594	0.552
	.6-.7 D	0.552	0.486
	.8-.9 D	0.451	0.468
4	.3-.4 D	0.421	0.498
	.6-.7 D	0.354	0.378
	.8-.9 D	0.288	0.312
5	.3-.4 D	--	--
	.6-.7 D	0.529	0.451
	.8-.9 D	0.318	0.330

(d) D = water depth

For our quantitative evaluation, we compared hodographs (or velocity ellipses) derived from the simulated velocities with those derived from the measured data. A hodograph represents the rotation of the velocity vector at a given point over one tidal cycle. Previous studies have noted that in most parts of the Irish Sea, the ratio of the minor axis of the velocity ellipse to the major axis is less than 0.1 (Robinson 1979; Bowden 1955). Exceptions are found in the flow regions off Morecambe Bay and the Cumbrian coast (near Windscale), where the ratio reaches 0.6 (Robinson 1979). Figure 4.16 shows the value of the ratio at various points in the study region. The higher-valued ratios are associated with weaker and more rotatory (almost circular) currents.

Hodographs were plotted for the measured data at each sampling point (including the different depths) and also for depth-averaged velocities at each of the five points. Hodographs based on the simulated velocities were plotted for the grid points shown in Figure 4.17. Note that the points (represented by circles) are either on a node or in the center of an element.

Figures 4.18 and 4.19 show the hodograph comparisons for stations 1 and 2. Note that the shapes of the hodographs are consistent with the findings noted above regarding the minor axis to major axis ratio at different locations. Station 1, located north of the Isle of Man, has a large major axis relative

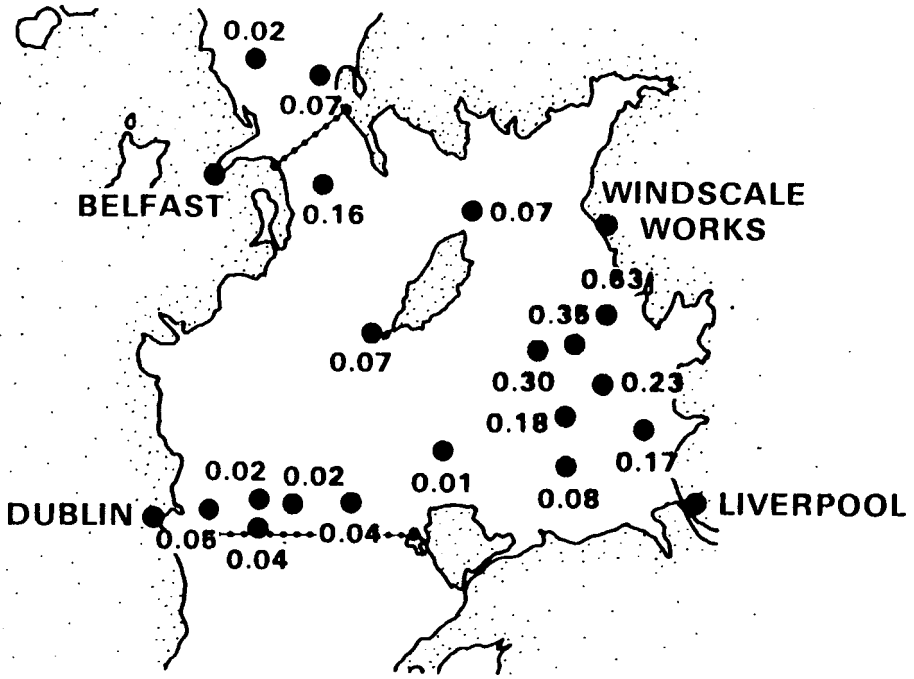

FIGURE 4.16. Velocity Ellipse Information for the M_2 Tidal Constituent (the numbers indicate the ratio of the minor axis to the major axis) (after Robinson 1979)

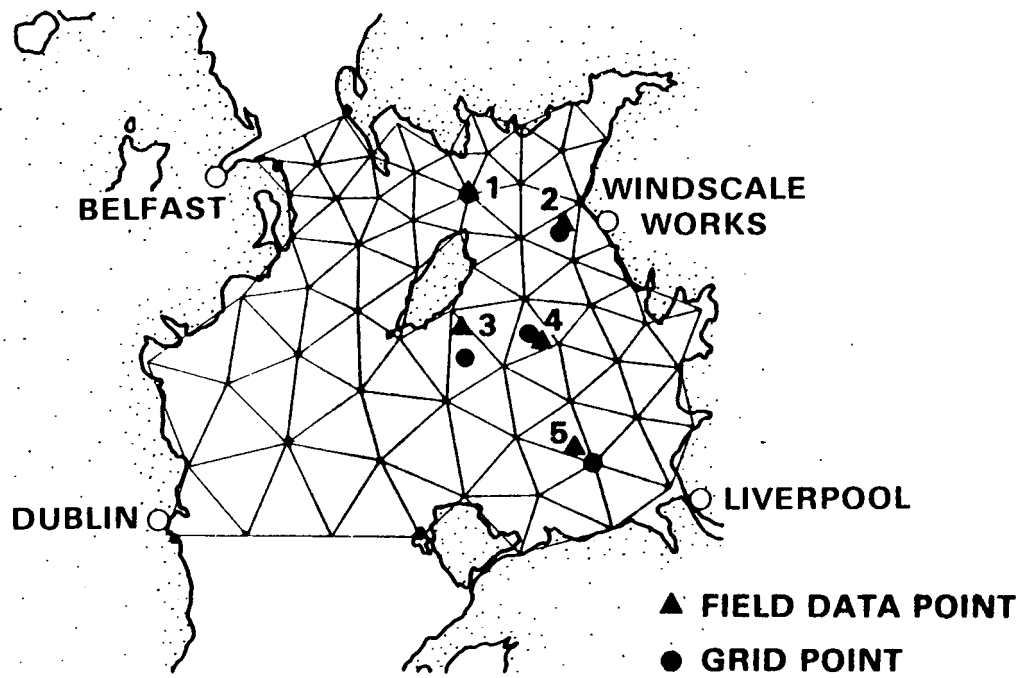

FIGURE 4.17. Points Used in the Hodograph Comparisons

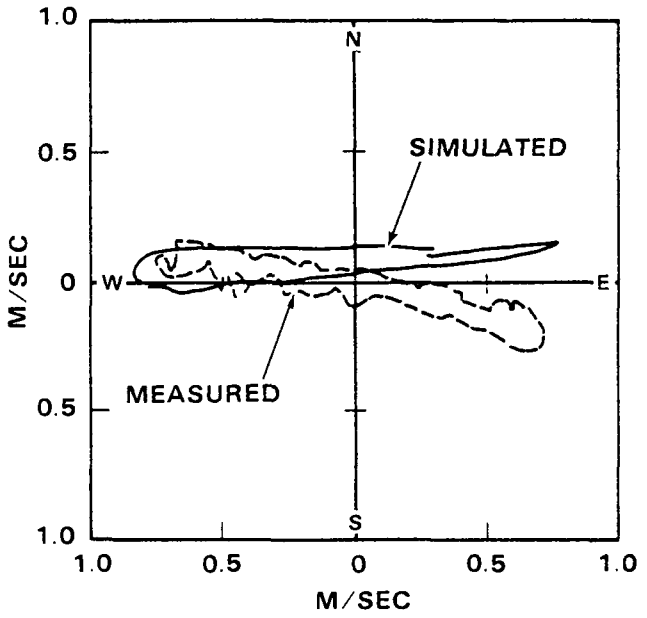

FIGURE 4.18. Hodograph Comparison - Station 1

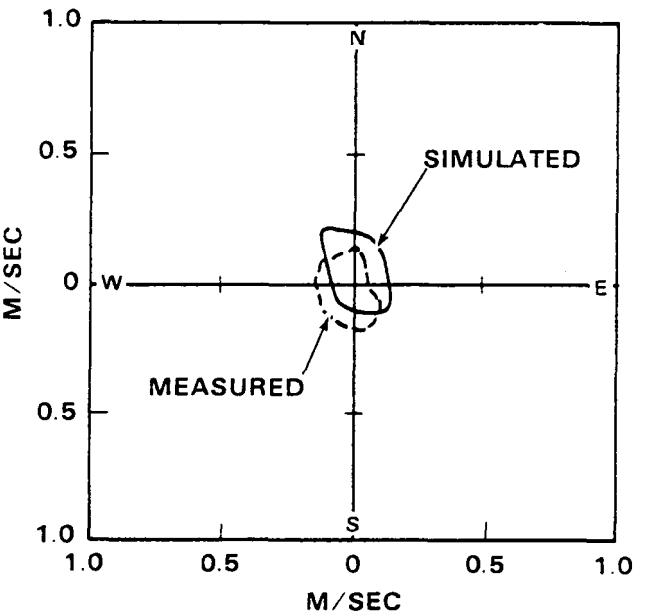

FIGURE 4.19. Hodograph Comparison - Station 2

to the minor axis and thus a small ratio. In contrast, point 2, located near Windscale, has a relatively large ratio resulting from the weaker and more rotatory currents. Note that the maximum flood and ebb current velocities at Station 1 are 0.8 m/sec to 0.9 m/sec (as we also noted in Figures 4.20 through 4.22, for the field data only), which is consistent with information presented above in regard to Figure 4.10.

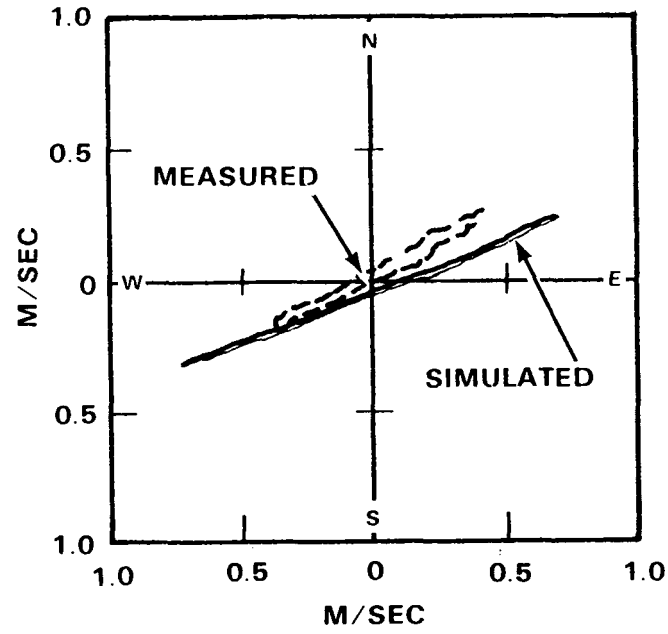

FIGURE 4.20. Hodograph Comparison - Station 3

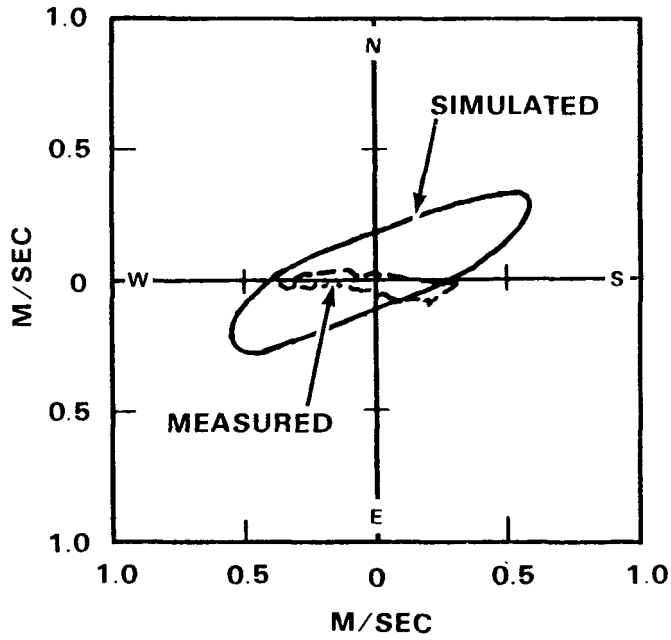

FIGURE 4.21. Hodograph Comparison - Station 4

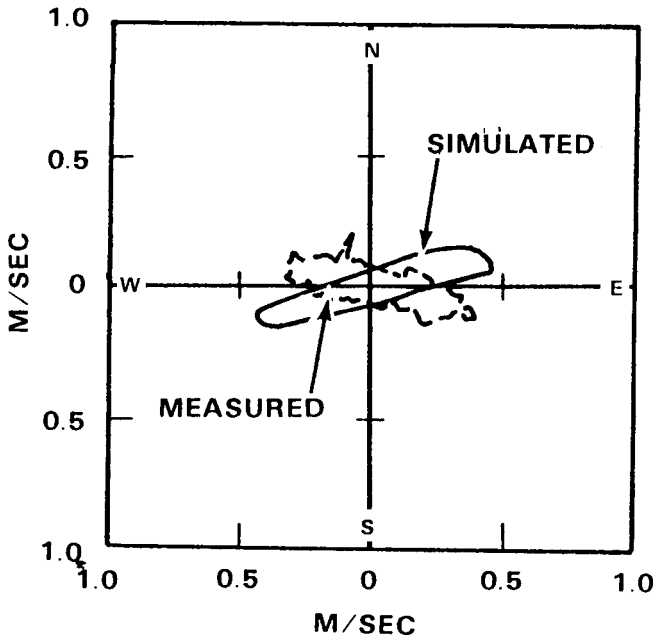

FIGURE 4.22. Hodograph Comparison - Station 5

The simulated and measured velocity magnitudes are well matched at both Stations 1 and 2. The simulated and measured velocity directions also show reasonable agreement at Station 2; at Station 1 the simulated flood currents are oriented 30° closer to the north than the corresponding measured data.

Figures 4.20 and 4.21 show the hodograph comparisons for Stations 3 and 4. At Station 3 the orientation of the hodographs is fairly close, although the simulated flood currents are approximately 15° closer to the south than the measured velocities. Comparing the amplitudes (i.e., magnitudes) of the maximum flood and ebb currents, the maximum simulated values are 45% and 90% higher than the maximum field values for flood and ebb, respectively. The hodographs at Station 4 show poor agreement. The maximum simulated velocities are 50% to 100% greater than maximum measured velocities, and the simulated velocities are oriented about 25° counterclockwise from the field velocities. In other words, the simulated velocities are oriented toward the Northeast and Southwest, whereas the measured velocities are oriented due West and East, on flood tide pointing toward Morecambe Bay.

Figure 4.22 shows the hodograph comparison for Station 5. The simulated and measured velocity magnitudes are in good agreement at this location, but the simulated velocities are again oriented 25° to 30° counterclockwise from the measured velocities. Note that the maximum simulated velocities are oriented parallel to the grid boundary, whereas the maximum measured velocities point into and away from Liverpool Bay. Thus, the simulated velocities may be constrained at this location by the coarse discretization.

The computed and observed phases (i.e., time of occurrence) of the maximum flood and ebb currents were also compared. At Stations 1, 2, and 5, the computed and observed phases were very close, the largest difference being

approximately 0.4 hr. At Stations 3 and 4 the computed and observed phases differed by less than an hour, except for a 1.4 hr difference on ebb tide at Station 4.

4.2.2.3 Results of 1974 Simulation Period

A 75-day CAFE simulation was run for the 1974 period, to be used for the FETRA application. Input parameters were the same as those used in the calibration, with the exception of the boundary and initial conditions. The time-varying water surface elevations for the open boundaries (i.e., the boundary conditions) were again obtained from NOS tide tables (U.S. Department of Commerce 1973). To overcome the effect of the assigned initial conditions (i.e., initial water surface elevations), the model was run for two tidal cycles before saving the output. Figures 4.23 and 4.24 show maximum flow velocities simulated by CAFE for two different times in July 1974. The simulated flow velocities and patterns are consistent with the calibration results.

4.2.3 Summary

We found that varying the bottom roughness, the diffusivity, and the wind magnitude and direction had little effect on either predicted flow velocities or predicted water surface elevations. Therefore, no adjustments were made in these input parameters. The changing water surface elevation due to tides was the sole driving force for the simulated hydrodynamics.

We compared simulated and observed general flow patterns and simulated and observed velocity ellipses; in the latter comparison, we focused on the amplitude, direction, and phase of the maximum flood and ebb currents. The CAFE results for the calibration period showed good agreement with the general circulation pattern and reasonable agreement with flow velocities. To improve our hydrodynamic results, we would probably need to 1) use a finer grid and 2) investigate more fully what effect changes in the boundary conditions (specified water surface elevations) would have on the flow field.

4.3 SEDIMENT AND RADIONUCLIDE TRANSPORT SIMULATION

This section describes the input data used for FETRA, the sensitivity of FETRA to these input data, and the FETRA simulation results. For this study, the following seven substances were simulated: 1) sand, 2) silt, 3) clay, 4) dissolved ^{137}Cs, 5) ^{137}Cs sorbed by sand, 6) ^{137}Cs sorbed by silt, and 7) ^{137}Cs sorbed by clay.

4.3.1 Input Data Description

The FETRA input data stream is comprised of the following eight categories:

1. numerical model parameters
2. model area discretization
3. fluid and flow characteristics

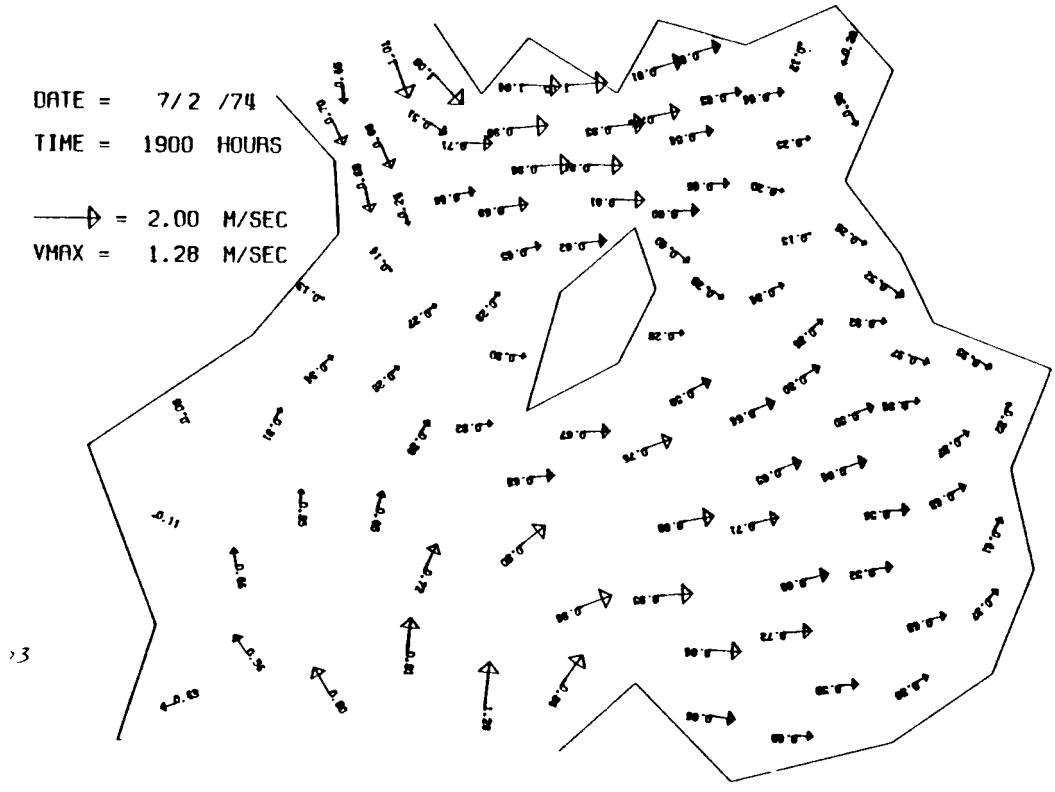

FIGURE 4.23. Maximum Flood Currents Predicted by CAFE During One Tidal Cycle in July 1974

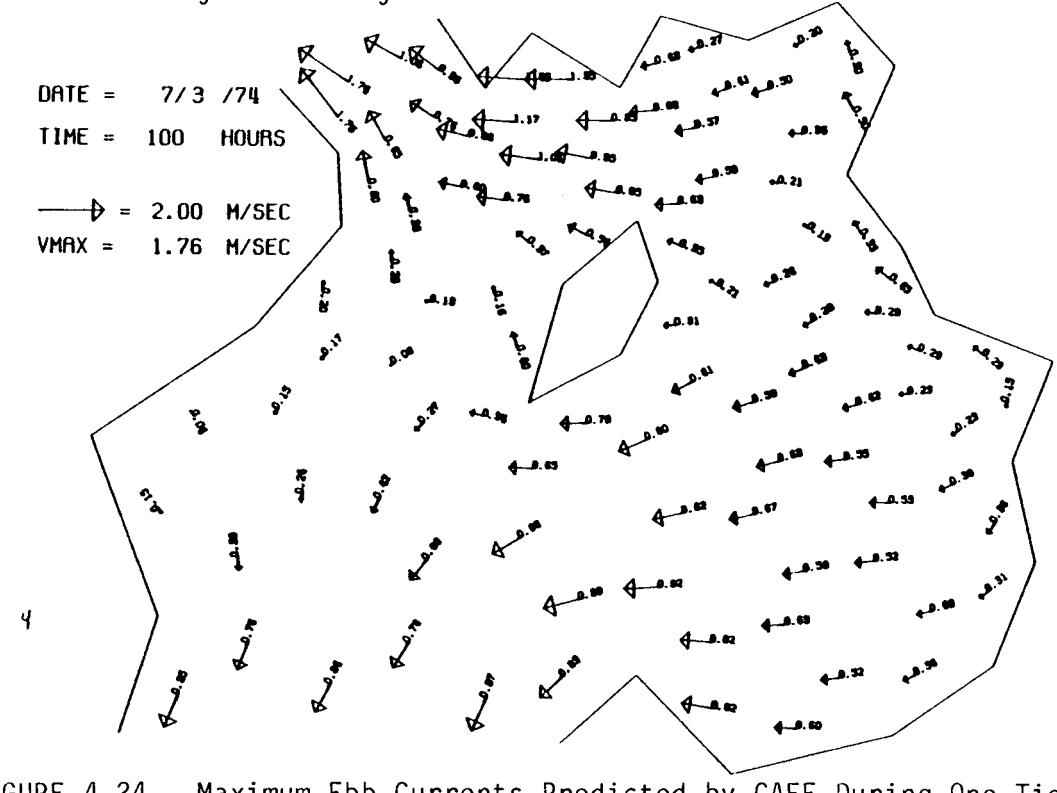

FIGURE 4.24. Maximum Ebb Currents Predicted by CAFE During One Tidal Cycle in July 1974

4. wind/wave characteristics
5. sediment characteristics
6. radiochemical parameters
7. initial conditions
8. boundary conditions

We will briefly discuss the input data required by the model.

Numerical Model Parameters

The numerical model parameters assigned by FETRA are

- number of substance set to seven
- number of timesteps set to 1500
- timestep size set to one hour
- fully implicit time-dependent numerical computations to be set.

Model Area Discretization

The FETRA model discretization is the same as that of CAFE, as shown in Figure 4.4. However, unlike CAFE, FETRA has six nodes (three corner nodes and three internal nodes) for each element. The total number of elements and nodes used by FETRA were 96 and 226, respectively. Channel bed parameters (i.e., the number of initial bed layers and standard thickness of each bed layer for each element) were assigned to be 4 and 20 cm, respectively. However, the top bed layer for each element was originally assigned to be 10 cm.

Fluid and Flow Characteristics

Fluid and flow characteristics used by FETRA were

- water viscosity set equal to 1.25×10^{-6} m^2/s
- water density set equal to 1000 kg/m^3
- flow velocity and depth at each node to be supplied by CAFE.

Wind/Wave Characteristics

The FETRA model either internally calculates characteristics of waves generated by wind or accepts wave characteristics estimated by other computer programs [e.g., the LO3D wave refraction model reported by Ecker and Degraca (1974)] for each computational node. For this study, wave characteristics were

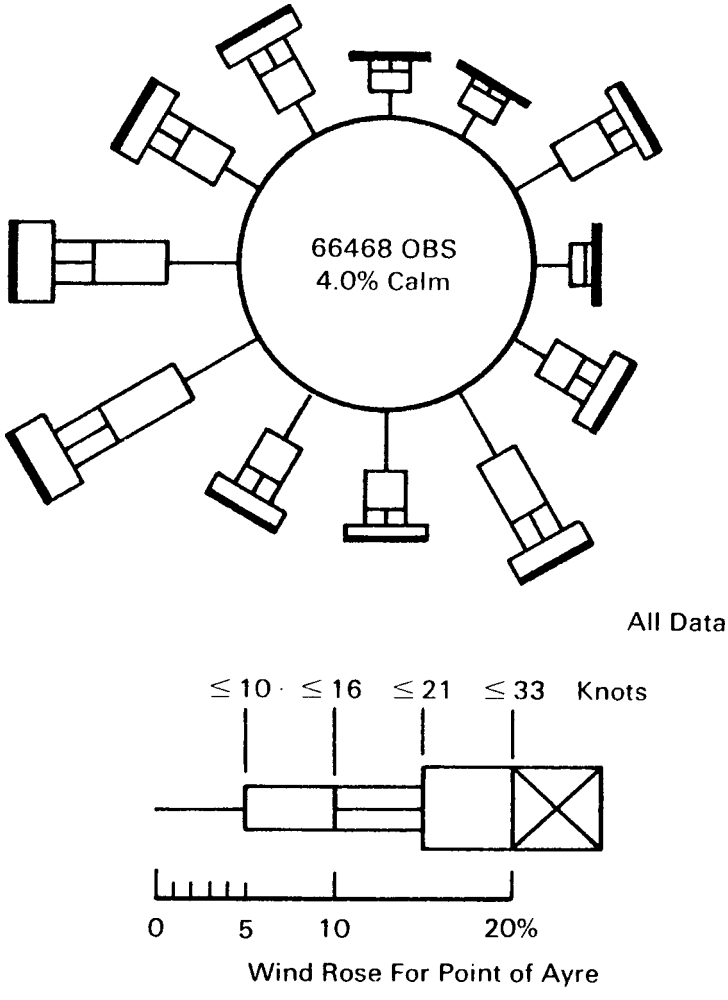

FIGURE 4.25. Wind Rose for Point of Ayre

internally computed. A wind rose for the Point of Ayre, located at the northern tip of the Isle of Man, is shown in Figure 4.25. For an actual production run, the following data were assigned:

- wind speed to be constant 6.7 m/s, which is the annual average wind speed
- wind direction to be east-northeast, which is the predominant wind direction
- effective fetch length and fetch depth assigned for each node.

Sediment Characteristics

The sediment characteristics input to FETRA were

- sediment diameter

- sediment particle density
- sediment fall velocity
- critical shear stresses for deposition of cohesive sediments
- critical shear stresses for erosion of cohesive sediments
- erodibility coefficient of cohesive sediments
- longitudinal and lateral dispersion coefficient
- porosity of bed sediment.

In the present application of FETRA to the Irish Sea, three sediment sizes representing sand, silt, and clay sediment fractions were used in the simulation. The sediment characteristics selected for this study are shown in Table 4.2.

Radiochemical Parameters

The radionuclide parameters used in this modeling study are

- distribution coefficient
- radionuclide transfer rate
- radionuclide decay rate
- radionuclide release rate.

FETRA requires the distribution coefficient, K_d, for each sediment size fraction. Jefferies (1968) reported that distribution coefficients for surface sand and surface silt collected from Ravenglass Estuary in 1965 and 1966 were 60 mℓ/g and 800 mℓ/g, respectively. Hetherington and Jefferies (1974) also reported the relationship between ^{137}Cs concentrations and sediments collected from the Eskmeals area in Ravenglass Estuary, as shown in Table 4.3. It is well known that more time is required for bed sediment to reach equilibrium with dissolved radionuclides than for similar suspended sediment (Onishi et al. 1981). However, because data on the amount of time required to reach equilibrium with dissolved ^{137}Cs were not available for either suspended or bed sediments, we assumed that these sediments reach equilibrium at the same time as expressed by the values of radionuclide transfer rates. This assumption will overpredict the amount of radionuclides adsorbed by bed sediment within a given time. Based on these data, the radiochemical parameters were selected, as summarized in Table 4.4.

TABLE 4.2. Sediment Characteristics

	Sand	Silt	Clay
Diameters, m	2.5×10^{-4}	1.72×10^{-5}	2.0×10^{-6}
Fall Velocity, m/s	3.0×10^{-2}	2.0×10^{-4}	2.75×10^{-6}
Porosity	0.5	0.5	0.5
Longitudinal Dispersion Coefficient, m^2/s	0.1	0.1	0.1
Lateral Dispersion Coefficient, m^2/s	0.1	0.1	0.1
Erodibility, $kg/m^2/s$	N.A.	1.0×10^{-10}	1.0×10^{-10}
Critical Scour Shear Stress, kg/m^2	N.A.	0.9	2.0
Critical Deposition Shear Stress, kg/m^2	N.A.	0.05	0.01

N.A. = not applicable.

TABLE 4.3. Cesium-137 Concentrations in Each Size Fraction of Eskmeals Estuary Sediment, Normalized to ^{137}Cs Concentration in Coarse Sand (Hetherington and Jefferies 1974)

	Coarse Sand	Fine Sand	Silt	Clay
Weight, %	2.5	12.5	70	15
Loss in Ignition, %	1	2.8	6.3	16.0
Normalized ^{137}Cs Concentration	1	2.9	5.9	11.1

TABLE 4.4. Radiochemical Parameters

	Distribution Coefficient, mℓ/g
Sand	60
Silt	600
Clay	1200
	Radionuclide Transfer Rate, 1/day
Suspended Sand	3.0
Suspended Silt	3.0
Suspended Clay	3.0
Bed Sand	3.0
Bed Silt	3.0
Bed Clay	3.0
^{137}Cs Decay Rate, 1/day	6.3×10^{-5}
^{137}Cs Release Rate, Ci/day	301

Initial Conditions

FETRA was assigned the following initial conditions;

- suspended sediment concentrations for sand, silt, and clay set equal to 1, 3, and 1 mg/ℓ, respectively
- ^{137}Cs sorbed by suspended sand, silt and clay set equal to zero
- dissolved ^{137}Cs concentration set equal to zero
- ^{137}Cs sorbed by bed sand, bed silt, and bed clay set equal to zero
- bed sediment size distribution set equal to that shown in Figure 4.26 reported by Williams et al. (1981) and Pentreath et al. (1983).

Because we did not have ^{137}Cs distributions in the sea bed for either 1973 or 1974, FETRA could not include initial effects of interaction between dissolved ^{137}Cs and bed sediment. To avoid this problem, we assumed that no ^{137}Cs was

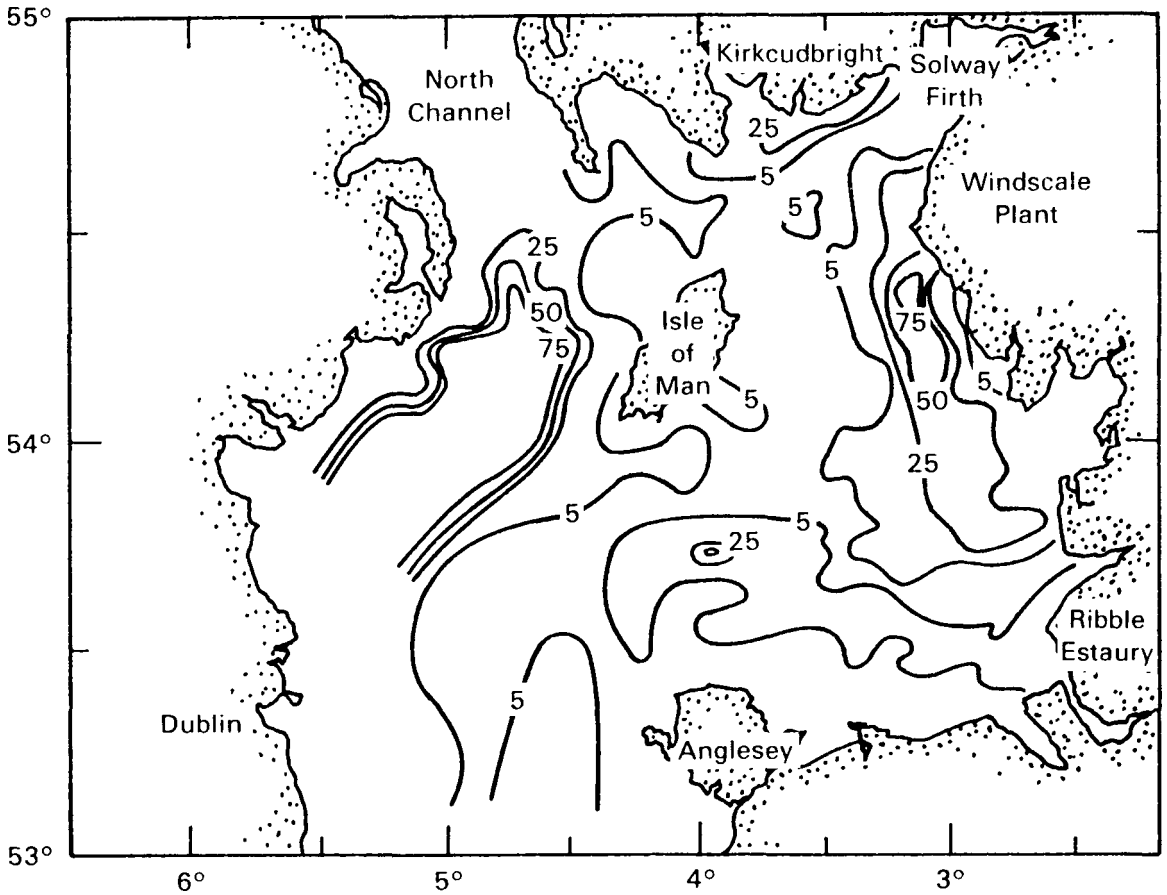

FIGURE 4.26. Distributions of System Sediments in the Irish Sea, Expressed as Percent by Weight of Sediment Finer Than 0.0625 mm (Williams et al. 1981)

initially present in the water column nor in the bed of the Irish Sea. Hence, the ^{137}Cs simulation results by FETRA should be regarded as an incremental difference over the 1973 condition.

Boundary Conditions

The boundary conditions in FETRA were

- time-varying flows and depths at the boundaries supplied by CAFE
- suspended-sediment concentrations of sand, silt, and clay set equal to 1, 3 and 1 mg/ℓ, respectively
- dissolved ^{137}Cs set equal to zero
- ^{137}Cs sorbed by suspended sand, silt, and clay set equal to zero.

4.3.2 Sensitivity Analysis

As a part of the evaluation of FETRA behavior, sensitivity analyses were performed for the Irish Sea study case. As indicated in Section 4.3.1, the only model parameters and coefficients of FETRA that can be adjusted to fit to measured data are the dispersion coefficients and three parameters for cohesive sediment erosion and deposition (critical shear stresses for erosion and deposition, and the erodibility coefficient).

Dispersion coefficients were changed from 0.01 m^2/s to 10,000 m^2/s for the sensitivity analysis. This wide range of dispersion coefficients, of course, changed ^{137}Cs concentrations. However, considering the large variation of the dispersion coefficient, the sensitivity analysis indicates that a dispersion coefficient within a reasonable range is not one of the most important parameters, especially when the radionuclide migration is dominated by advection.

Three parameters for cohesive sediment erosion and deposition strongly affected the fine sediment distributions in the water column and sea bed and, thus, affected the transport, deposition and erosion of sediment-sorbed radionuclides. For example, silt and clay concentrations almost linearly increase with the erodibility coefficient once the bed shear is above the critical shear stress of erosion. These parameters are the least well-known because cohesive sediment erosion and deposition are not well understood. Field and laboratory studies are needed to improve the understanding of cohesive sediment transport characteristics. However, when radionuclides have little affinity to sediment (e.g., have a small distribution coefficient), the importance of these parameters to the resulting total radionuclide concentration is lessened.

Although other model parameters and coefficients should not be arbitrarily changed to match measured data, we tested the sensitivity of FETRA to many of these parameters. These include the distribution coefficient, K_d; radionuclide transfer rate, K_j; sediment size, D_{50}; and wind velocity. As expected, FETRA results were very sensitive to these parameters and so they must be carefully selected. As an example, the effects of wind on sand concentrations at wind speeds of 6.7 and 50 m/s over three-day periods are shown in Figure 4.27 and 4.28, respectively. Note that solid lines in these figures indicate the Irish Sea study area boundary, while dashed lines represent computed concentration contours. Because of the interpolation method used for plotting, concentration contour lines sometimes crossed over the study boundary. For the 6.7-m wind case, sand concentrations are generally less than 1 mg/ℓ, except near the beach along the east side of the study area (Liverpool and Morecambe Bays). In these bay areas, sand concentrations reached up to 100 mg/ℓ, owing to the long fetch lengths of east-southeasterly winds in the study region, and the relatively shallow flow depth near the beach. However, northeast of the Isle of Man, relatively small sand concentrations are present because the Isle of Man reduces the fetch lengths significantly. For the 50-m/s wind case, sand concentrations are much higher, because larger surface waves are generated by the higher wind speed. These sand concentration differences result from the different waves generated by the two winds. However, the large changes of sand concentrations changed the dissolved ^{137}Cs concentrations only slightly because sand has a small capacity to adsorb ^{137}Cs.

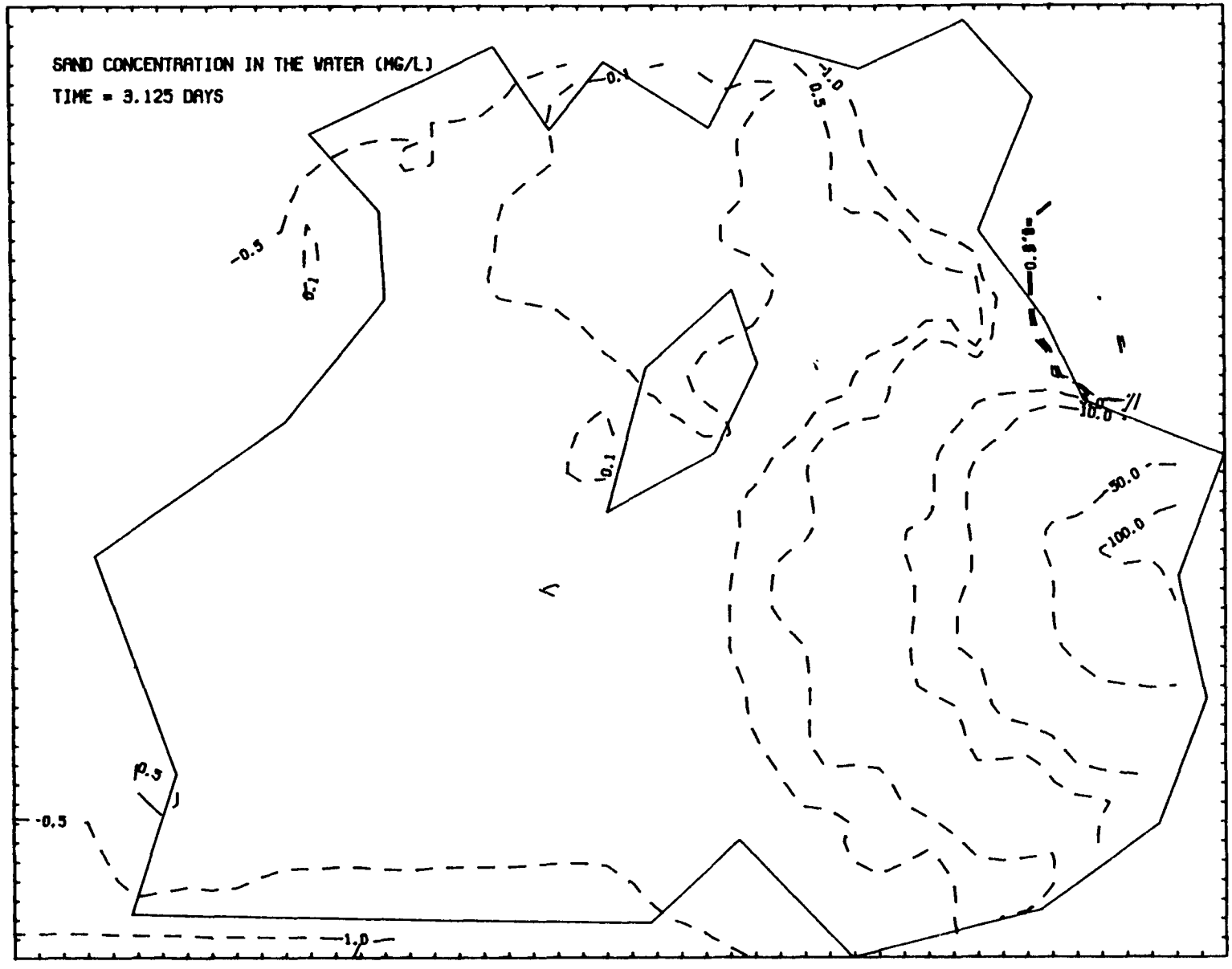

FIGURE 4.27. Computed Suspended Sand Concentrations for 6.7 m/s Wind Blowing 3.1 Days

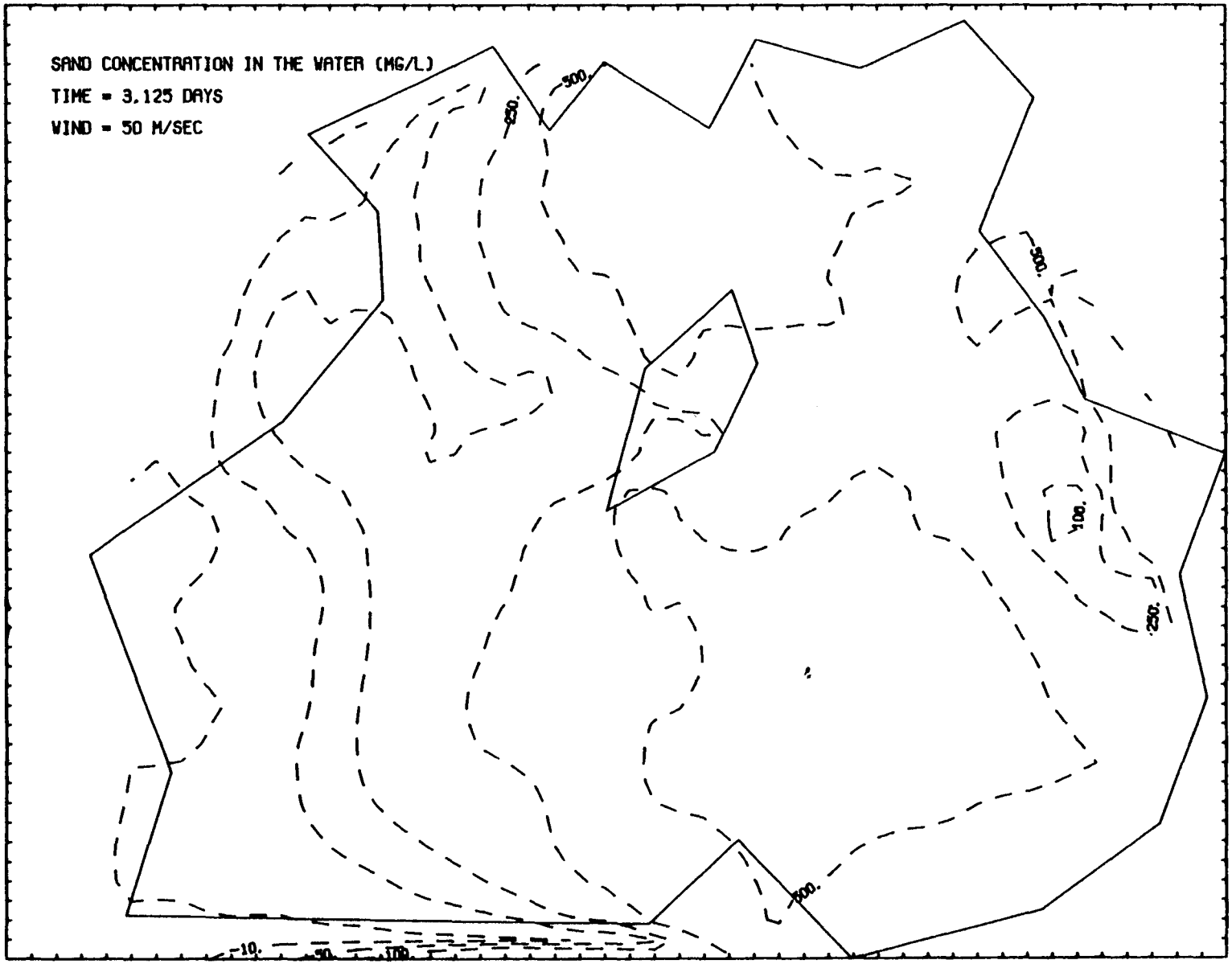

FIGURE 4.28. Computed Suspended Sand Concentrations for 50 m/s Wind Blowing 3.1 Days

These sensitivity analyses indicate that if sorbed radionuclides are important, then most of these parameters tested under this study are important. However, if radionuclides do not have high affinity for sediments, then almost all of the parameters and coefficients are even less important than the 'not-so-crucial' dispersion coefficients.

4.3.3 FETRA Application -- 1974

Using the input data described in Section 4.3.1, the FETRA model simulated sediment and ^{137}Cs distribution in the Irish Sea for 62.5 days with a one-hour time step. FETRA was implemented on a CDC 7600 computer to predict movements of the three sediment size fractions, dissolved ^{137}Cs and sediment-sorbed ^{137}Cs for each of the three sediment size fractions, as well as the sediment/radionuclide bed inventory. This calculation took a total of 52 milliseconds per time step per node. As reported in Onishi and Trent (1982), the finite difference three-dimensional model, FLESCOT, which simulates distributions of flow, water temperature, salinity, sediment, and radionuclides with their interactions, took only 6.3 milliseconds per time step per cell to compute all those values when it was applied to the Hudson River Estuary using the CDC 7600 computer. Although FETRA and FLESCOT have been applied to different sites, the difference in computational speed for these two studies are indicative of their compution speeds. The slowness of the two-dimensional model, FETRA, probably is caused mainly by its finite element computational scheme, as compared to the much more efficient finite difference scheme used by FLESCOT. Note that CAFE was run using a VAX 11/780 computer.

Predicted concentrations of suspended sand, silt, and clay, 15.6 days after the start are shown in Figures 4.29, 4.30, and 4.31, respectively. These concentrations are the sum of sediment concentrations of both suspended load and bed load. However, in this report, we call the sum of these two loads suspended sediment, in contrast to stationary bed sediment. Note that suspended sand concentrations are very small (mostly less than 1 mg/ℓ) except near and along the east-side beach of the Irish Sea similar to those after 3.1 days (Figure 4.27). There the wind-generated waves become strong enough and flow depths become shallow enough to suspend the bed sand up to concentrations of 120 mg/ℓ. However, suspended silt and clay concentrations are relatively uniform throughout the study area.

The computed total suspended-sediment concentrations (the sum of suspended sand, silt, and clay concentrations) were approximately 3 to 5 mg/ℓ, except near the east beach of the Irish Sea, as shown in Figure 4.32. Hetherington (1976) reported that the measured total suspended-sediment concentrations are usually between 0.5 and 10 mg/ℓ. However, wind-induced waves are known to stir the estuaries near and along the eastern beach of the Irish Sea and sometimes become a significant factor in transporting sediment-sorbed radionuclides.

Computed distributions of suspended sediment after 62.5 days, shown in Figure 4.33 through 4.36, are also very similar to those after 15.6 days, as discussed previously. This similarity of sediment concentrations indicates that the computed sediment concentrations reach quasi-equilibrium values.

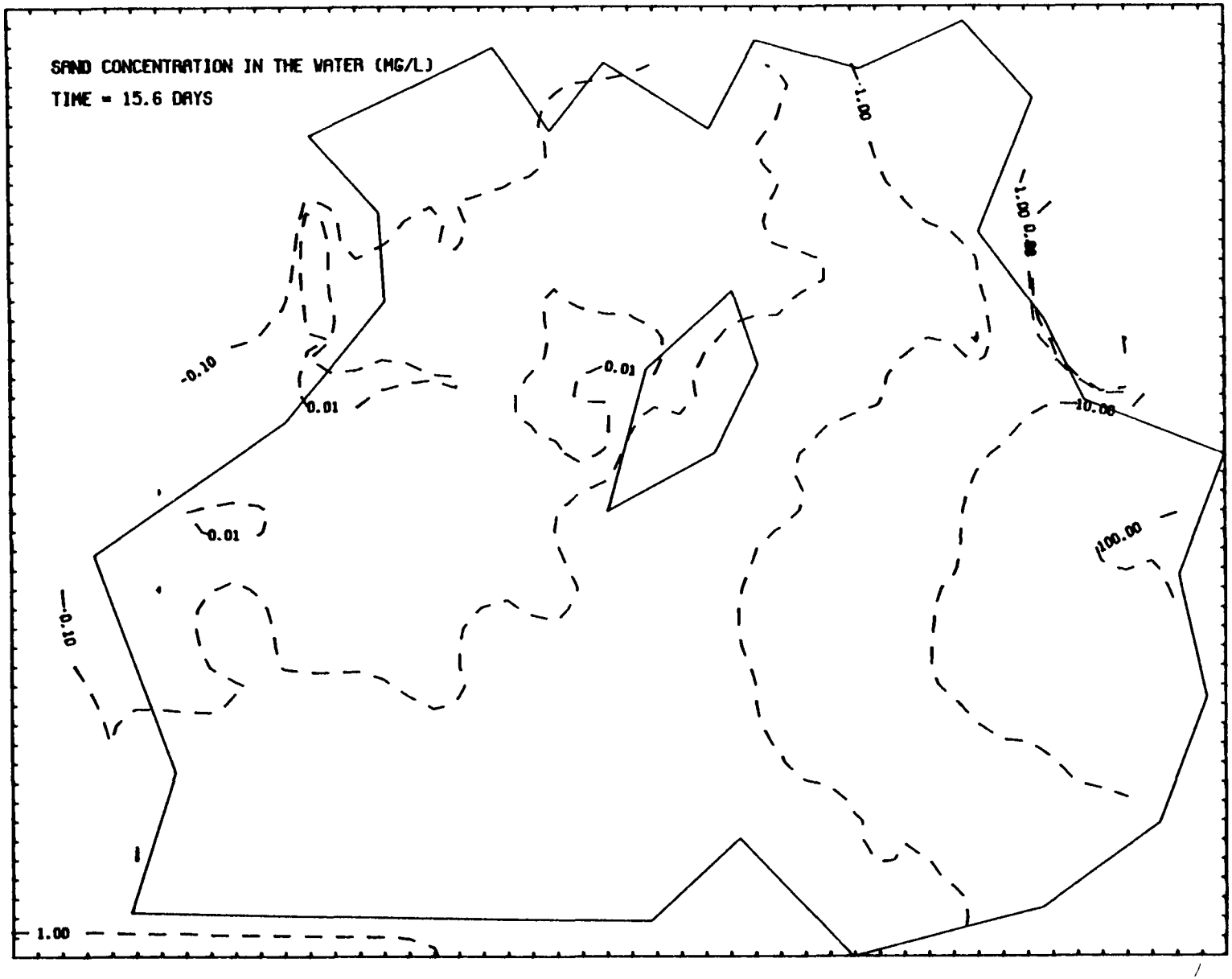

FIGURE 4.29. Computed Suspended Sand Concentrations After 15.6 Days of Simulation

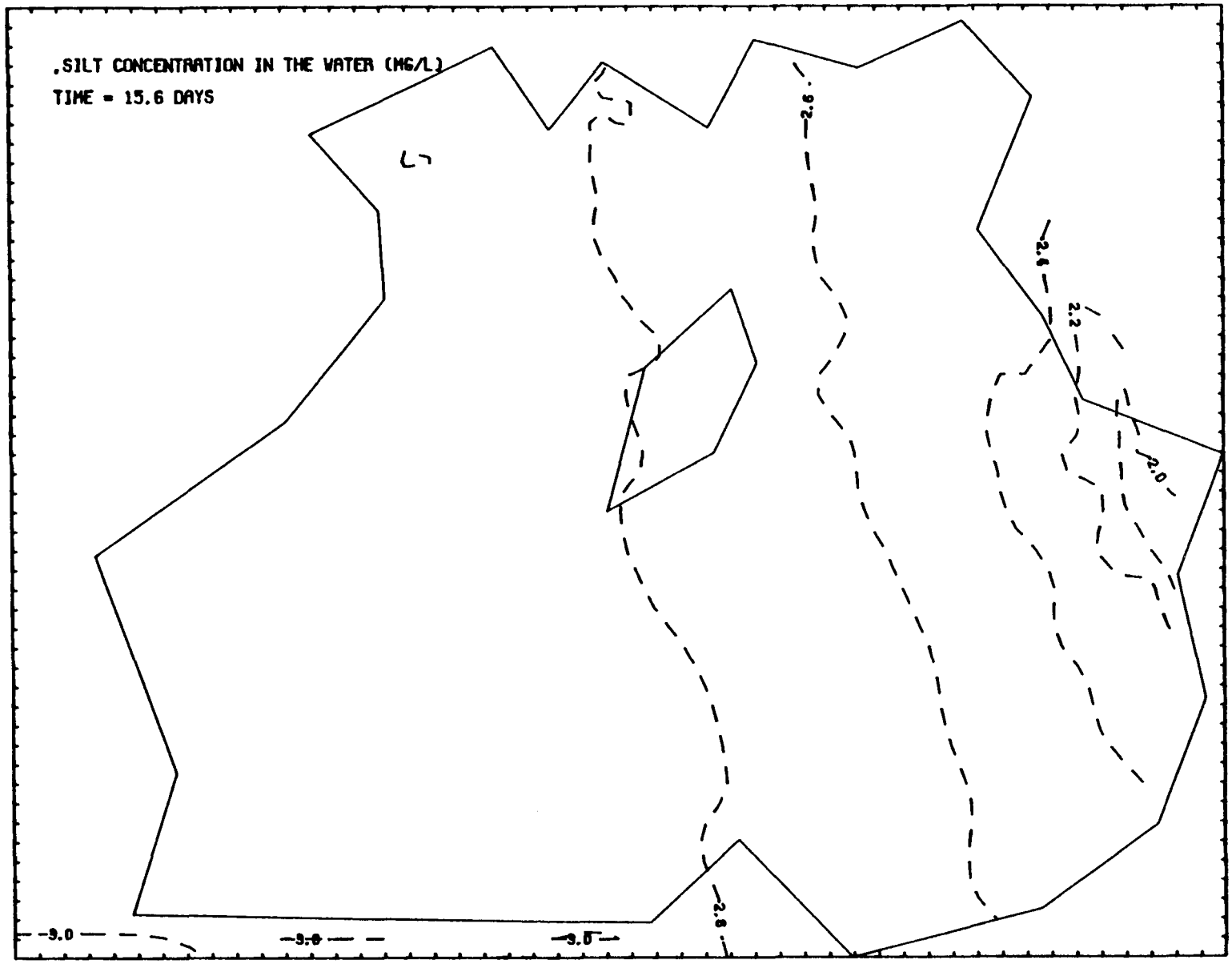

FIGURE 4.30. Computed Suspended Silt Concentrations After 15.6 Days of Simulation

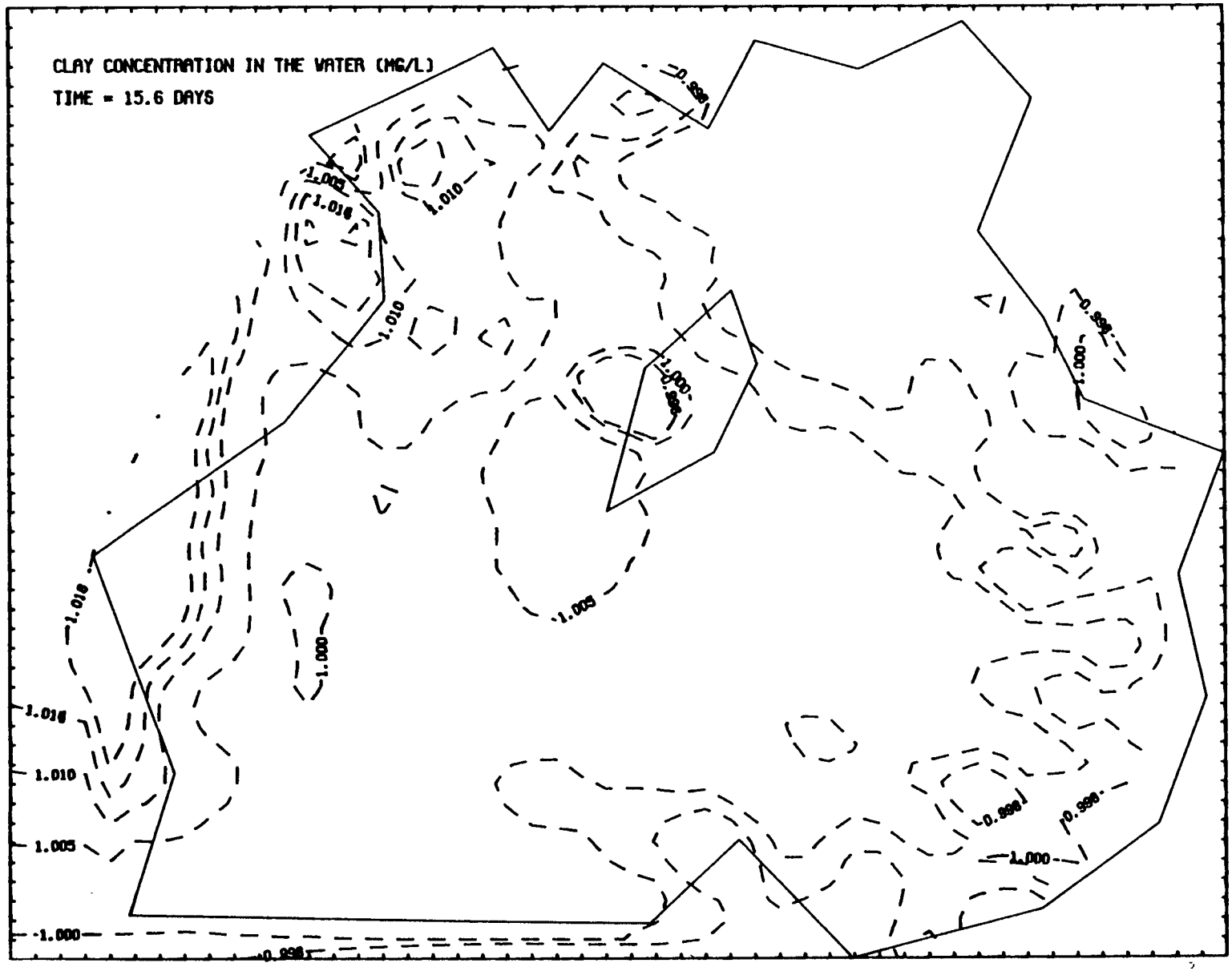

FIGURE 4.31. Computed Suspended Clay Concentrations After 15.6 Days of Simulation

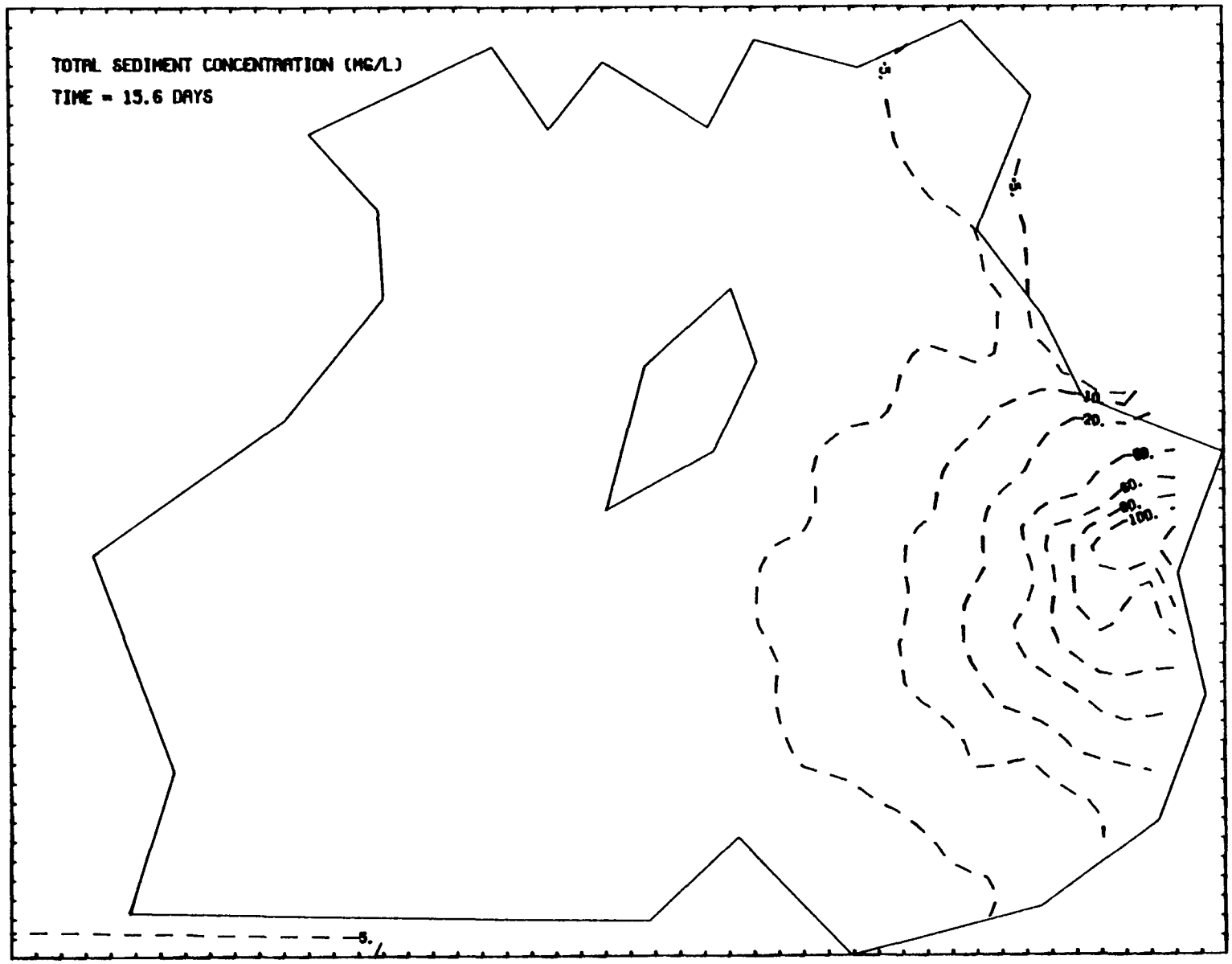

FIGURE 4.32. Computed Total Suspended Sediment Concentrations After 15.6 Days of Simulation

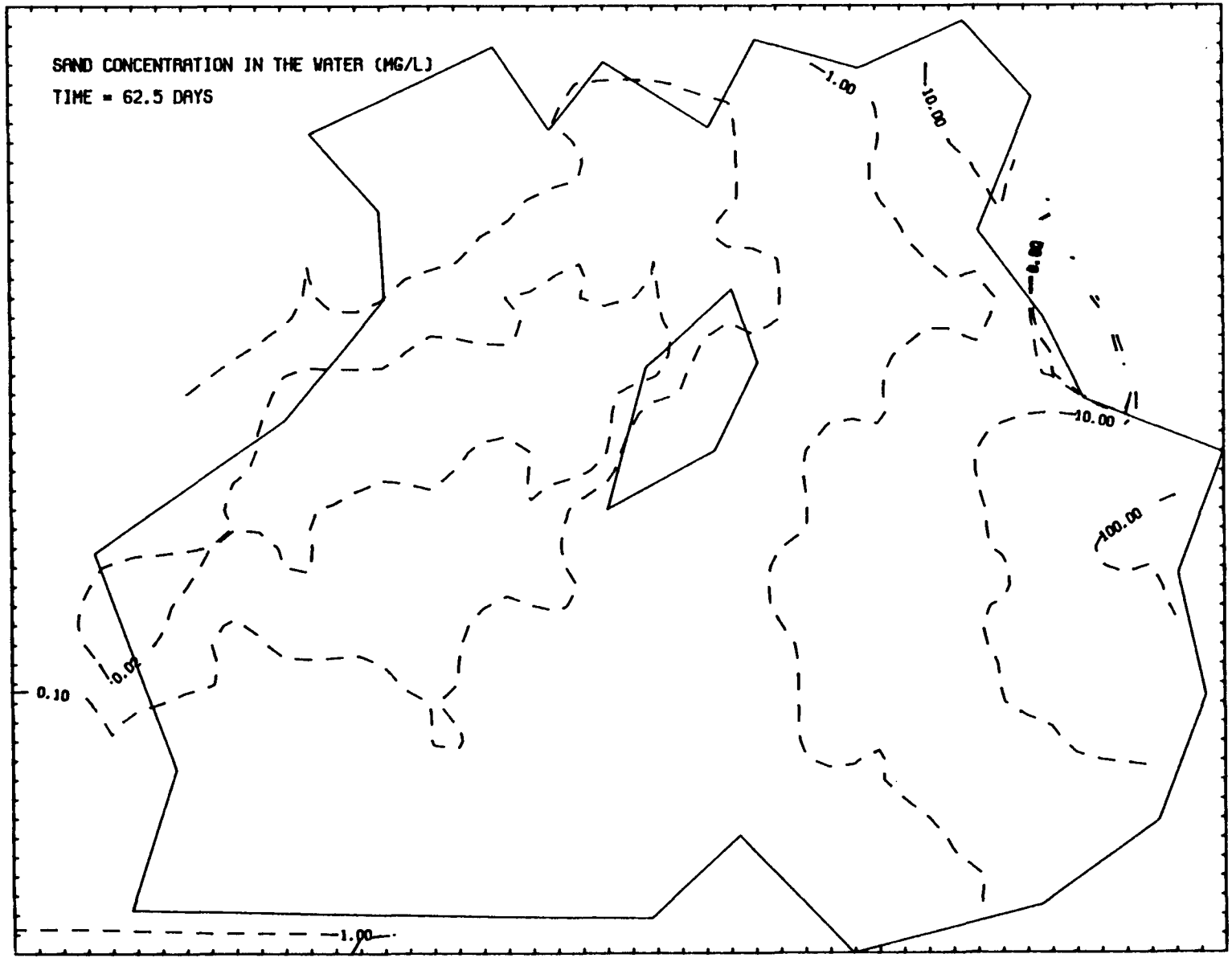

FIGURE 4.33. Computed Suspended Sand Concentrations After 62.5 Days of Simulation

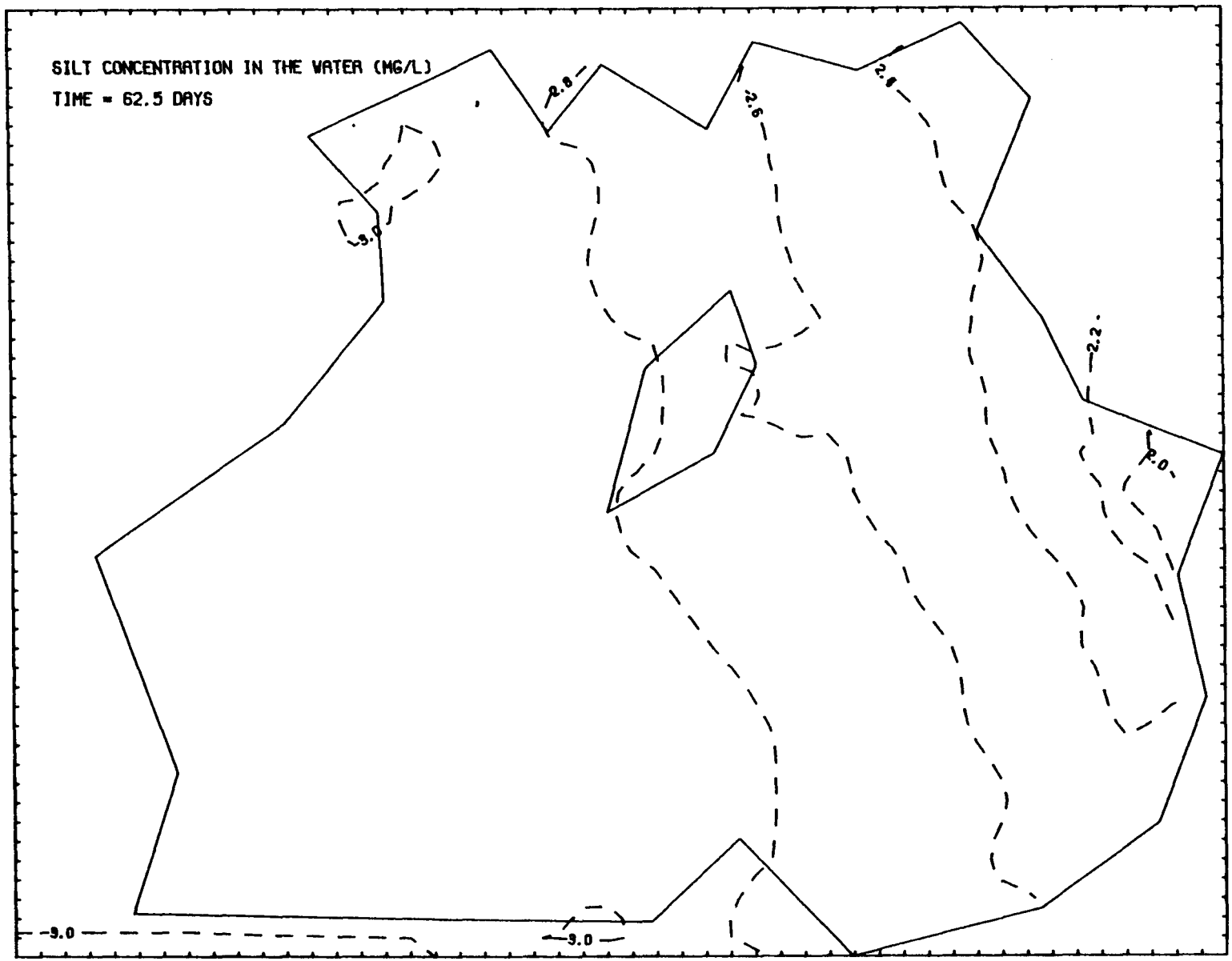

FIGURE 4.34. Computed Suspended Silt Concentrations After 62.5 Days of Simulation

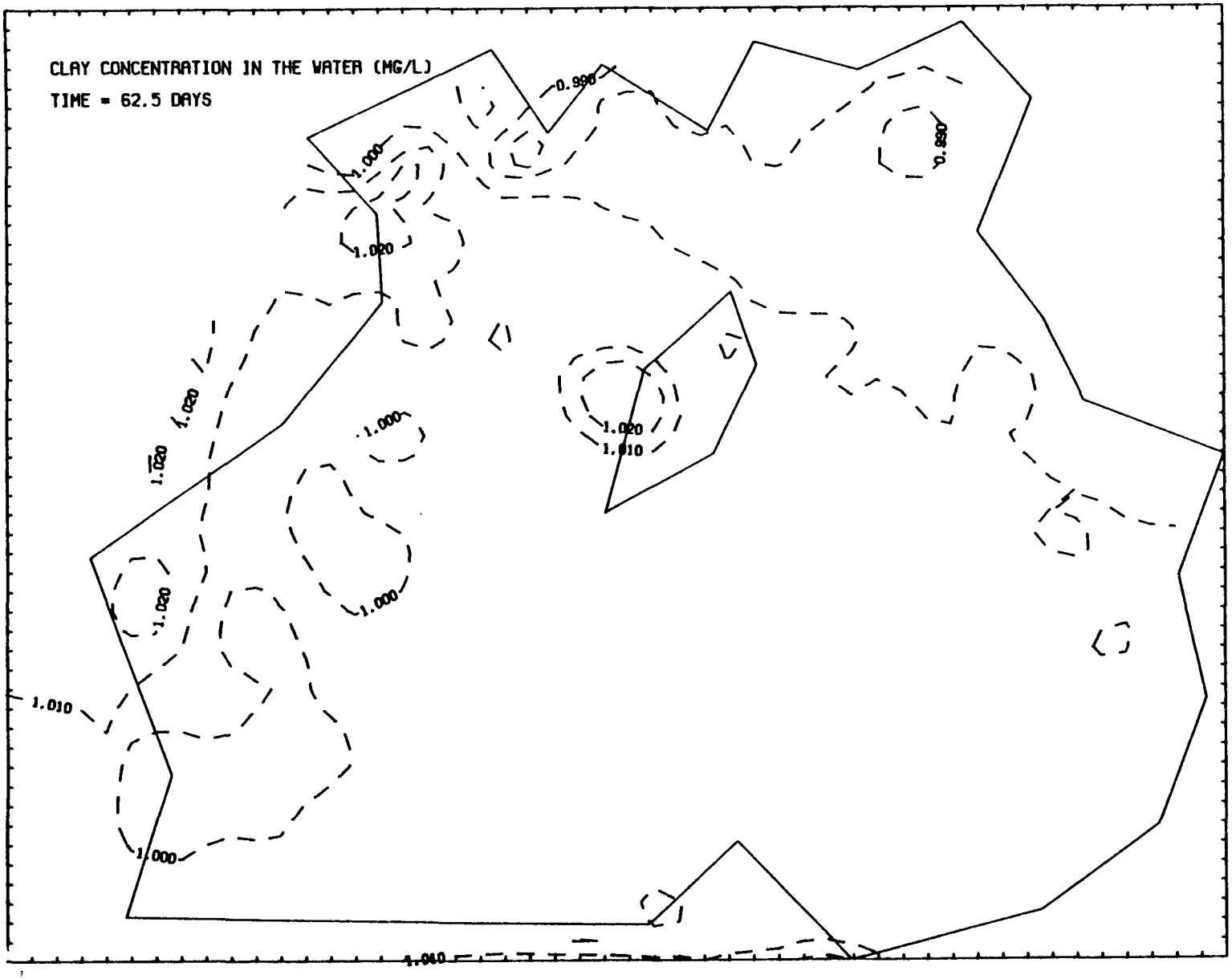

FIGURE 4.35. Computed Suspended Clay Concentrations After 62.5 Days of Simulation

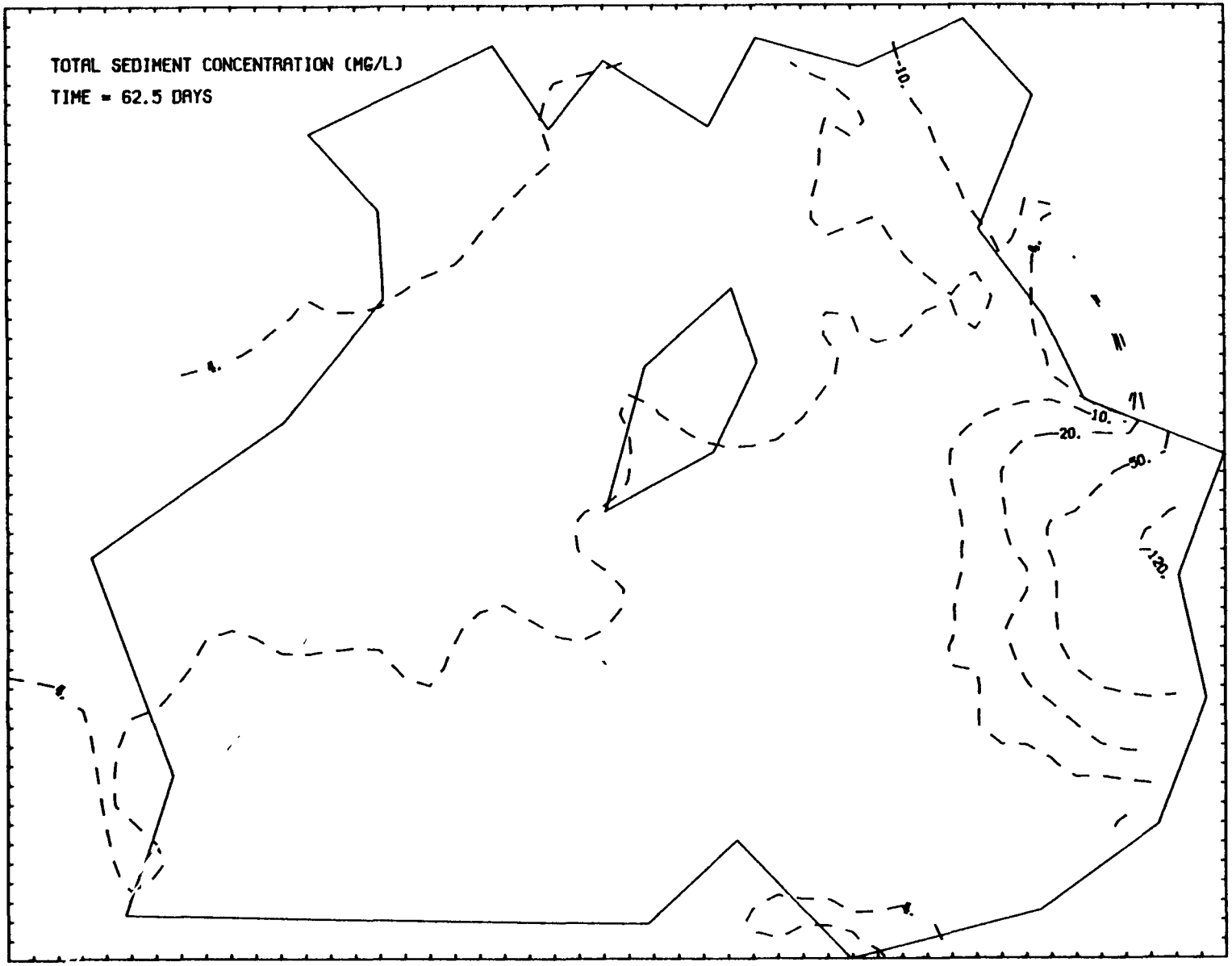

FIGURE 4.36. Computed Total Suspended Sediment Concentrations AFter 62.5 Days

Dissolved ^{137}Cs distributions measured in July 1973 and July 1974 are shown in Figures 4.37 and 4.38 (Hetherington 1976; Pentreath et al. 1983). The higher dissolved ^{137}Cs concentrations measured in July 1974 as compared to those of July 1973 resulted because larger amounts of ^{137}Cs were released from the Windscale plant in 1974, as indicated in Figure 4.1. The difference in dissolved ^{137}Cs concentrations between those two measurements was plotted in Figure 4.39. This difference in ^{137}Cs concentration is due to six to seven months high release of ^{137}Cs in 1974 from January to July. Note that dissolved

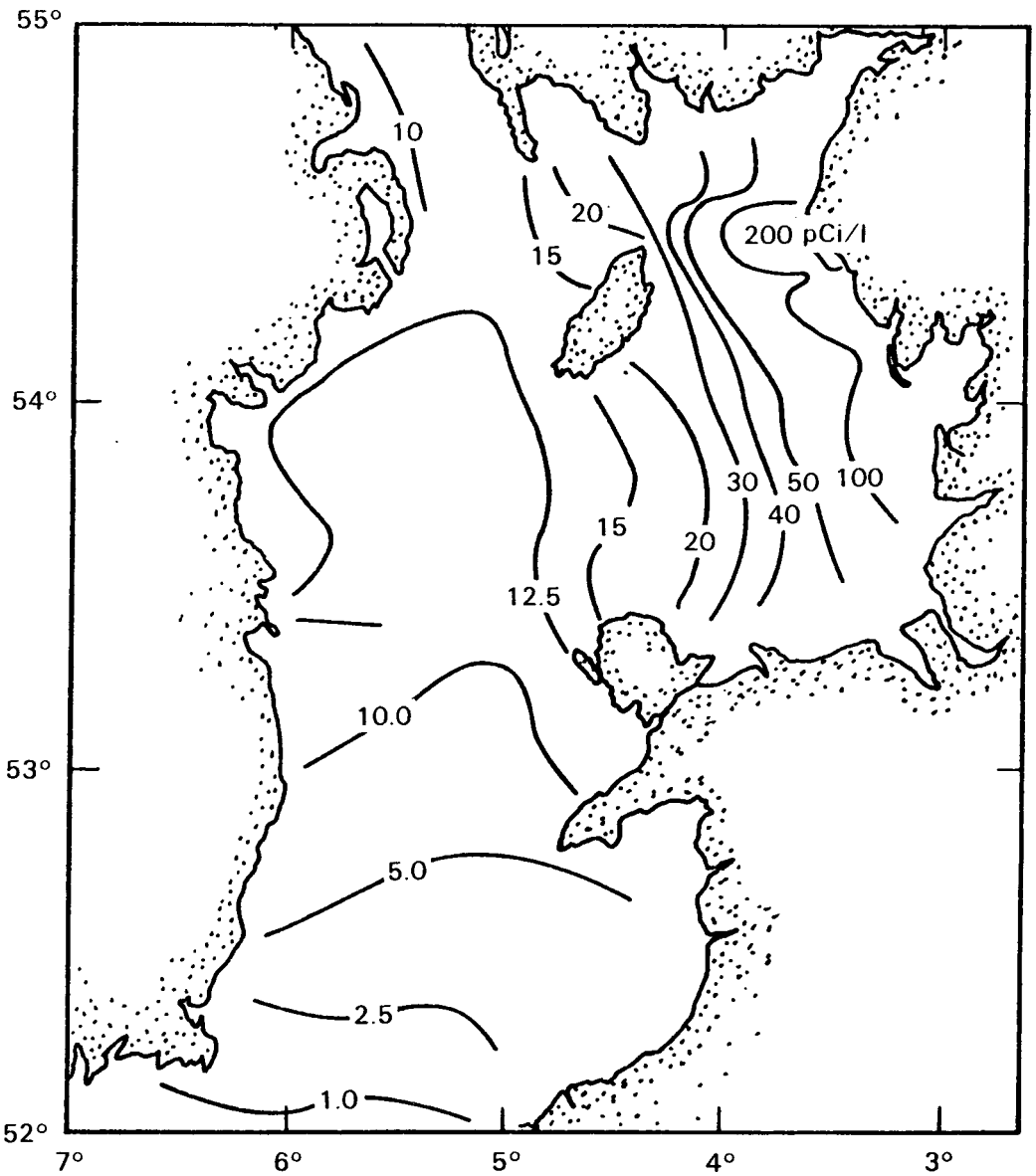

FIGURE 4.37. Dissolved ^{137}Cs Concentrations Measured in July 1973 (Hetherington 1976; Pentreath et al. 1983)

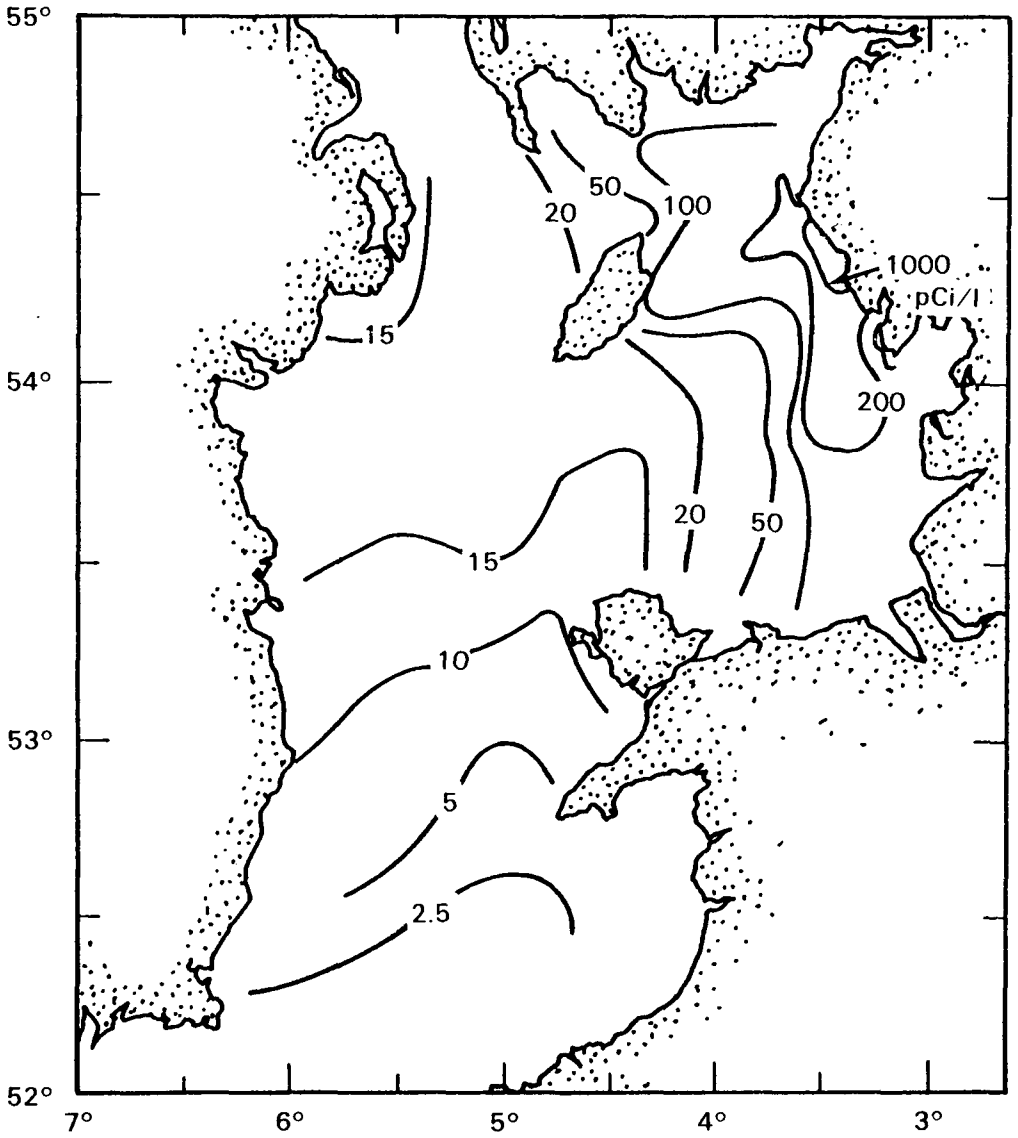

FIGURE 4.38. Dissolved ^{137}Cs Concentrations (measured in July 1974) (Hetherington 1976; Pentreat et al. 1983)

^{137}Cs concentrations measured north of Anglesey were the same or lower for July 1974 as for July 1973. Because our simulation started with no ^{137}Cs concentrations in the Irish Sea, we compare our simulation results with the incremental difference between measured concentrations from 1973 to 1974 as shown in Figure 4.39.

Predicted dissolved ^{137}Cs concentrations after 15.6 days of simulation are shown in Figure 4.40. Predicted concentrations varied from over 50 pCi/ℓ near the release point to below 0.1 pCi/ℓ around the southwest corner of the Irish Sea study area. Dissolved concentrations near the release point were much smaller than measured data indicate. The model discretization near the release

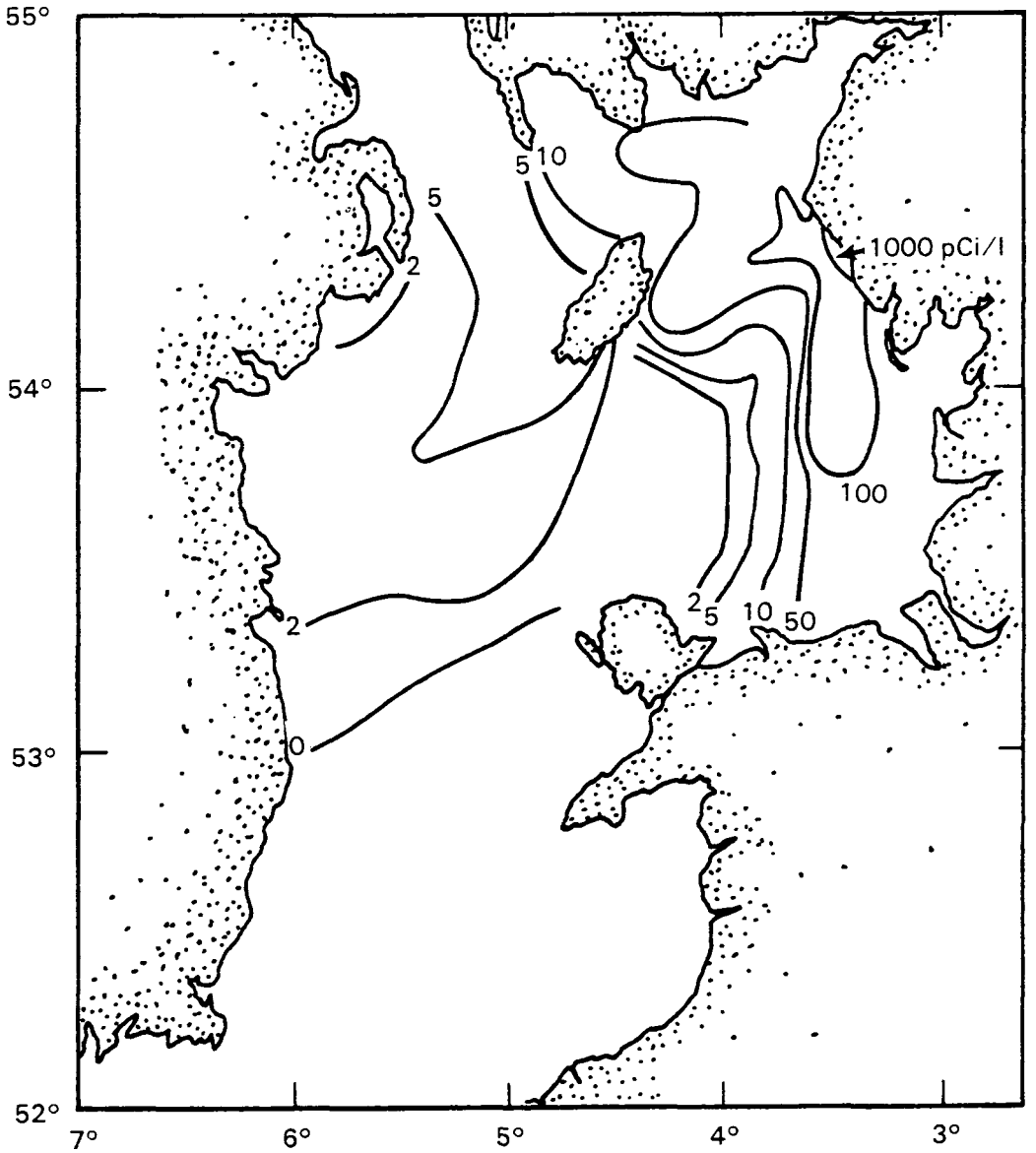

FIGURE 4.39. Difference Between Measured Dissolved ^{137}cs Concentrations in July 1974 and July 1973

point was not fine enough to produce the very sharp peak of computed radionuclide concentration near the source. Because the finite element technique produces solutions to fit an overall solution plane based on available nodes, the rather coarse finite element grid used for this study did not show the very sharp concentration rise near the source. Moreover, some dispersion occurred through the beach boundary, because the grid used was too coarse. The coarse grid did not allow the model to compute ^{137}Cs concentration with no gradient perpendicular to the boundary even though the model formulation was set to impose no flux across the solid boundary. However, the amount of dispersion across the beach boundary was small because we used very small dispersion coefficients. These shortcomings in the solution could very likely be eliminated simply by using a finer finite element grid around the release

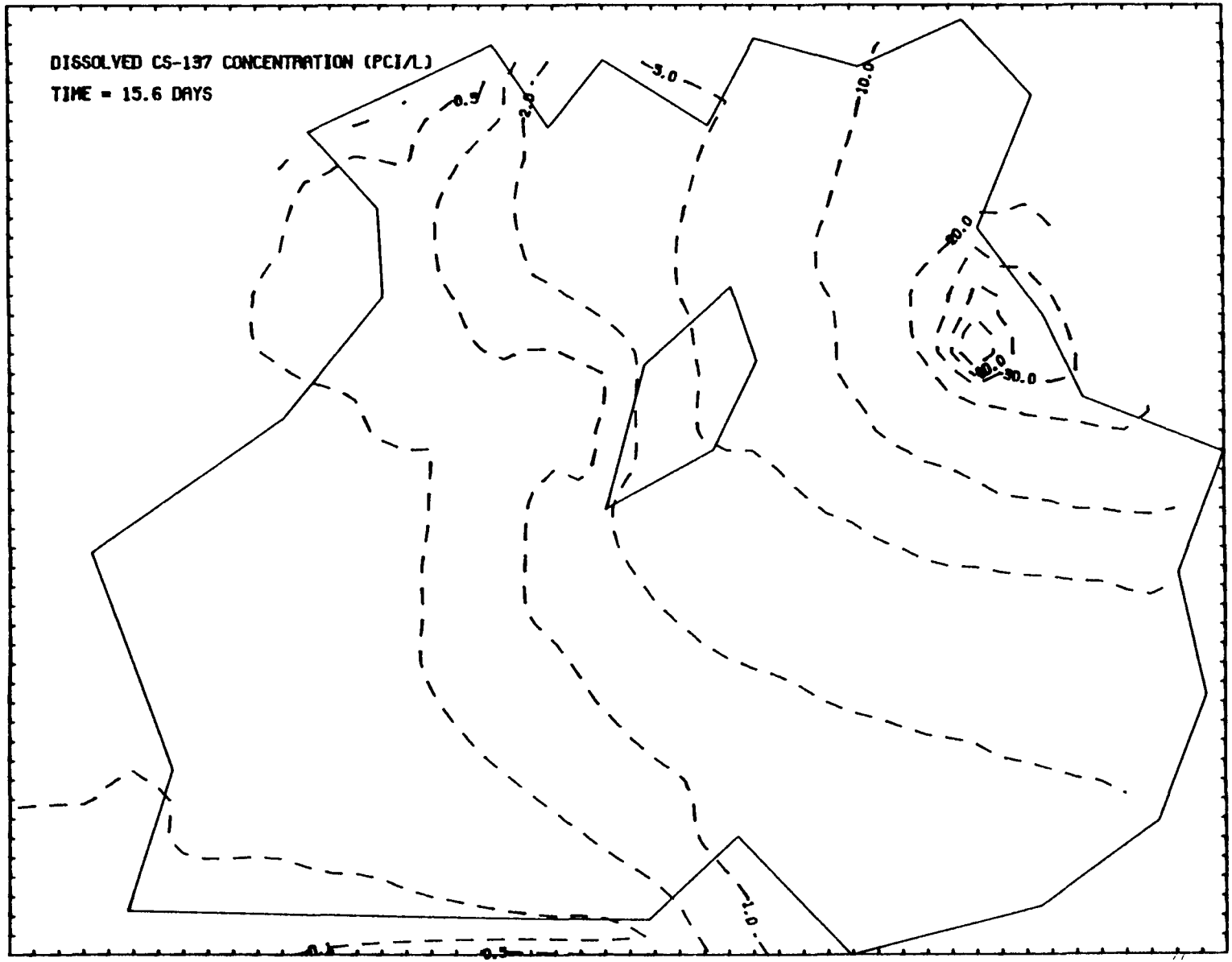

FIGURE 4.40. Computed Dissolved ^{137}Cs Concentrations after 15.6 Days of Simulations

point. However, this modification would increase the computational time. Although some problems arose because we used a coarse grid, the model did generally produce a reasonable pattern of dissolved ^{137}Cs distribution.

Computed ^{137}Cs sorbed by suspended sand, silt, and clay are shown in Figure 4.41, 4.42, and 4.43, respectively, reflecting the computed dissolved ^{137}Cs distribution pattern. As expected from the values of distribution coefficients of ^{137}Cs with sand, silt, and clay, ^{137}Cs sorbed by suspended clay had the highest concentration, approximately 20 times higher than corresponding ^{137}Cs associated with suspended sand. Figure 4.44 shows ^{137}Cs sorbed by weighted-average suspended sediment in pCi/g, while Figure 4.45 indicates the total ^{137}Cs attached to suspended sediments in pCi/ℓ. The total ^{137}Cs concentrations in water column (the sum of dissolved and suspended-sediment-sorbed ^{137}Cs) are shown in Figure 4.46.

Computed distributions of ^{137}Cs associated with bed sediment in the top 10-cm bed layer are shown in Figures 4.47, 4.48, and 4.49. Note that Figure 4.51 also shows ^{137}Cs concentration contours obtained by reducing the measured ^{137}Cs (shown in Figure 4.39) by factor of 3.25. Again, ^{137}Cs attached to bed clay has the highest concentration; (up to 4.2 pCi/g near the release point. However, these values are lower than actual ^{137}Cs concentrations because the course grid caused the model to underestimate dissolved ^{137}Cs concentrations near the release point. The ^{137}Cs attached to bed sand has the lowest concentrations with maximum concentrations of 0.21 pCi/g near the release point. Cesium-137 sorbed by weighted-average bed sediment is shown in Figure 4.50, ranging from 1.3 pCi/g near the release point to 0.0002 pCi/g near the southwest corner of the study area. The model also predicted that west of the Isle of Man ^{137}Cs concentrations were relatively high associated with the weighted-average bed sediment. This reveals that high ^{137}Cs concentrations appear in the areas west of the Isle of Man and near the release point, which contained bed sediment with a high clay content.

Computed ^{137}Cs distributions at 62.5 days are shown in Figure 4.51 through Figure 4.64. Computed concentrations of dissolved ^{137}Cs at 62.5 days, shown in Figure 4.51, vary from over 50 pCi/ℓ near the source to approximately 0.1 pCi/ℓ near the north and south opening of the Irish Sea. Note that dissolved ^{137}Cs concentrations near the northern entrance of the Irish Sea were larger than those near the southern entrance of the Irish Sea, because the net tidal flow moves from south to north. Since the measured dissolved ^{137}Cs concentrations plotted in Figure 4.39 were a phenomena produced by six to seven months of high ^{137}Cs discharges in 1974, the computed dissolved ^{137}Cs concentrations should be approximately 3 to 3.5 times smaller than those in Figure 4.39. Again, the general pattern of dissolved ^{137}Cs concentration that was predicted is reasonably close to estimated values based on measured concentrations, except around two areas. One exception is near the release point due to the use of coarse grids in this modeling as discussed earlier. The second area is the southeastern portion of the study area. In order to produce the distribution estimated from the measured dissolved ^{137}Cs distributions shown in this region, there must be a large-scale southerly residual flow from Windscale toward Liverpool Bay. However, the CAFE results indicate that our predicted velocity distributions, which matched reasonably well with measured velocity data, did

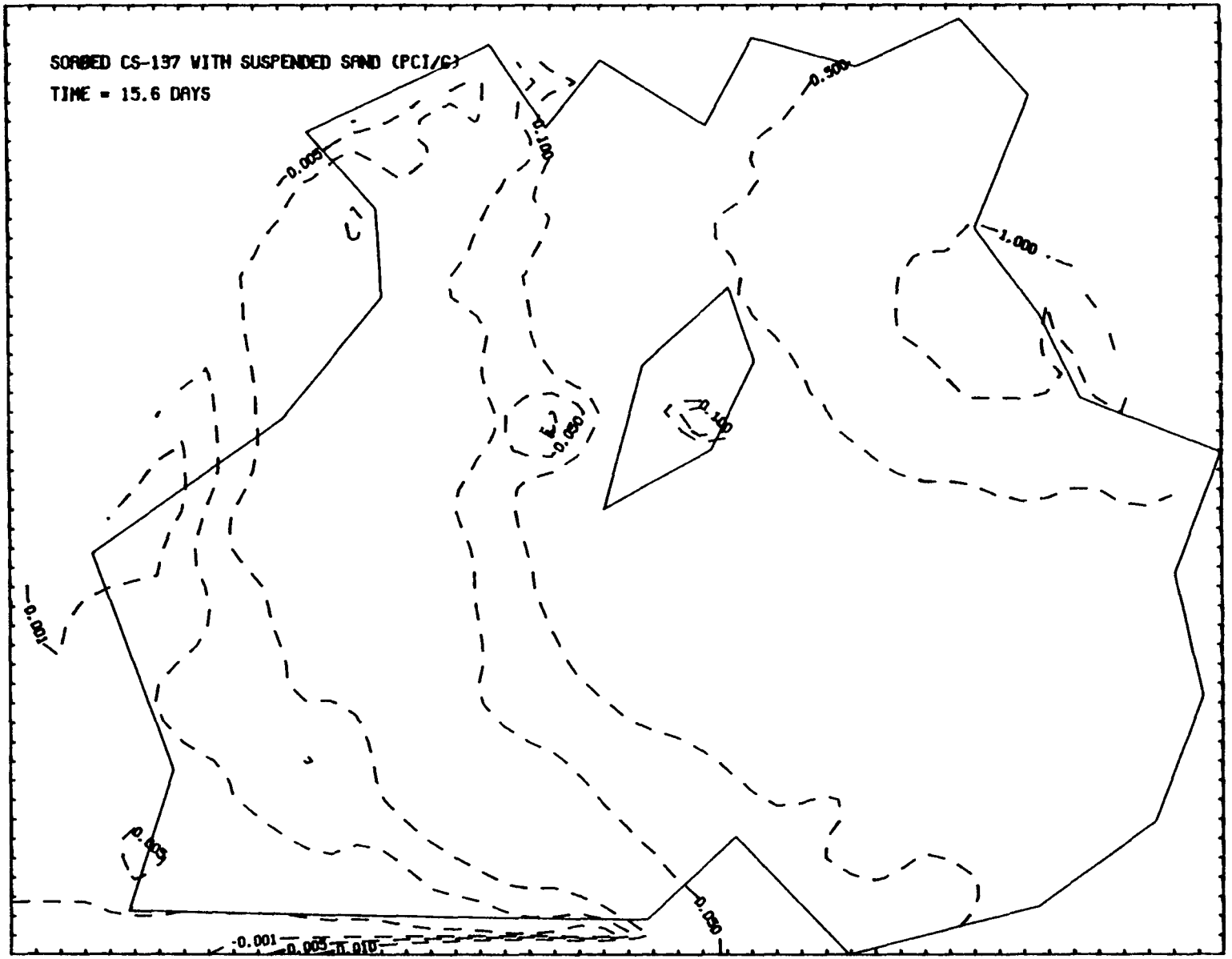

FIGURE 4.41. Computed Concentrations ^{137}Cs Sorbed by Suspended Sand After 15.6 Days of Simulation

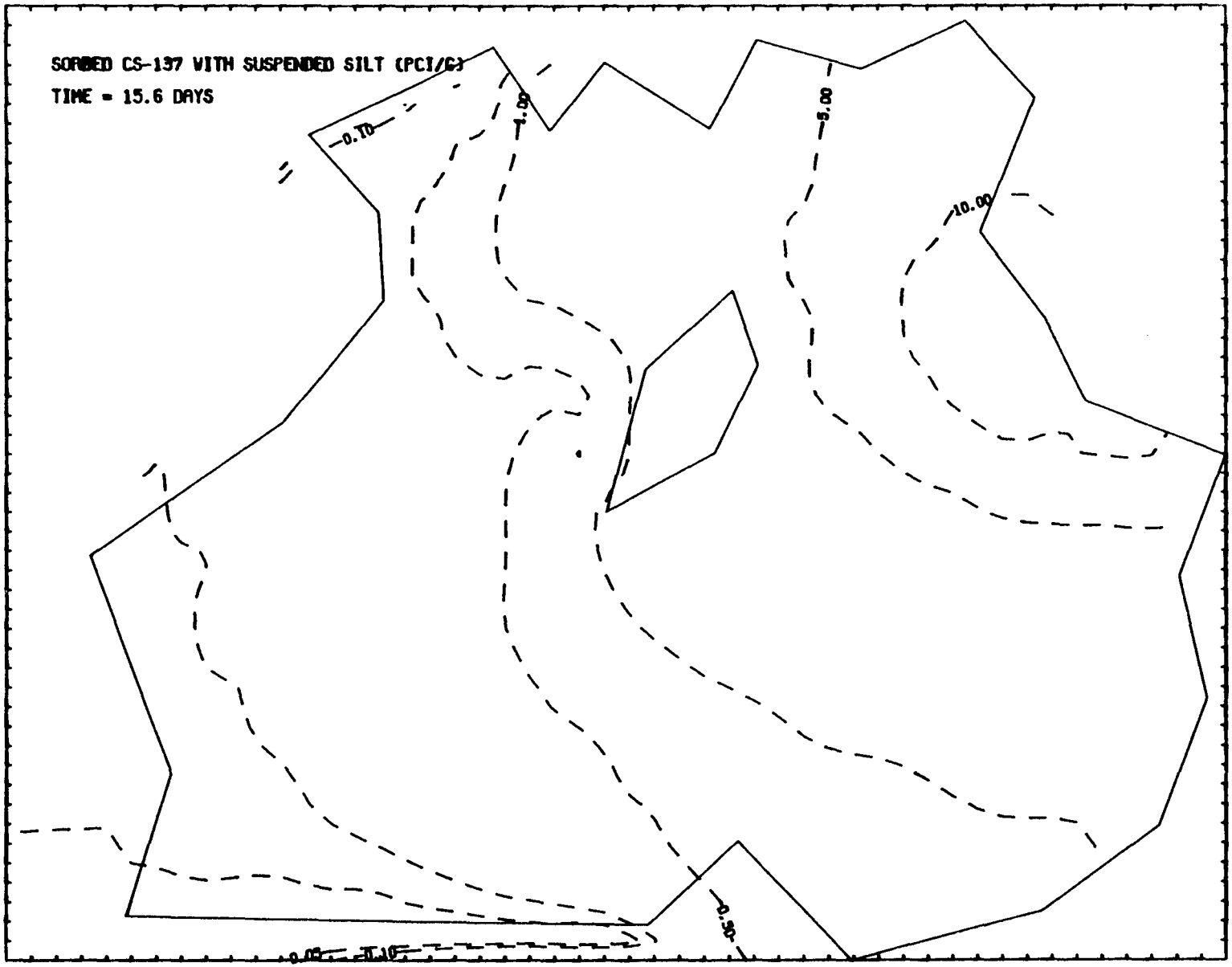

FIGURE 4.42. Computed Concentrations ^{137}Cs Sorbed by Suspended Silt After 15.6 Days of Simulation

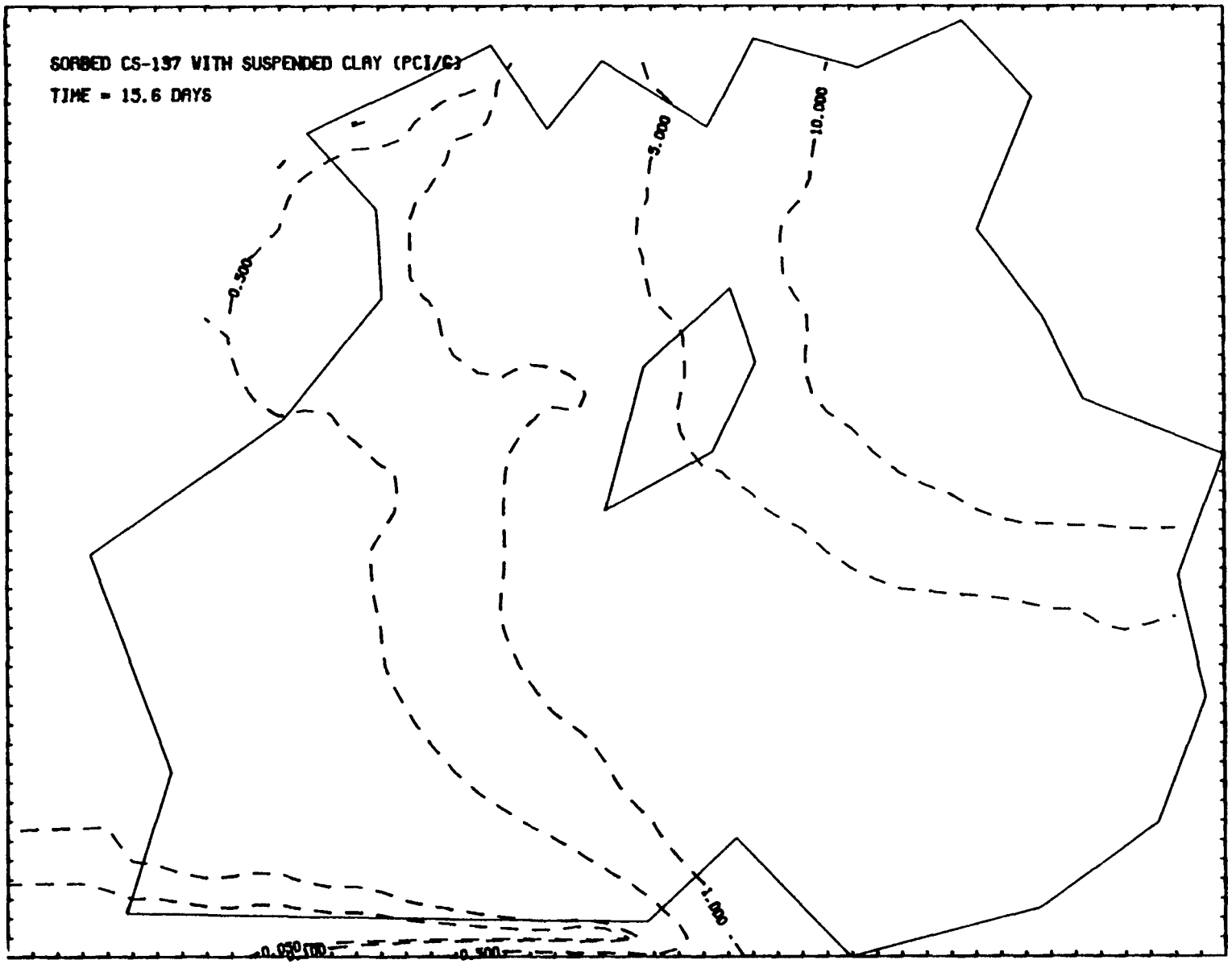

FIGURE 4.43. Computed Concentrations ^{137}Cs Sorbed by Suspended Clay After 15.6 Days of Simulation

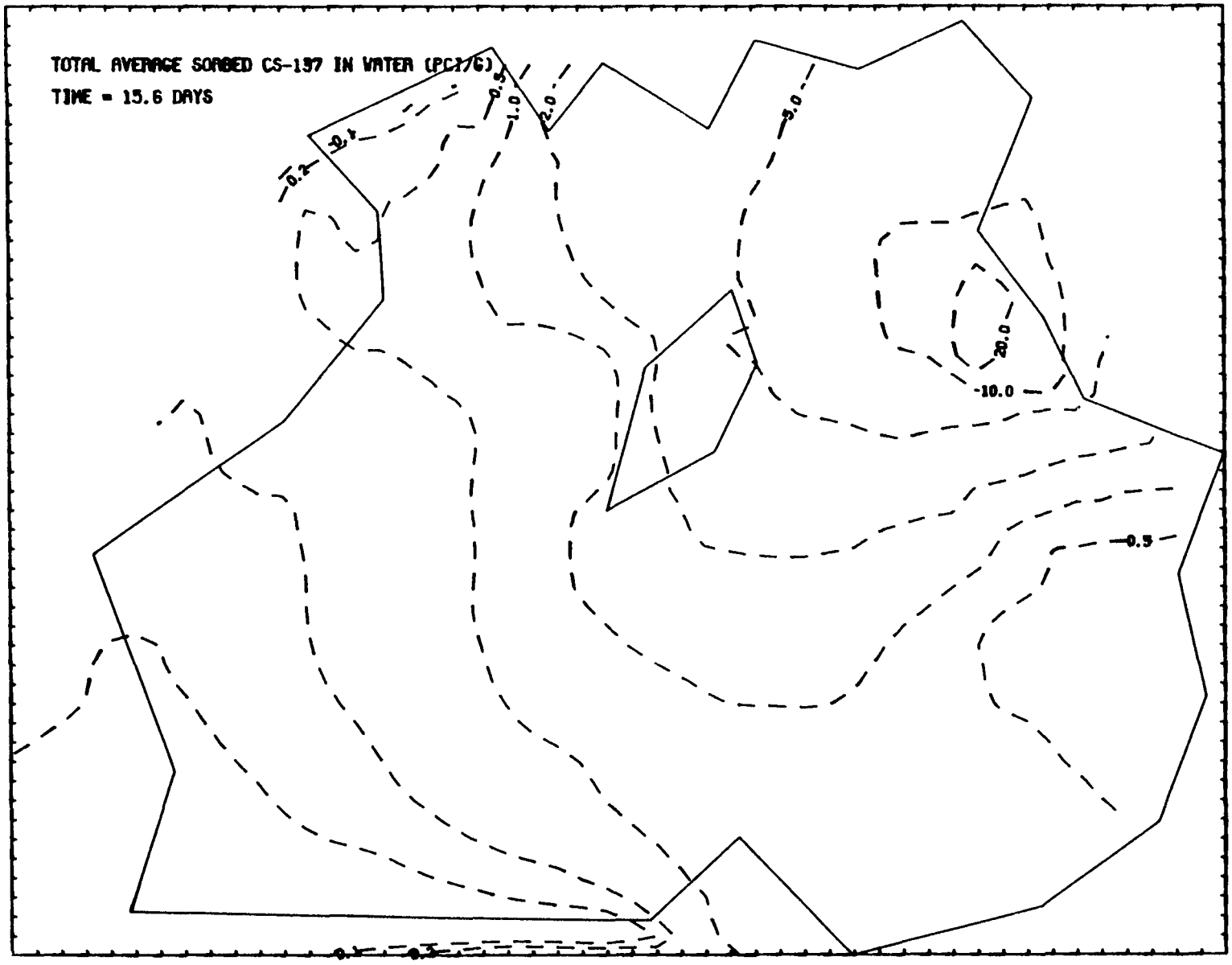

FIGURE 4.44. Computed Concentrations of ^{137}Cs Sorbed by Weighted Average Suspended Sediment After 15.6 Days of Simulation in pCi/g

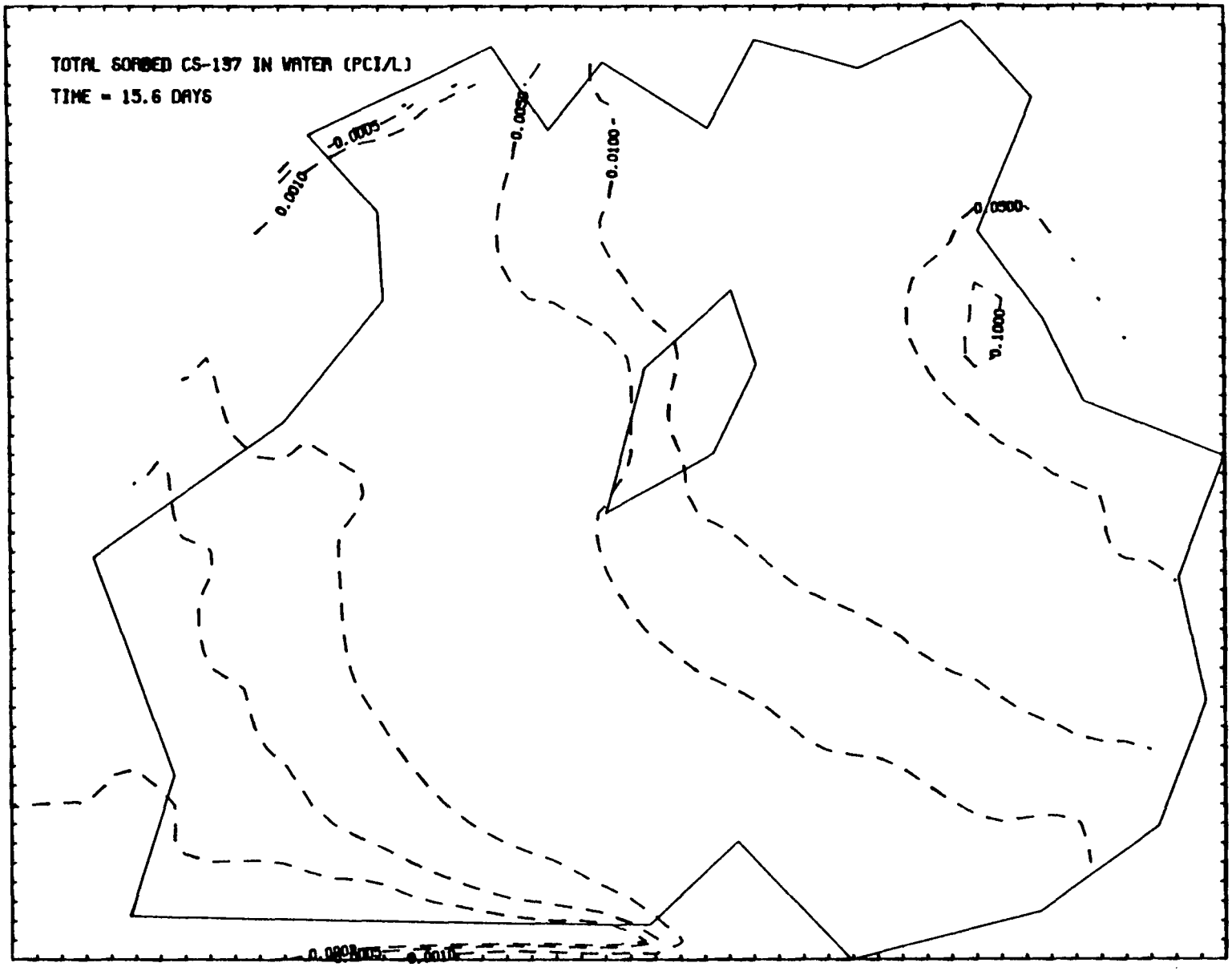

FIGURE 4.45. Computed Concentrations of Total ^{137}Cs Sorbed by All Suspended Sediment After 15.6 Days of Simulation in pCi/ℓ

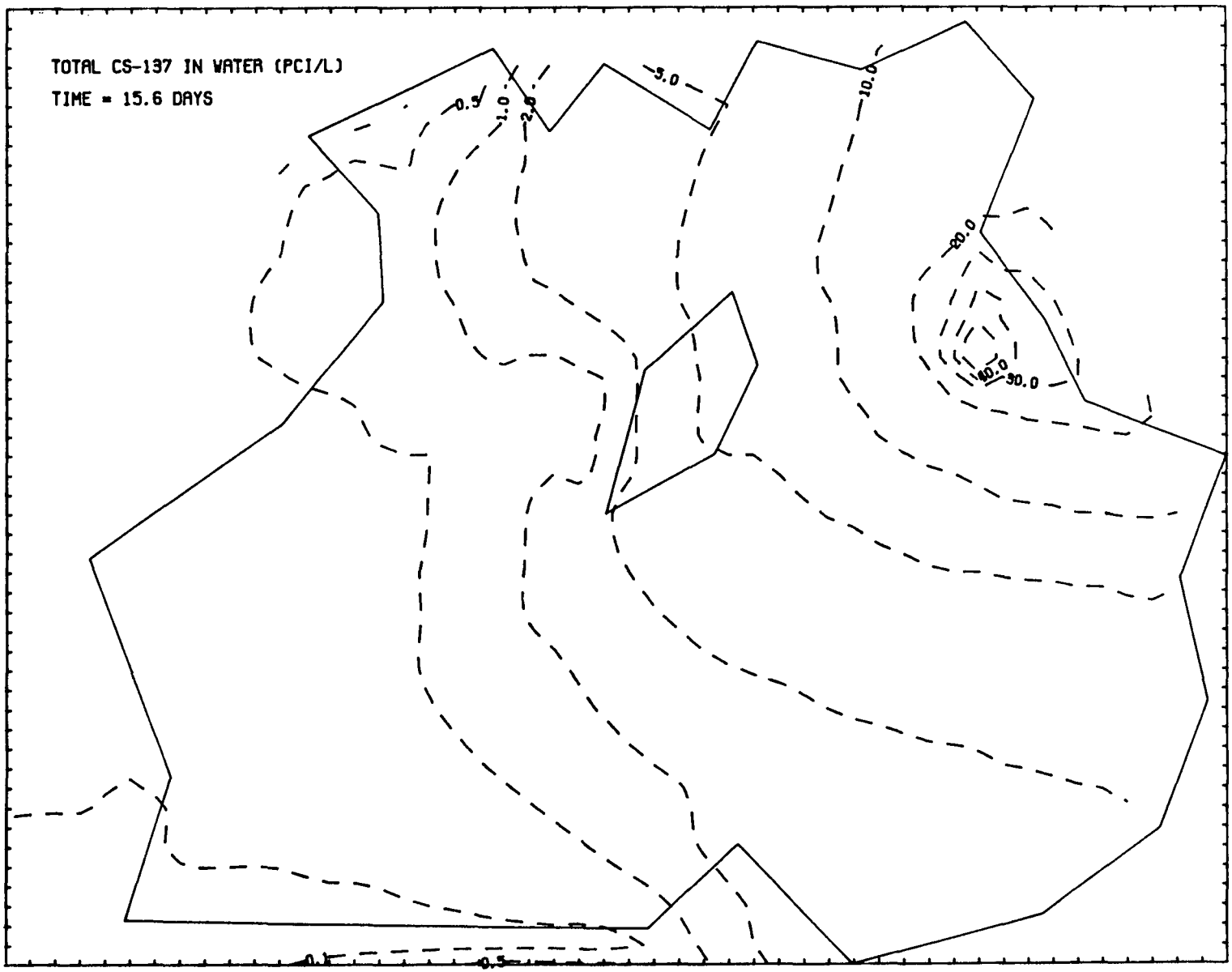

FIGURE 4.46. Computed Concentration of Total ^{137}Cs After 15.6 Days of Simulation

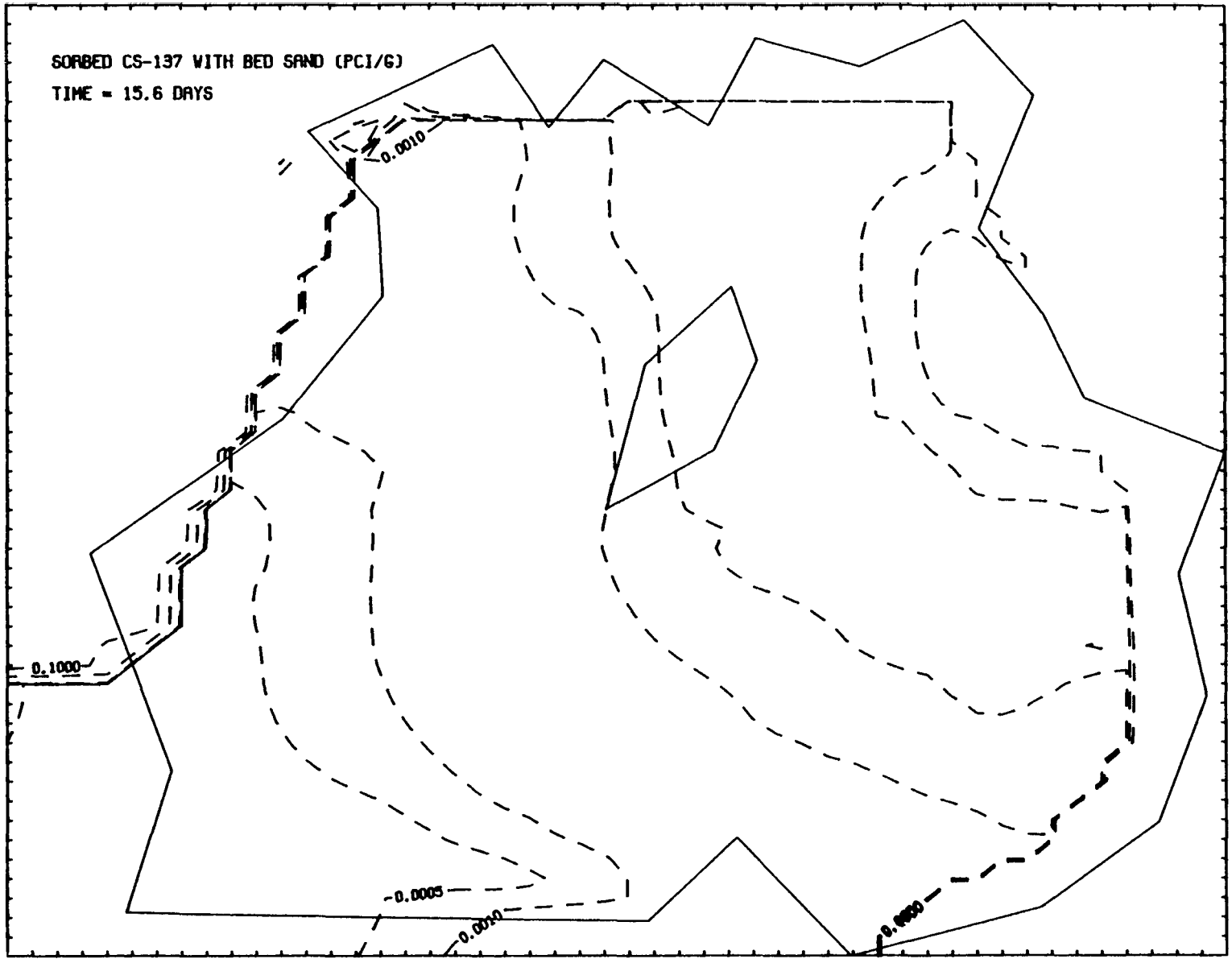

FIGURE 4.47. Computed Concentration of ^{137}Cs Sorbed by Bed Sand in the Top 10-cm Bed Layer After 15.6 Days of Simulation

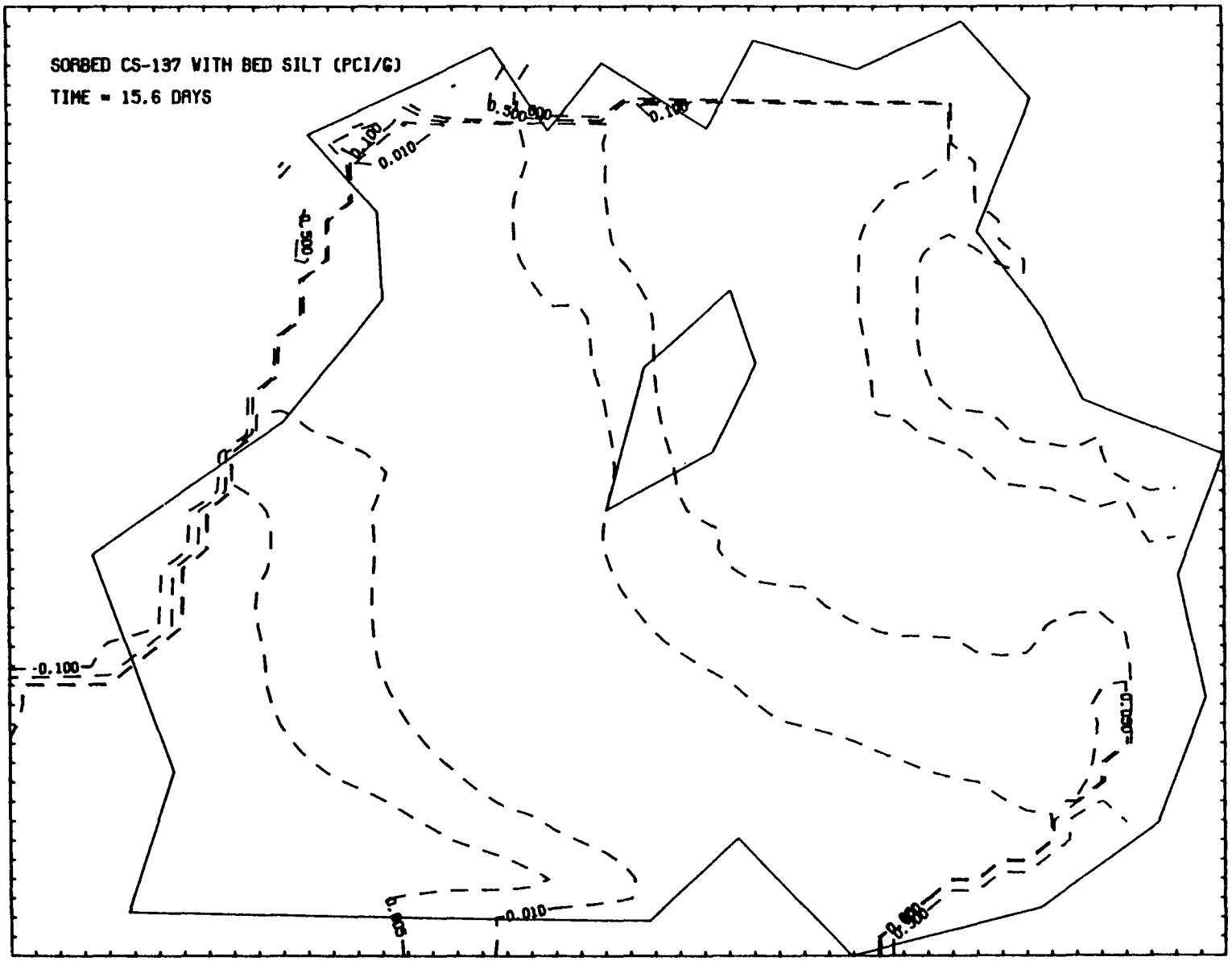

FIGURE 4.48. Computed Concentrations of ^{137}Cs Sorbed by Bed Silt in the Top 10-cm Bed Layer After 15.6 Days of Simulation

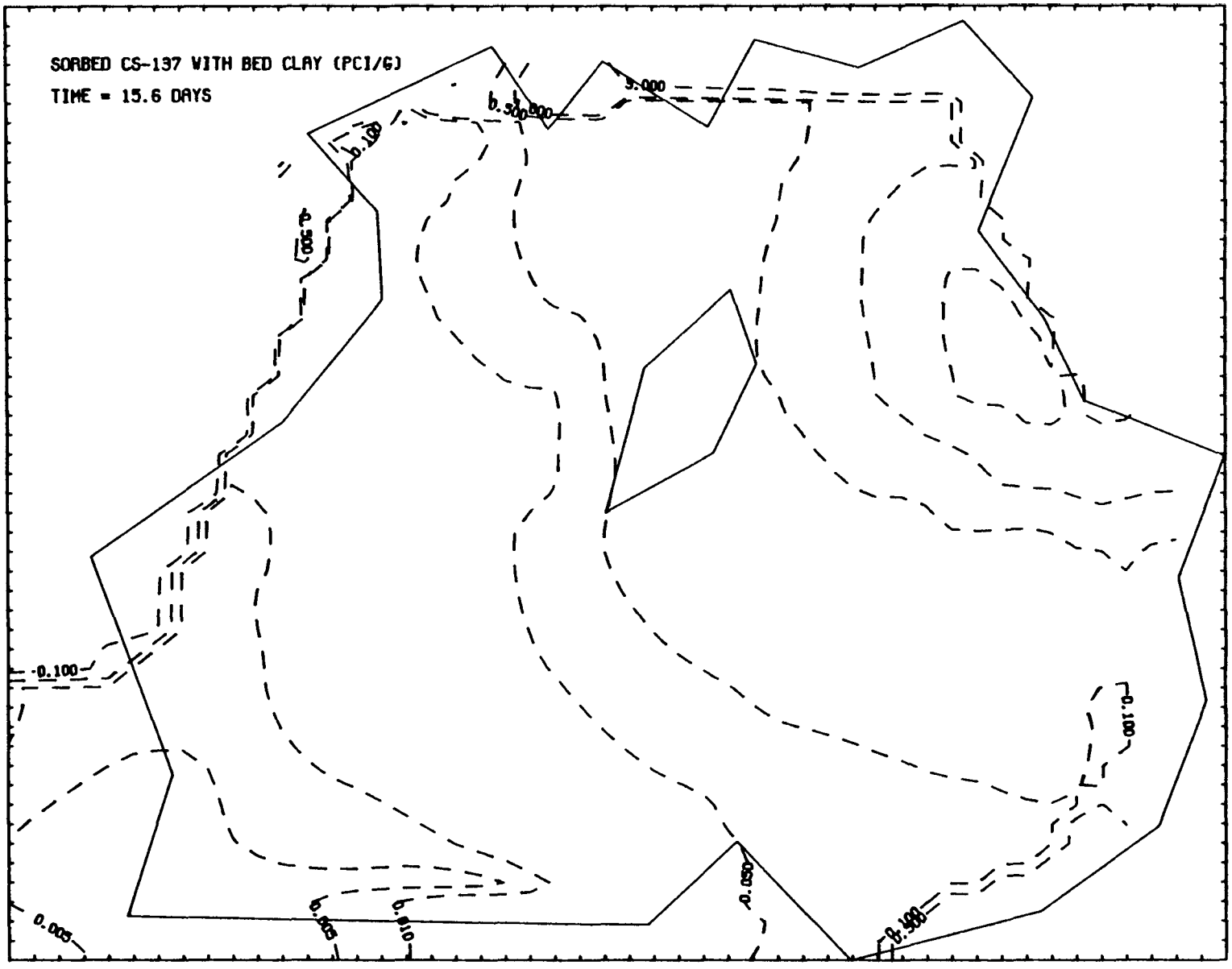

FIGURE 4.49. Computed Concentrations of ^{137}Cs Sorbed by Bed Clay in the Top 10-cm Bed Layer After 15.6 Days of Simulation

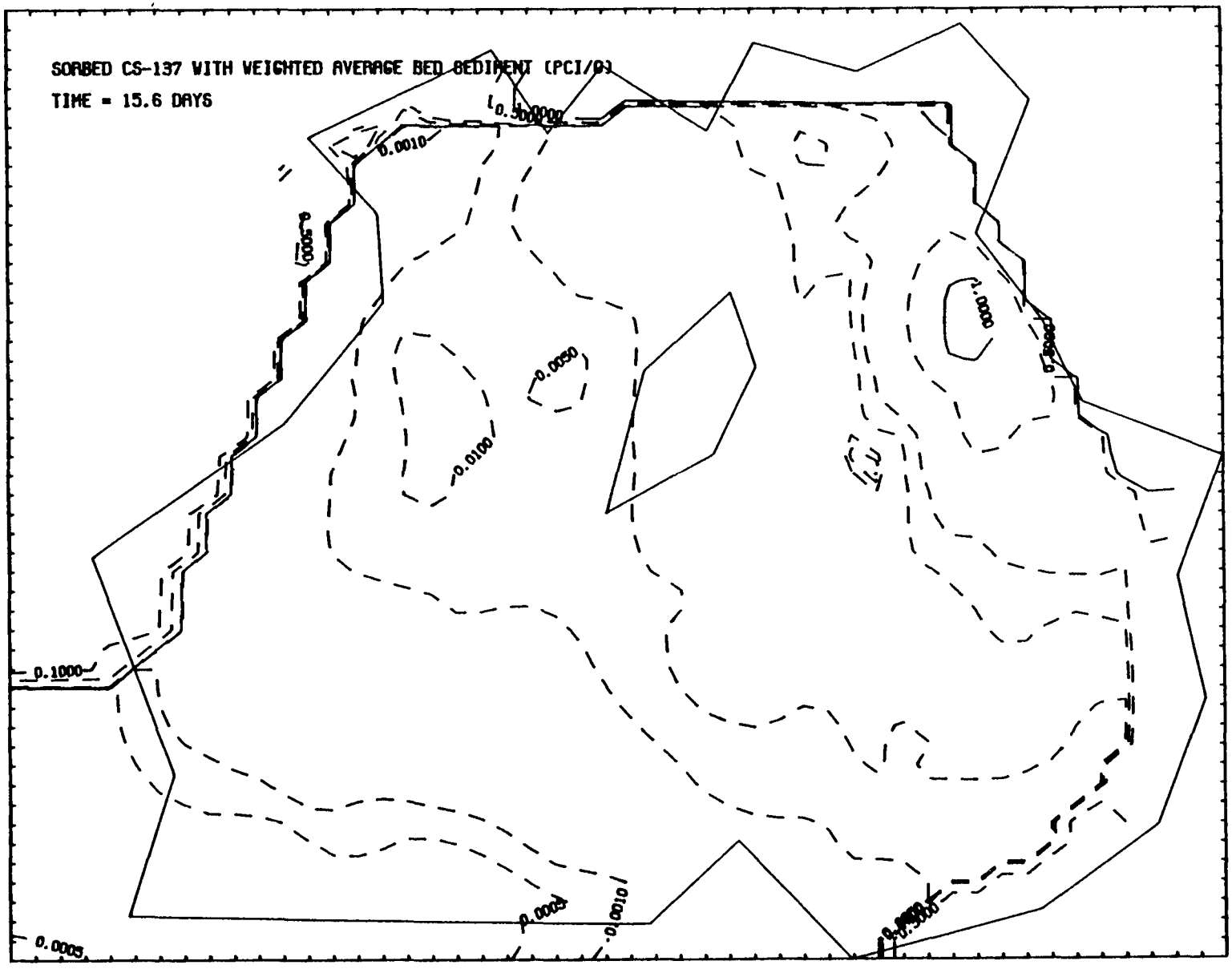

FIGURE 4.50. Computed Concentrations of ^{137}Cs Sorbed by Weighted Average Bed Sediment

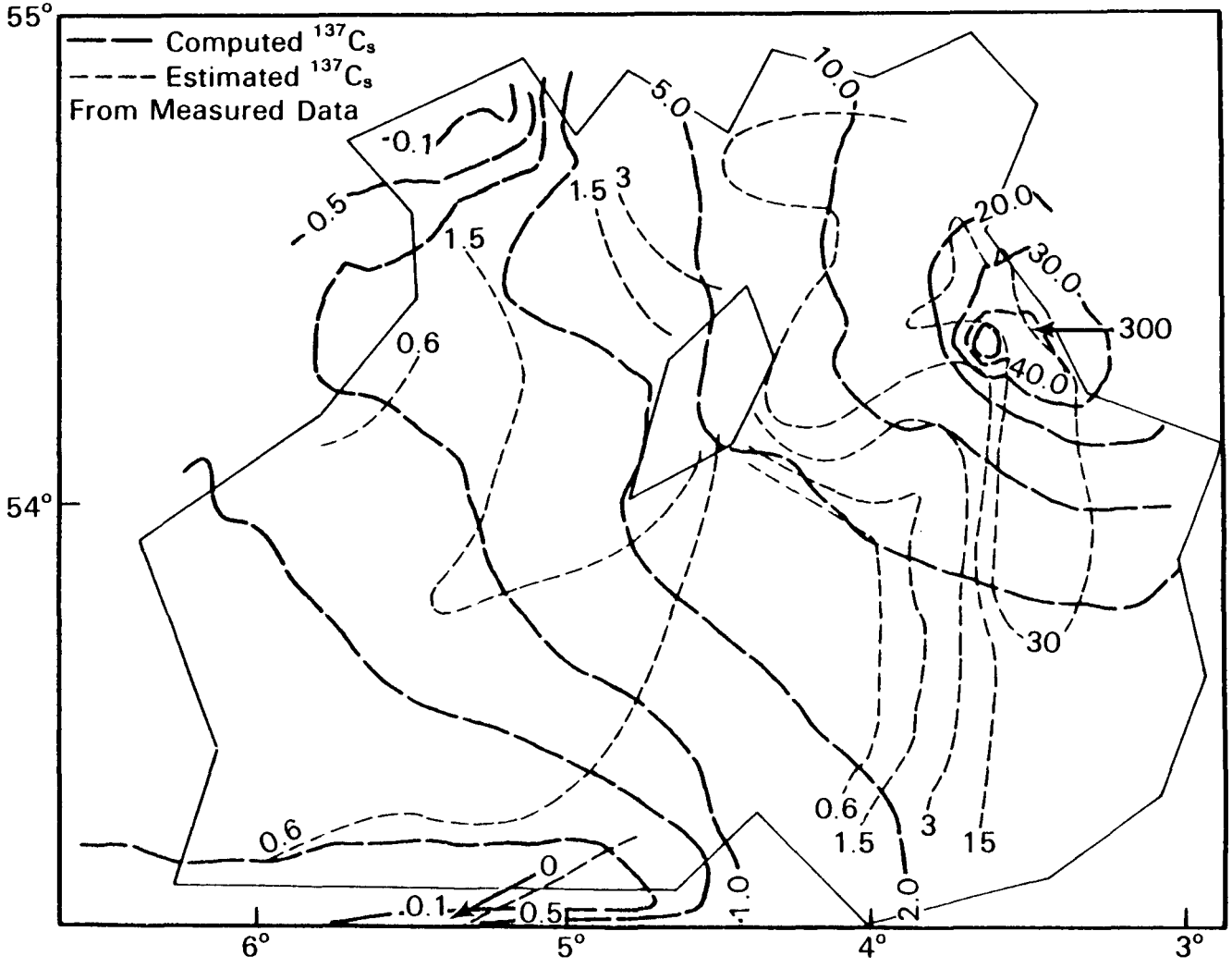

FIGURE 4.51. Computed Dissolved ^{137}Cs Concentrations After 62.5 Days of Simulation Together with Estimated Measured Dissolved ^{137}Cs Concentrations in pCi/ℓ.

not indicate a large-scale southerly residual flow in this area. This possible difference in the velocity fields may be responsible for some of the discrepancy between the simulated and measured ^{137}Cs concentration patterns in this area.

Computed ^{137}Cs concentrations sorbed by suspended sand, silt, clay and weighted-average suspended sediment at 62.5 days are shown in Figures 4.52, 4.53, 4.54, and 4.55. Although these concentration levels were higher, these distributions exhibited similar trends to those at 16.2 days (Figures 4.41, 4.42, 4.43, and 4.44).

Computed concentrations of ^{137}Cs sorbed by all suspended sediment and the total ^{137}Cs (the sum of dissolved and suspended-sediment-sorbed ^{137}Cs) at 62.5 days are also shown in Figures 4.56 and 4.57.

Computed distributions of bed sediment size fractions (bed sand, silt, and clay) in the top 10-cm bed layer after 62.5 days of simulation are shown in Figures 4.58, 4.59, and 4.60, revealing relatively large amounts of fine sediment along Windscale to Liverpool Bay and west of the Isle of Man. These computed sediment distribution patterns differed only slightly from the initial condition of the bed sediment distribution (Figure 4.26).

Computed ^{137}Cs distributions sorbed by bed sand, silt, clay and weighted sediment in the top 10-cm bed layer after 62.5 days of simulation are shown in Figures 4.61, 4.62, 4.63 and 4.64. The highest ^{137}Cs concentration was associated with bed clay near the release point that had a concentration of 16 pCi/g. The predicted ^{137}Cs concentrations sorbed by weighted-averaged bed sediment ranged from approximately 5 pCi/g near the release point to 0.003 pCi/g near the southwestern corner of the study area. Although the ^{137}Cs showed the highest concentrations near the source, relatively higher ^{137}Cs concentrations also correlated well with higher contents of clay in bed sediment. Since Heatherington (1976) reported that the water in the study area flushed with a half period of approximately one year, the very low values of ^{137}Cs concentrations near the southwestern corner may result because the contaminated effluent might not have fully reached that area within the 62.5 days.

At the end of 62.5 days, approximately 82%, 0.002%, and 18% of the total ^{137}Cs remaining in the study area were dissolved, suspended-sediment-sorbed, and bed-sediment-sorbed radionuclides, respectively. Because we selected rather high values for the radionuclide transfer rate from the water to the bed sediment, we predicted somewhat higher fractions of ^{137}Cs contained in bed sediment. Hetherington (1976) reported that over 80% of the ^{137}Cs released to the Irish Sea remains in the water phase. Thus, our prediction agreed fairly well with Hetherington's estimate considering the lack of important field data and the problems caused by using a coarse grid.

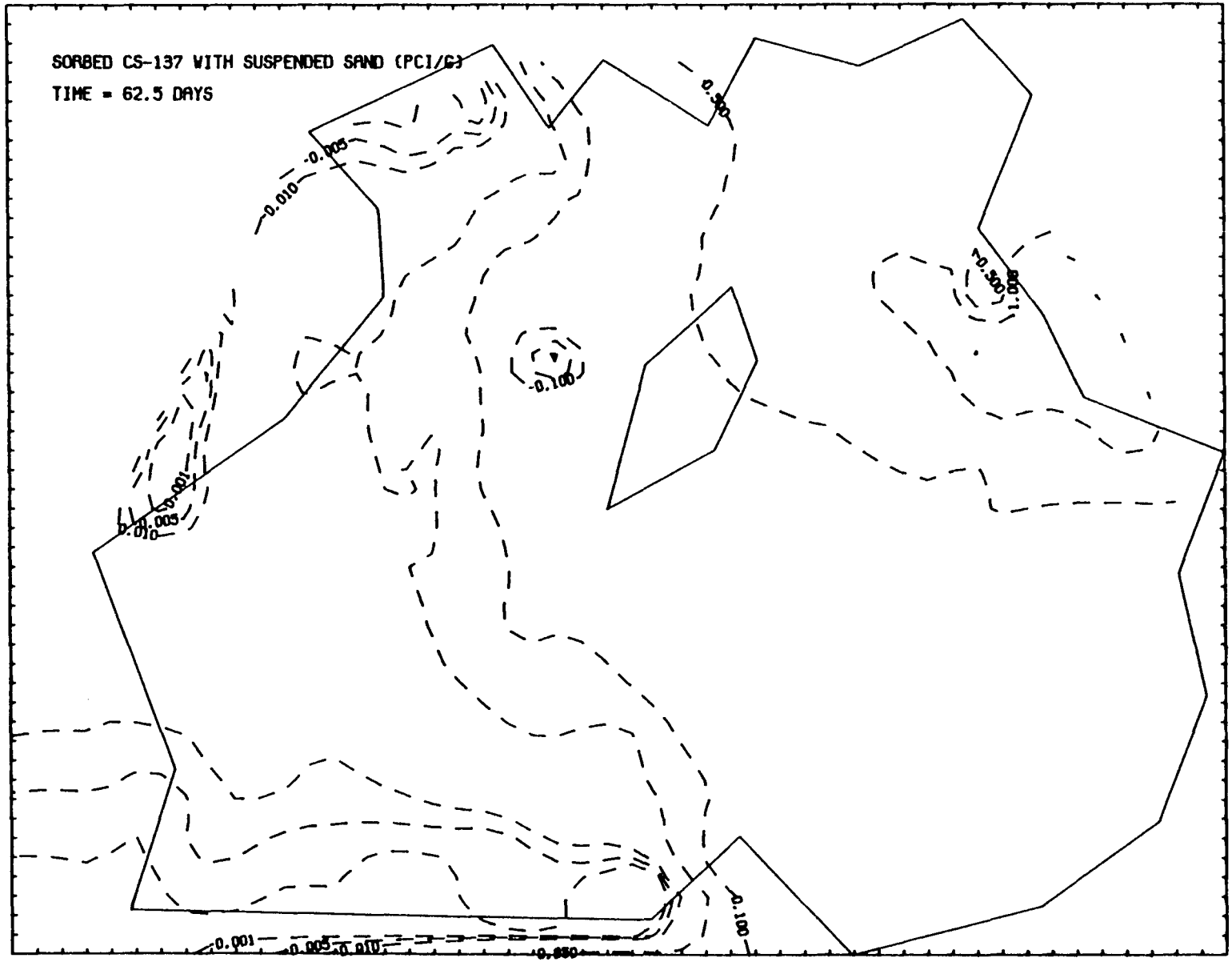

FIGURE 4.52. Computed Concentrations of ^{137}Cs Sorbed by Suspended Sand After 62.5 Days of Simulation

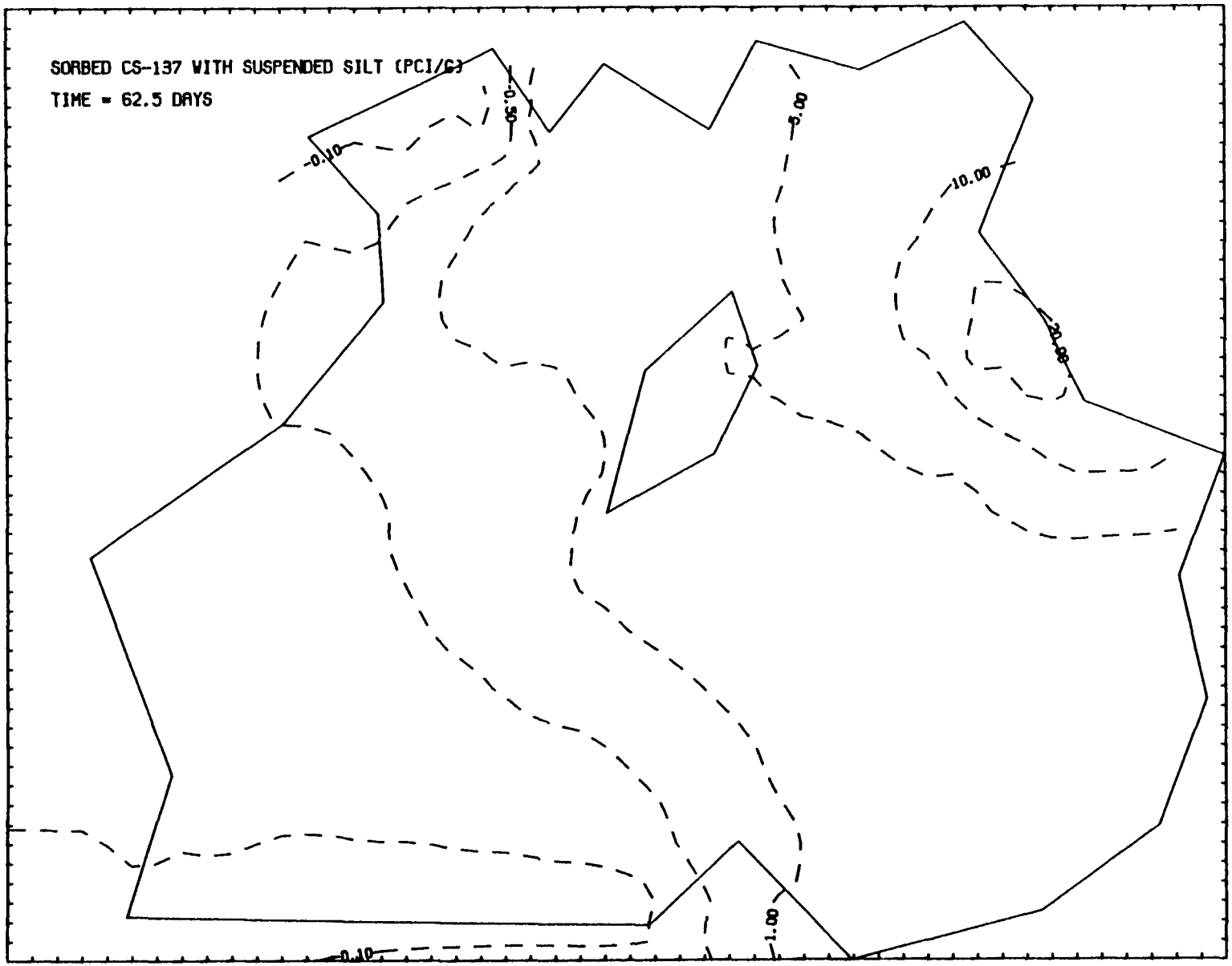

FIGURE 4.53. Computed Concentrations of ^{137}Cs Sorbed by Suspended Silt After 62.5 Days of Simulation

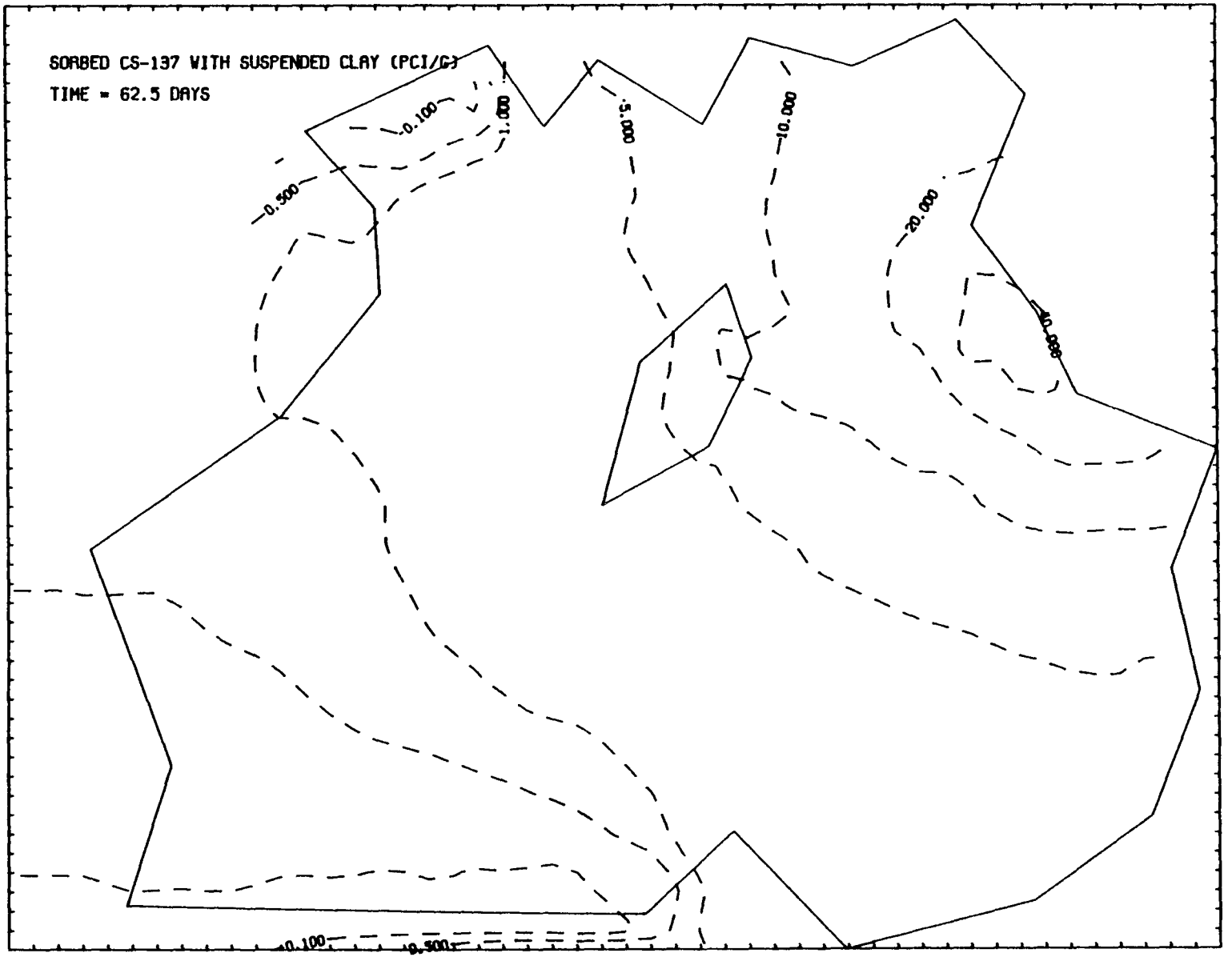

FIGURE 4.54. Computed Concentrations of ^{137}Cs Sorbed by Suspended Clay After 62.5 Days of Simulation

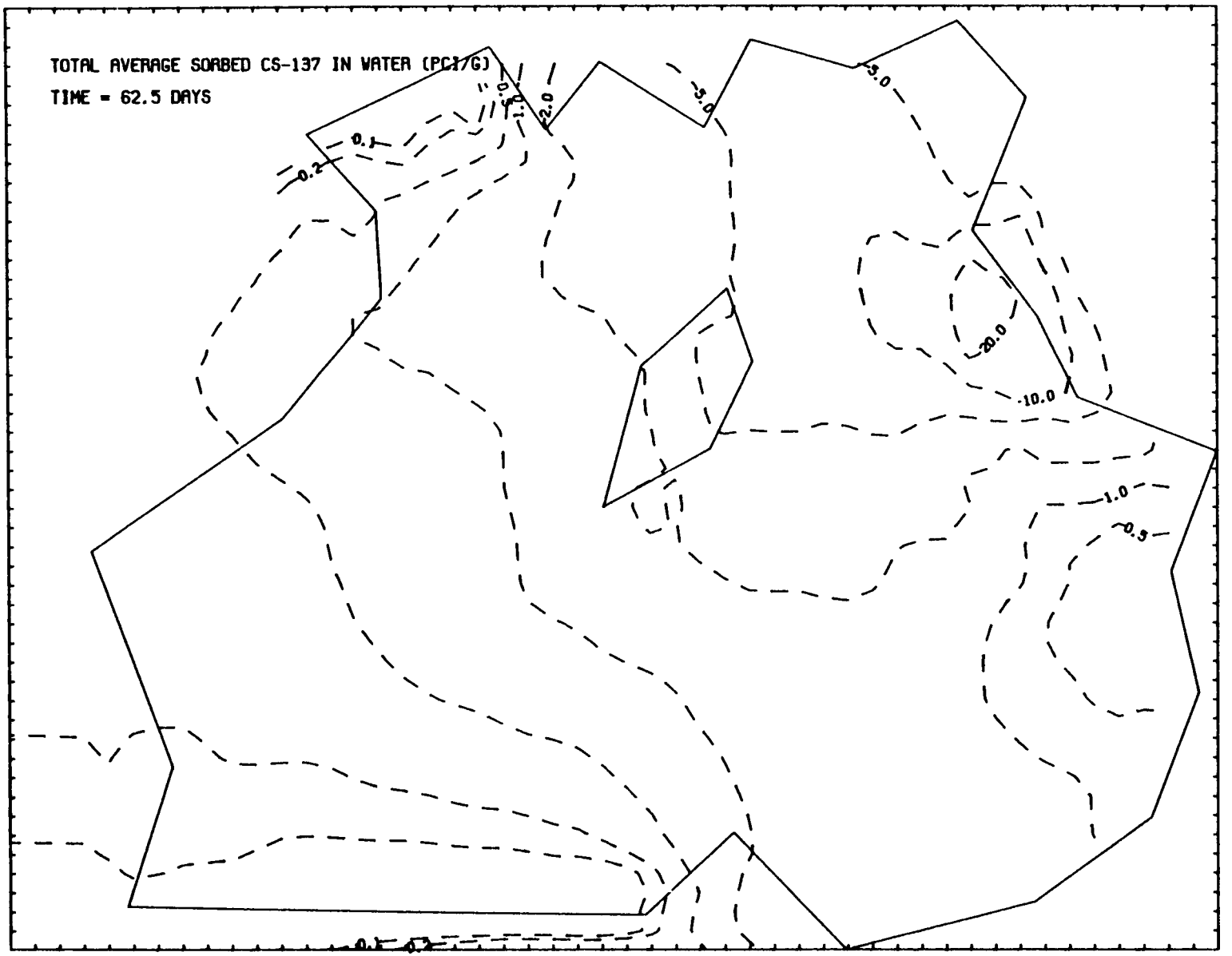

FIGURE 4.55. Computed Concentrations of ^{137}Cs Sorbed by Weighted Average Supsended Sediment After 62.5 Days of Simulation in pCi/g

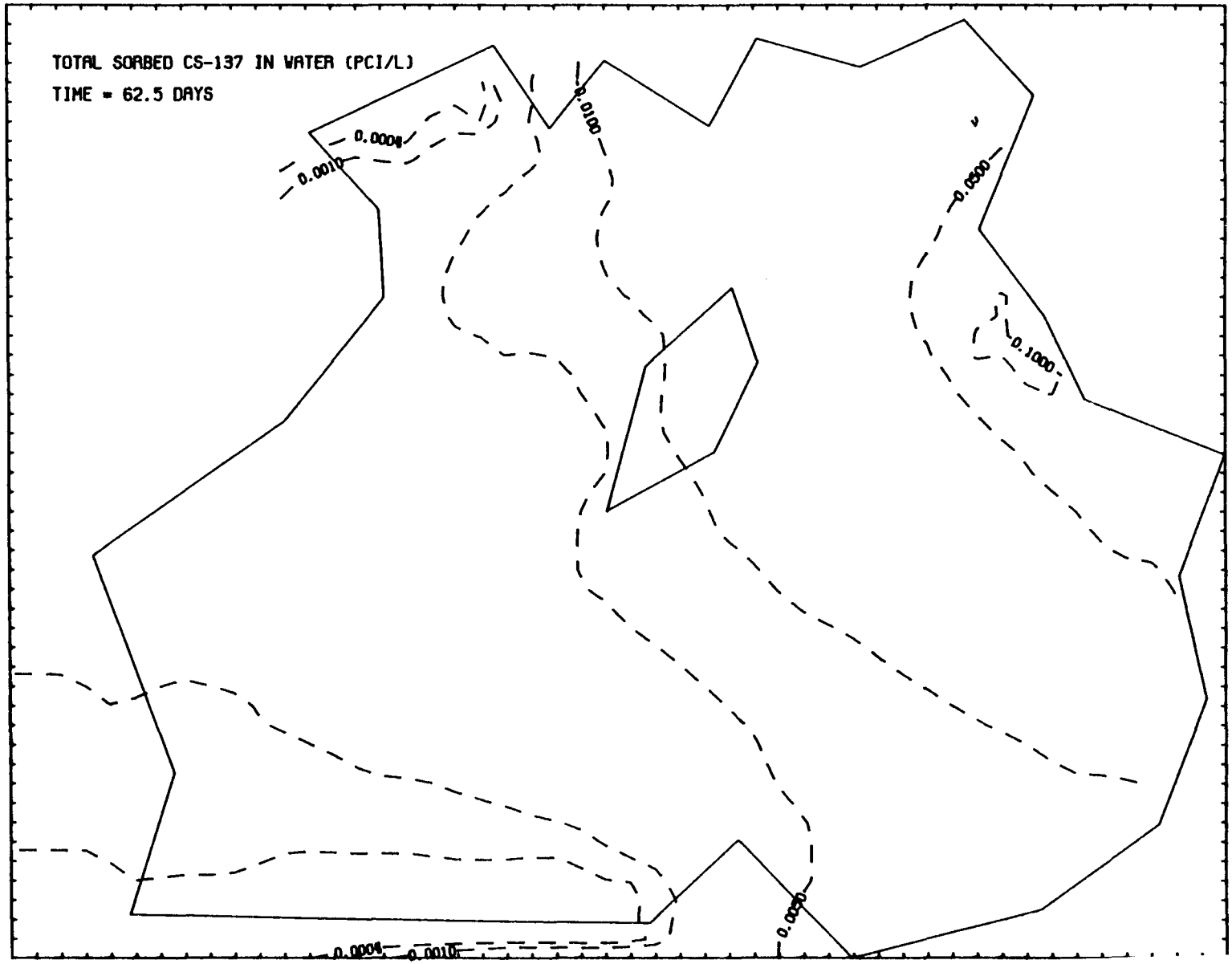

FIGURE 4.56. Computed Concentrations of Total ^{137}Cs Sorbed by All Suspended Sediment After 62.5 Days of Simulation

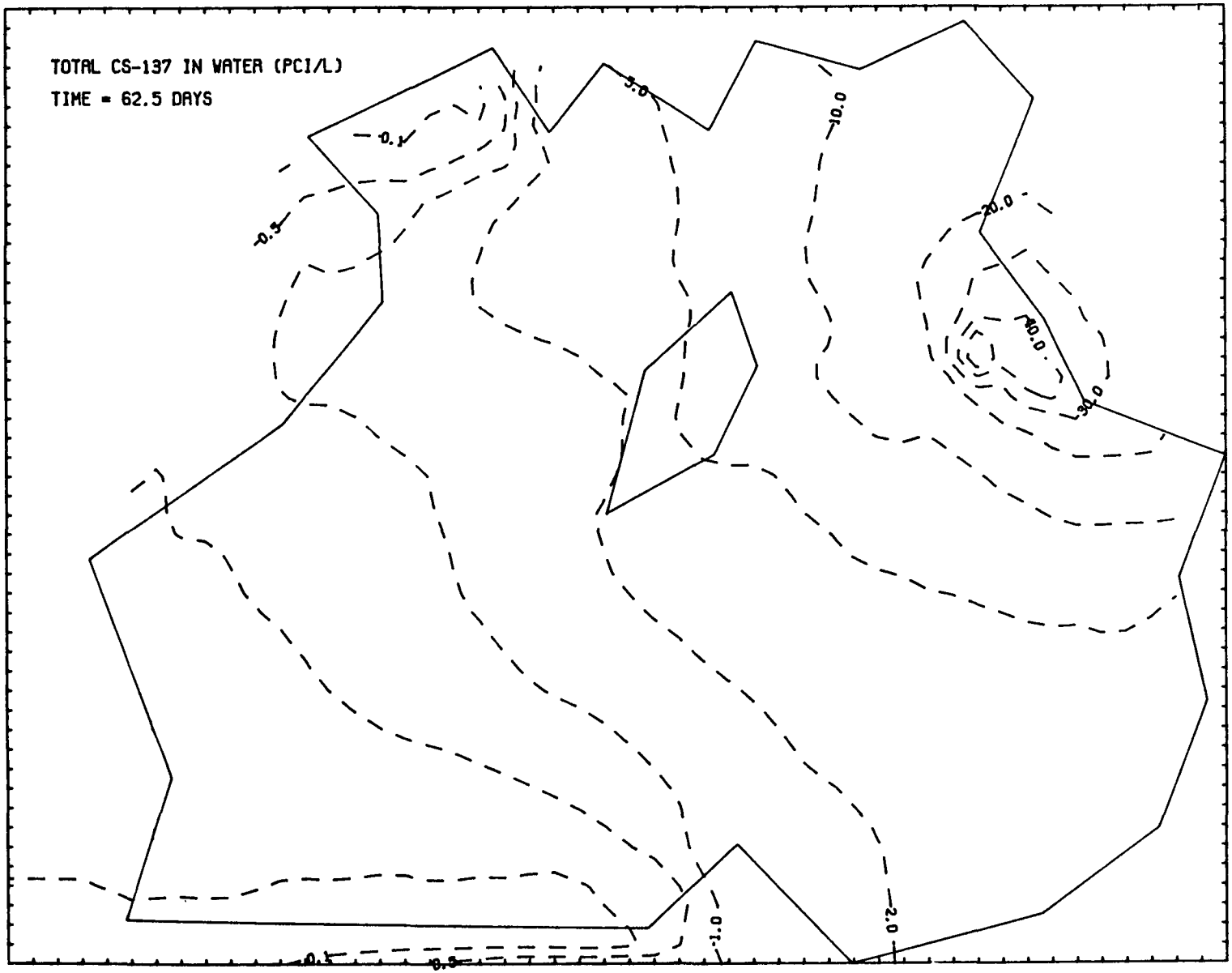

FIGURE 4.57. Computed Concentrations of Total ^{137}Cs After 62.5 Days of Simulation

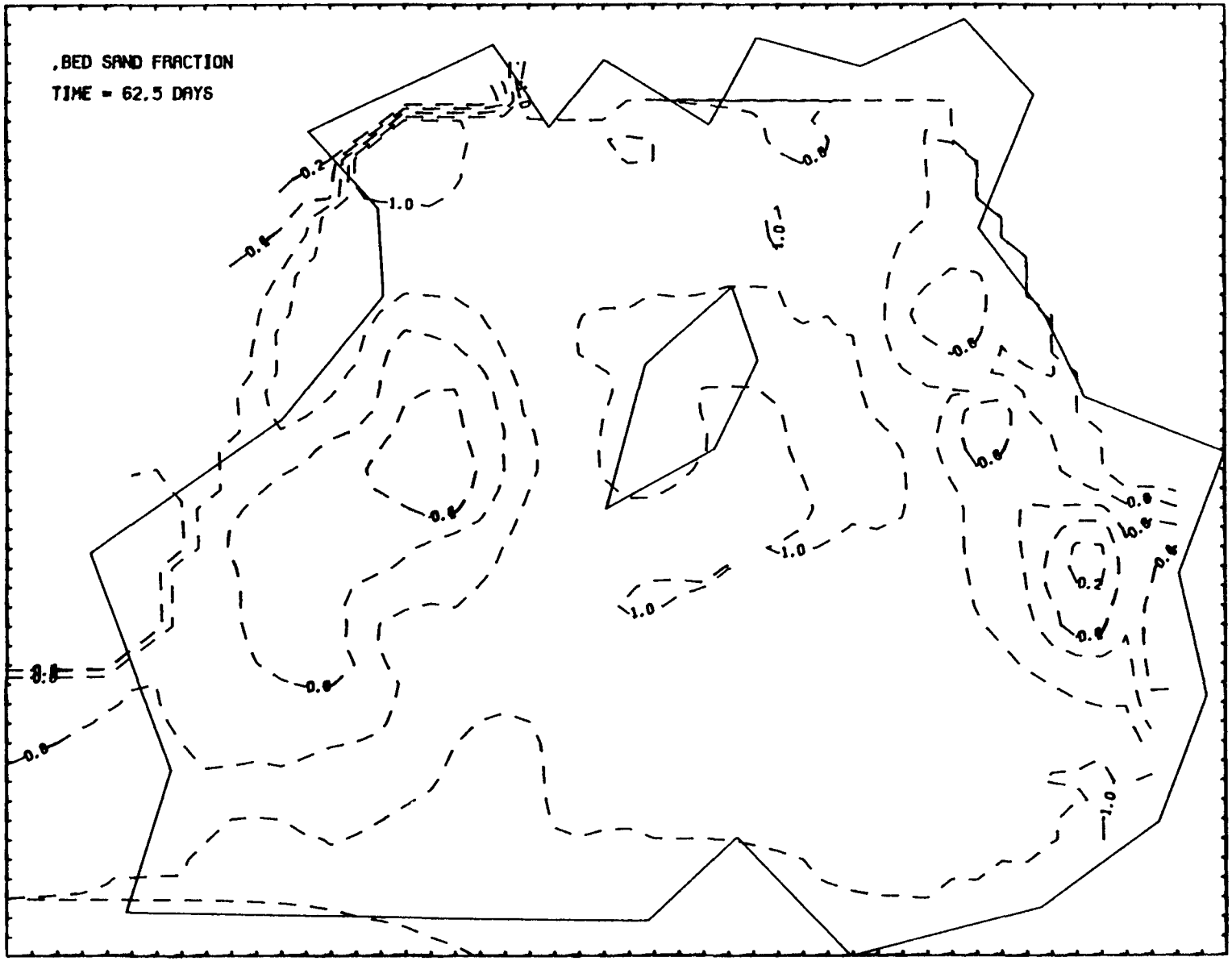

FIGURE 4.58. Computed Distribution of Bed Sand Fraction in the Top 10-cm Bed Layer After 62.5 Days of Simulation

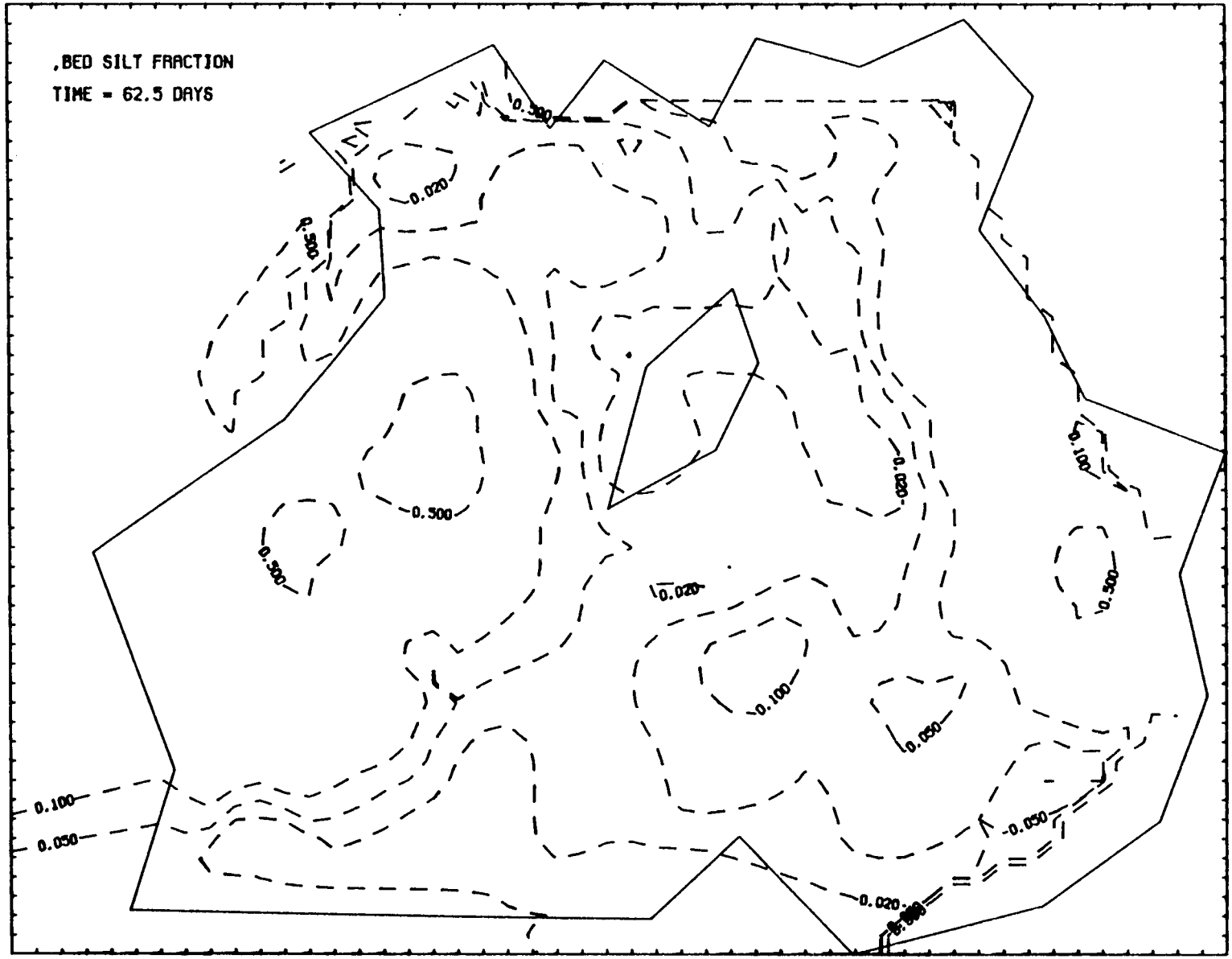

FIGURE 4.59. Computed Distribution of Bed Silt Fraction in the Top 10-cm Bed Layer After 62.5 Days of Simulation

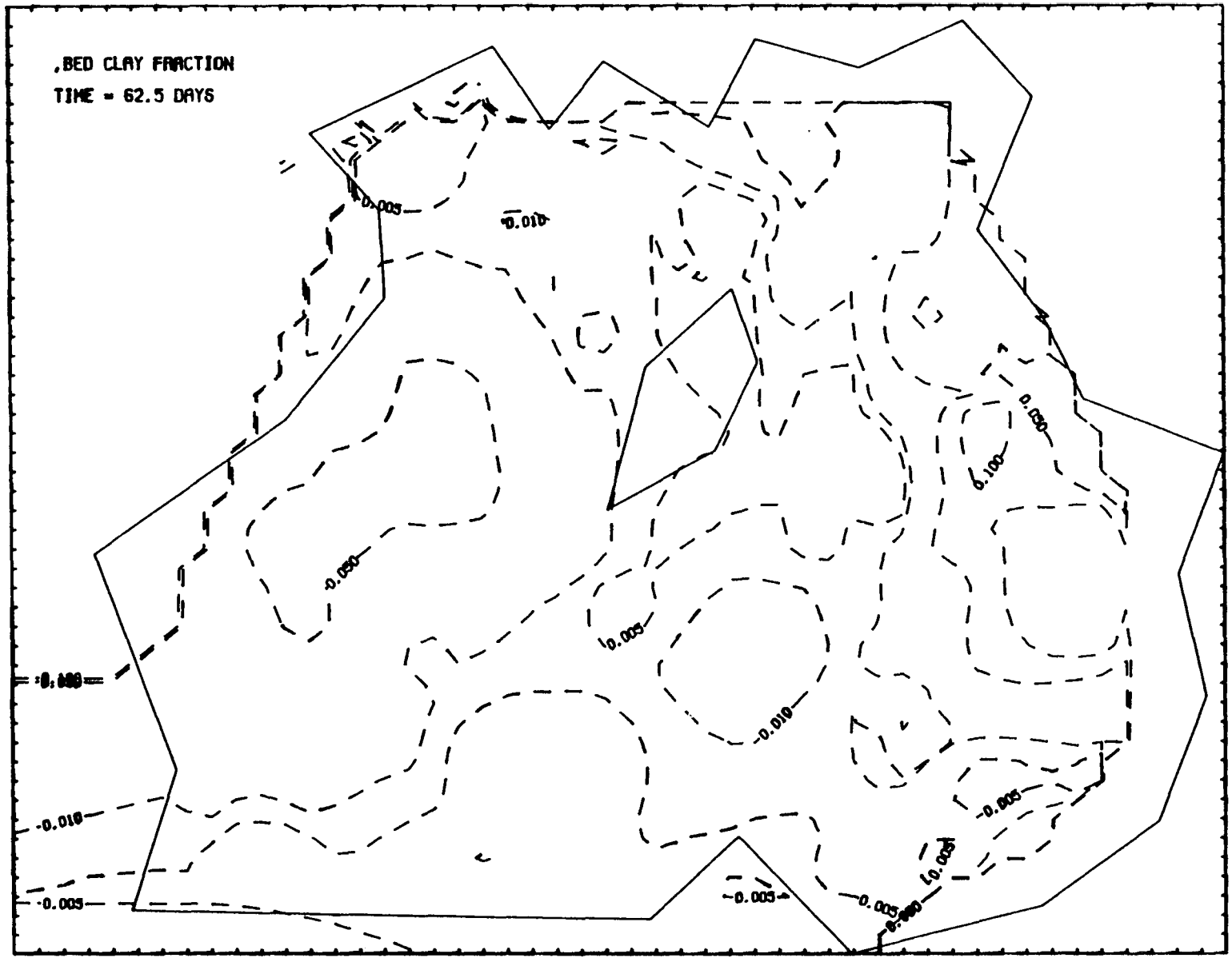

FIGURE 4.60. Computed Distribution of Bed Clay Fraction in the Top 10-cm Bed Layer After 62.5 Days of Simulation

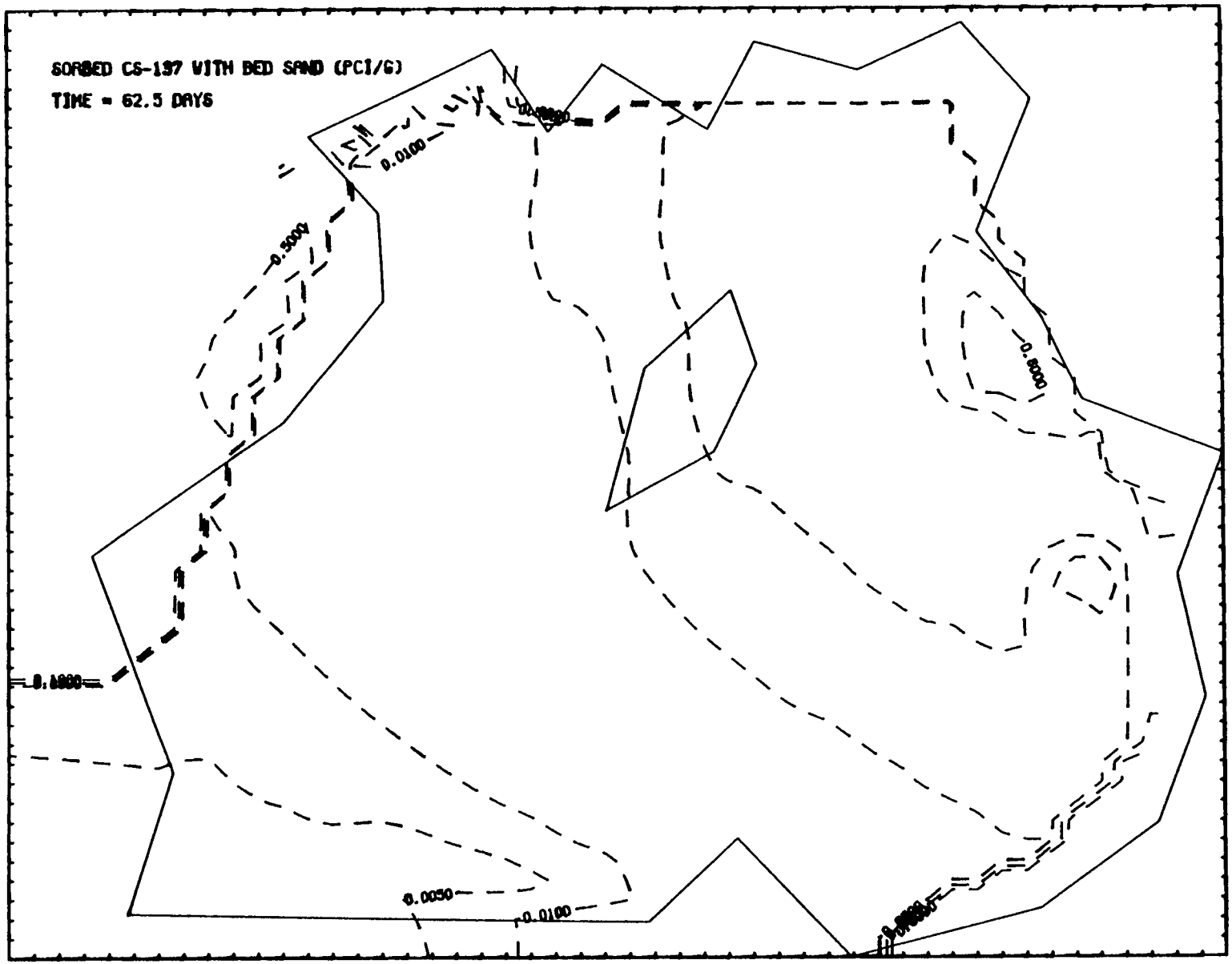

FIGURE 4.61. Computed Concentration of ^{137}Cs Sorbed by Bed Sand in the Top 10-cm Bed Layer After 62.5 Days of Simulation

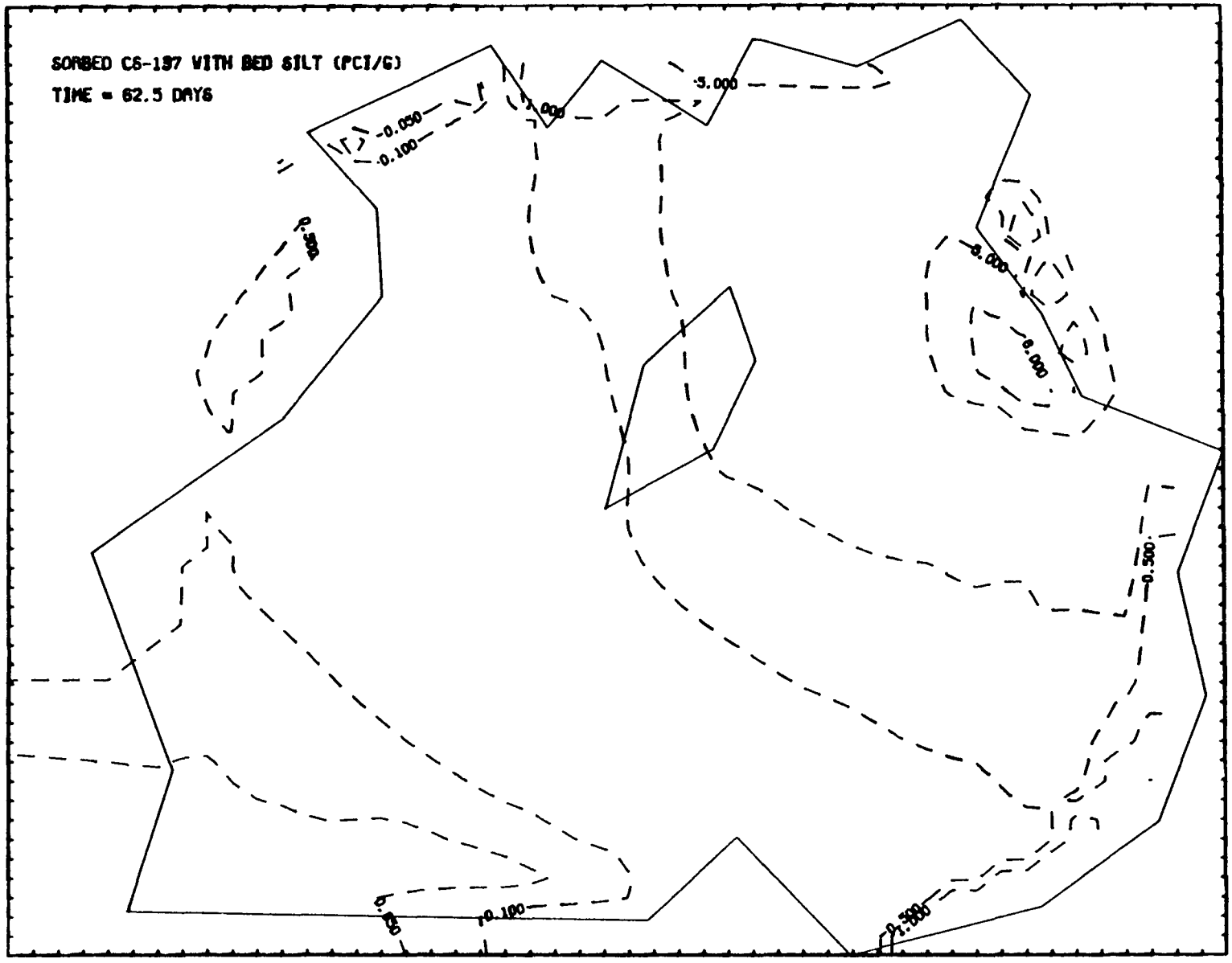

FIGURE 4.62. Computed Concentration of ^{137}Cs Sorbed by Bed silt in the Top 10-cm Bed Layer After 62.5 Days of Simulation

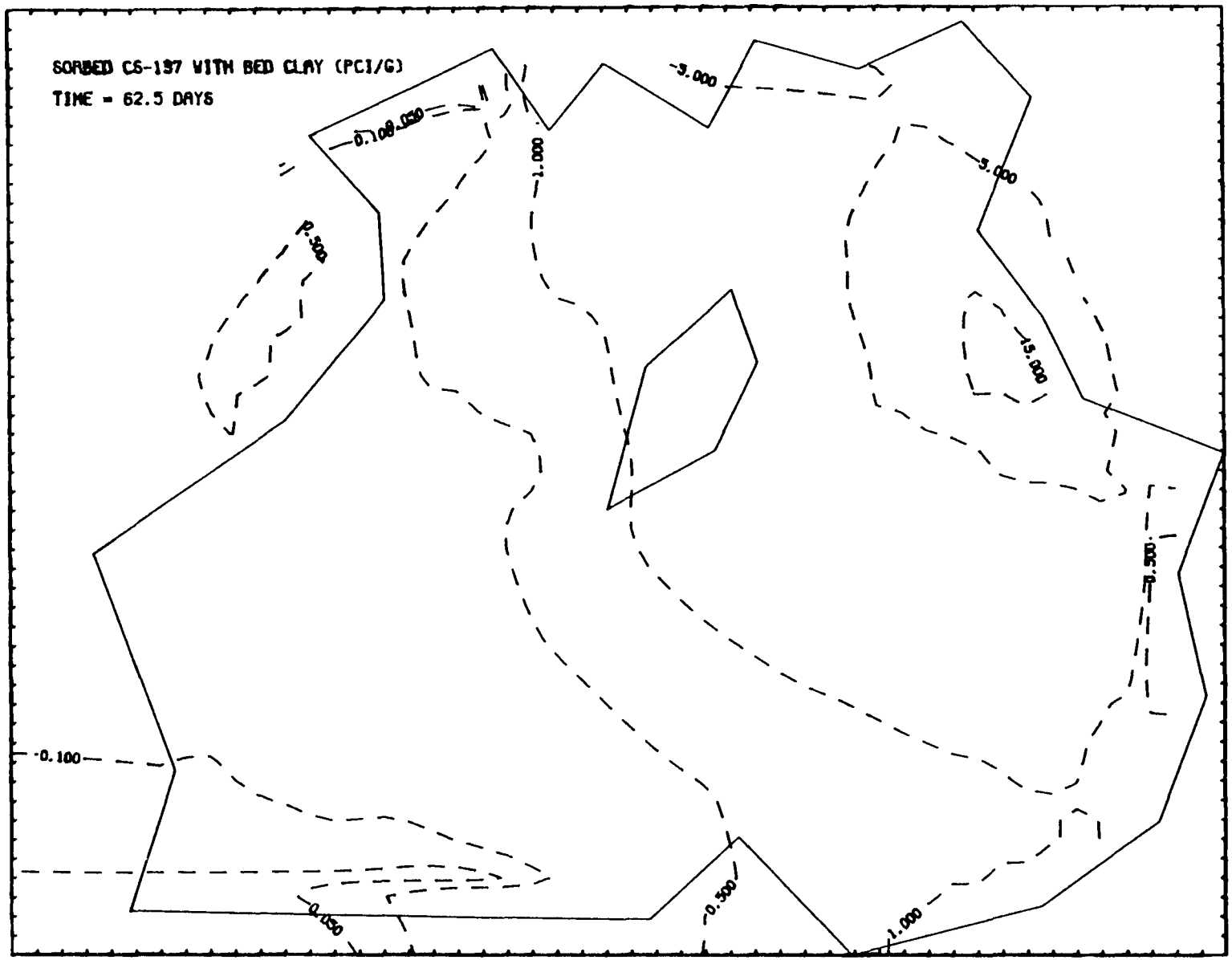

FIGURE 4.63. Computed Concentration of ^{137}Cs Sorbed by Bed Clay in the Top 10-cm Bed Layer After 62.5 Days of Simulation

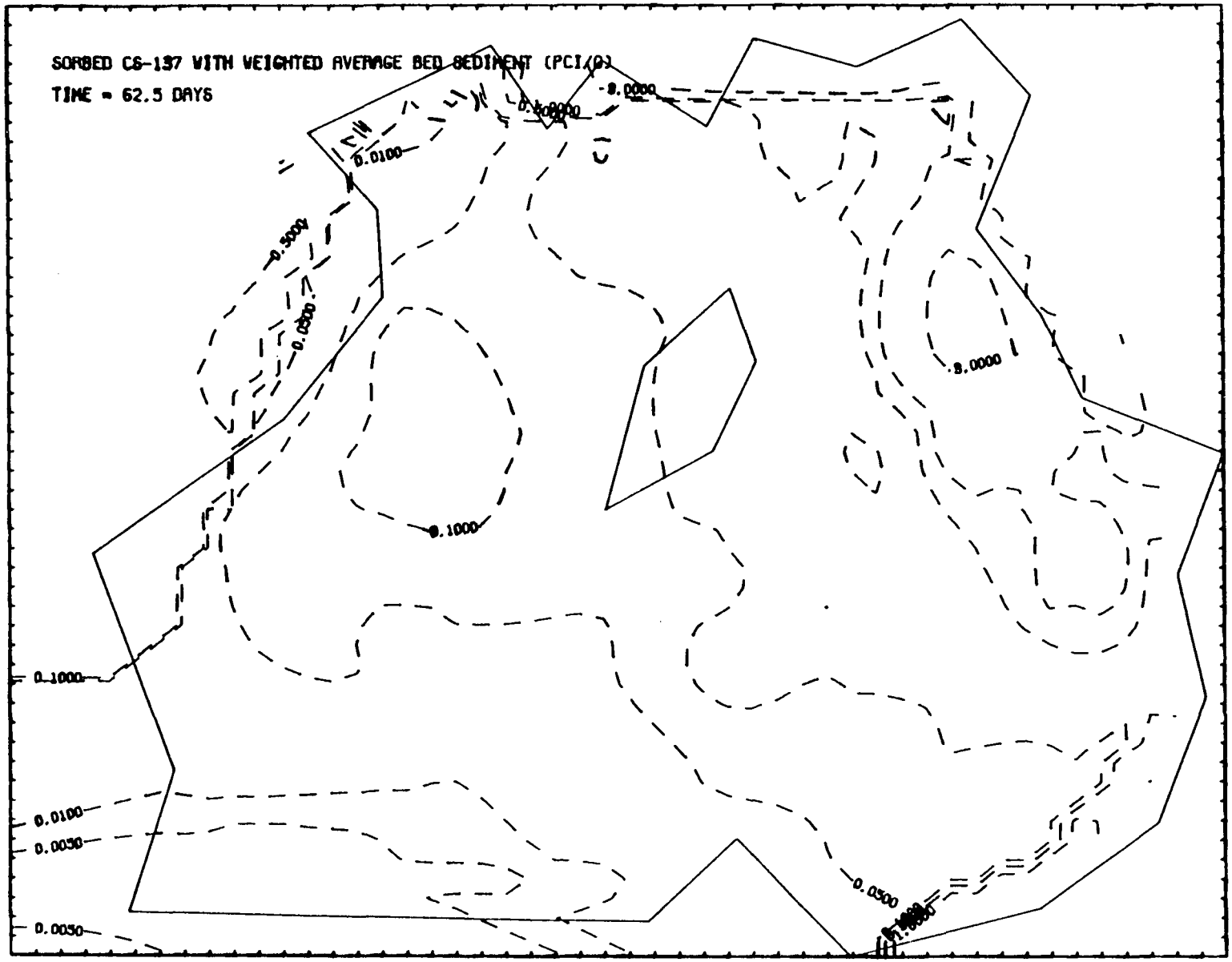

FIGURE 4.64. Computed Concentration of ^{137}Cs Sorbed by Bed Sand by Weighted Average Bed Sediment

REFERENCES

Bowden, K. F. 1955. Physical Oceanography of the Irish Sea. Ministry of Agriculture, Fisheries and Food, Fishery Investigations, Series II, Vol. XVIII, No. 8, Her Majestry's Stationary Office, London, United Kingdom.

Bretschedier, C. L. and R. O. Reid. 1953. "Change in Wave Height Due to Bottom Friction, Percolation and Refraction." 34th Annual Meeting of American Geophysics Union.

Daily, J. W. and D. R. F. Harleman. 1966. Fluid Dynamics. Addison Wesley Publishing Co., Inc., New York, New York.

Dawson, G. W. 1978. The Feasibility of Mitigating Kepone Contamination in the James River Basin. Prepared by Pacific Northwest Laboratory, for the Environmental Protection Agency.

Desai, C. S. and J. F. Abel. 1972. Introduction to the Finite Element Method, A Numerical Method for Engineering Analysis. Van Nostrand Reinhold Co., New York, New York.

Dobson, R. S. 1967. Some Applications of a Digital Computer to Hydraulic Engineering Problems. Technical Report No. 80, Stanford University, Department of Civil Engineering, Stanford, California.

Ecker, R. M. and H. M. Degraca. 1974. "Sediment Transport - Coast of Northern California," Preprint 2141 from ASCE National Water Resources Engineering Meeting, January 21-25, 1974. Los Angeles, California.

Einstein, H. A. 1972. "Sediment Transport by Wave Action." In Proceedings of 13th Conference on Coastal Engineering, American Society of Civil Engineers.

Eraslan, A. H. 1975. A Transient, Two-Dimensional, Discrete - Element, Far-Field Model for Thermal Impact analysis of Power Plant Discharges in Mathemaical Model and the Results of an Application. ORNL-4940, Oak Ridge National Laboratory, Oak Ridge, TN.

Eraslan, A. H. 1977. Development of a Unified Transport Approach for the Assessment of Power-Plant Impact. ORNL/NUREG/TM-89, Oak Ridge National Laboratory, Oak Ridge, TN.

Fischer, H. B. 1967. "The Mechanics of Dispersion in Natural Streams," Journal of the Hydraulics Division 92(HY6):187-216.

Hetherington, J. A. 1976. "The Behavior of Plutonium Nuclides in the Irish Sea." In Environmental Toxicity of Aquatic Radionuclides: Models and Mechanisms, eds. M. W. Miller and J. N. Stannard. p. 81-106, Ann Arbor Science, Ann Arbor, Michigan.

Hetherington, J. A. 1976. Radioactivity in Surface and Coastal Waters of the British Isles, 1974. Ministry of Agriculture, Fisheries and Food, Directorate of Fisheries Research, Lowestoft, United Kingdom.

Hetherington, J. A. and D. F. Jefferies. 1974. "The Distribution of Some Fission Product Radionuclides in Sea and Estuarine Sediments." Netherlands Journal of Sea Research, 8(4):319-338.

Ippen, A. T. (ed.) 1964. Estuary and Coastline Hydrodynamics. McGraw-Hill Book Company, Inc., New York, New York.

Jefferies, D. F. 1968. "Fission-Product Radionuclides in Sediments from the Northeast Irish Sea." Helgolander wiss. Meeresunters, 17:280-290.

Jefferies, D. F., A. Preston and A. K. Steele. 1973. "Distribution of Cesium-137 in British Coastal Waters." Marine Pollution Bulletin, Vol. 4, No. 8, pp. 118-122.

Komar, P. D. 1977. "Modeling of Sand Transport on Beaches and the Resulting Shoreline Evolution." In The Sea. Vol. 6, pp. 499-513, John Wiley and Sons, New York.

Krone, R. B. 1962. Flume Studies of the Transport of Sediment in Estuarial Shoaling Processes, Hydraulic Engineering Laboratory and Sanitary Engineering Research Laboratory, University of California at Berkeley, California.

Leendertse, J. J. 1970. "A Water Quality Simulation Model for Well Mixed Estuaries and Coastal Seas." Principles of Computation. Vol. I, RM-6230-RC.

Leendertse, J. J., R. C. Alexander and S. L. Liu. 1973. "A Three-Dimensional Model for Estuaries and Coastal Seas." In Principles of Computation, Vol. I, R-147-OWPR, The Rand Corporation.

Liang, S. S. and H. Wang. 1973. Sediment Transport in Random Waves. Technical Report No. 26, University of Delaware, College of Marine Studies.

Livingston, H. D., and V. T. Bowen. 1976. Contrasts Between Marine and Freshwater Biological Interactions of Plutonium and Americium. HASL-315, Health and Safety Laboratory Environmental Quarterly, U.S. Energy Research and Development Administration, Washington, D.C.

Mauchline, J. and W. L. Templeton. 1963. "Dispersion in the Irish Sea of the Radioactive Liquid Effluent from Windscale Works of the U.K. Atomic Energy Authority," Nature 198(4981):623-626.

Nevissi, A., and W. R. Schell. 1975. "Efficiency of a Large Volume Water Sampler for Some Radionuclides in Salt and Fresh Water." In Proc. 4th Nat. Symp. on Radiation Ecology, Oregon State University, Corvallis, OR.

Noshkin, V. E., and V. T. Bowen. 1973. "Concentrations and Distributions of Long-Lived Fallout Radionuclides in Open Ocean Sediments." In Radioactive Contamination of the Marine Environment, pp. 671-686, IAEA, Vienna, Austria.

Onishi, Y. 1981. "Sediment-Contaminant Transport Model," Journal of the Hydraulic Division 107(HY9):1089-1107.

Onishi, Y., E. M. Arnold and D. W. Meyer. 1979. Modified Finite Element Transport Model, FETRA, for Sediment and Radionuclides Migration in Open Coastal Waters. NUREG/CR-1026 (PNL-3114). Nuclear Regulatory Commission, Washington, D.C.

Onishi, Y., R. J. Serne, E. M. Arnold, C. E. Cowan and F. L. Thompson. 1981. Critical Review: Radionuclide Transport, Sediment Transport, and Water Quality Mathematical Modeling; and Radionuclide Adsorption/Desorption Mechanisms. NUREG/CR-1322 (PNL-2901), Nuclear Regulatory Commission, Washington, D.C.

Onishi, Y. and D. S. Trent. 1982. Mathematical Simulation of Sediment and Radionuclide Transport in Estuaries--Testing of Three-Dimensional Radionuclide Transport Modeling for the Hudson River Estuary, New York. NUREG/CR-2423 (PNL-4109), Nuclear Regulatory Commission, Washington, D.C.

Onishi, Y., S. B. Yabusaki and C. T. Kincaid. 1982. "Performance Testing of the Sediment-Contaminant Transport Model, SERATRA," In Proceedings of the conference on Applying Research to Hydraulic Practice, pp. 623-632, ASCE, Jackson, Mississippi.

Partheniades, E. 1962. A Study of Erosion and Deposition of Cohesive Soils in Salt Water. Dissertation presented to the University of California, at Berkeley, California.

Pentreath, R. J., J. B. Lovett, D. F. Jefferies, D. S. Woodhead, J. W. Talbot, and N. T. Mitchell. 1983. "The Impact on Public Radiation Exposure of Transuranium Nuclide Discho-sed in Liquid Wastes from Fuel Element Reprocessing at Sellafield, United Kingdom," In Proceedings of the International Conference on Radioactive Waste Management, IAEA-CN-43, International Atomic Energy Agency, Seattle, Washington.

Robinson, I. S. 1979. "The Tidal Dynamics of the Irish and Celtic Seas." Geophysical Journal of the Royal Astronomical Society 56(1):159-197.

Sayre, W. W. 1966. "Dispersion of Silt Particles in Open Channel Flow." Journal of the Hydraulics Division 92(HY3):1009-1038.

Schell, W. R. 1977. "Concentration, Physico-Chemical States and Mean Residence Time of ^{210}Pb and ^{210}Po in Marine and Estuarine Waters." Geochimica et Geophysica Acta, 41:1019-1031.

Schlichting, H. 1968. Boundary-Layer Theory. McGraw Hill Book Co.

Smith, T. J., W. R. Parker and R. Kirby. 1980. Sedimentation Studies Relevant to Low-Level Radioactive Dispersal in the Irish Sea. Part I, Radionuclides in Marine Sediments. Report No. 110, N.E.R.C. Institute of Oceanographic Sciences, Godalming, Surrey.

Sverdrup, H. U. and W. H. Munk. 1947. Wind, Sea and Swell; Theory of Relationships for Forecasting. Pub. No. 601, U.S. Navy Hydrographic Office, Washington D.C.

U.S. Army Corps of Engineers, Beach Erosion Board. 1962. Waves in Inland Reservoirs, Summary Report on Civil Works Investigation Projects CW-164 and CW-165. Tech. Memo No. 132.

U.S. Army Corps of Engineers. 1973. Shore Protection Manual, Vol. 3. Coastal Engineering Research Center.

U.S. Department of Commerce. 1967. Tide Tables 1968, High and Low Water Predictions, Europe and West Coast of Africa, Environmental Science Services Administration, Coast and Geodetic Survey, Rockville, Maryland.

U.S. Department of Commerce. 1973. Tide Tables 1973, High and Low Water Predictions, Europe and West Coast of Africa, National Oceanic and Atmospheric Administration, National Ocean Survey, Rockville, Maryland..

U.S. Environmental Protection Agency. 1978. Kepone Mitigation Project Report. Division of Standards and Criteria, Office of Water and Hazardous Materials, Washington, D.C.

Vanoni, V. A., ed. 1975. "Sedimentation Engineering," ASCE Task Committee for the Presentation of the Manual on Sedimentation of the Sedimentation Committee of the Hydraulics Division, American Society of Civil Engineers.

Wang, J. D. and J. J. Connor. 1975. Mathematical Modeling of Near Coastal Circulation. Report No.200, R. M. Parsons Laboratory, Massachusetts Institute of Technology, Department of Civil Engineering, Cambridge, Massachusetts.

Williams, W. J., R. Kirby, T. J. Smith and W. R. Parker. 1981. Sedimentation Studies Relevant to Low-Level Radioactive Effluent in the Irish Sea; Part II, Sea Bed Morphology, Sediments and Shallow Subbottom Stratigraphy of the Eastern Irish Sea, Report No. 120, N.E.R.C. Institute of Oceanographic Sciences, Godalming, Surrey.

DISTRIBUTION

No. of Copies

OFFSITE

U.S. Nuclear Regulatory Commission
Division of Technical Information and Document Control
7920 Norfolk Avenue
Bethesda, MD 20014

P. R. Reed
U.S. Nuclear Regulatory Commission
Washington, DC 20555

R. B. Codell
U.S. Nuclear Regulatory Commission
Washington, DC 20555

F. Swanberg
Office of Nuclear Regulatory Research
U.S. Nuclear Regulatory Commission
Washington, DC 20555

E. F. Conti
Office of Nuclear Regulatory Research
U.S. Nuclear Regulatory Commission
Washington, DC 20555

R. D. Smith
Office of Nuclear Material Safety and Safeguard
U.S. Nuclear Regulatory Commission
Washington, DC 20555

No. of Copies

J. H. Kittel
Argonne National Laboratory
9700 S. Cass Avenue
Argonne, IL 60439

Battelle Memorial Institute
Office of Nuclear Waste Isolation
Attn: Beverly Rawles
505 King Avenue
Columbus, OH 43201

Irving Joseph
Bechtel Corporation
50 Beale Street
San Francisco, CA 94105

G. H. Jirka
Department of Environmental Engineering
Cornell University
Ithaca, NY 14850

P. F. Ricci
Electric Power Research Institute
P.O. Box 10412
Palo Alto, CA 94303

W. Hanson
Mail Stop 495
Los Alamos National Laboratory
P.O. Box 1663
Los Alamos, NM 87545

G. L. DePoorter
Los Alamos National Laboratory
Los Alamos, NM 87545

No. of
Copies

J. J. Connor
Department of Civil Engineering
Massachusetts Institute of
Technology
Cambridge, MA 02139

J. J. Leendertse
RAND Corp.
Santa Monica, CA 90406

G. Setlock
Rockwell International
Rockly Flats
P.O. Box 464
Golden, OH 80401

J. R. Wiley
Savannah River Laboratory
Aiken, SC 29801

G. Zweig
322 Warren Hall
School of Public Health
University of California
Berkeley, CA 94720

E. R. Holley
Department of Civil Engineering
University of Illinois
Urbana, IL 61801

J. F. Kennedy
Institute of Hydraulic
Research
University of Iowa
Iowa City, IA 52241

E. F. Gloyna
College of Engineering
University of Texas at Austin
Austin, TX 78705

D. N. Edgington
Center of Great Lake Studies
University of Wisconsin
P.O. Box 413
Milwaukee, WI 53201

No. of
Copies

C. V. Alonso
U.S. Department of Agriculture
Sedimentation Laboratory
Southern Region
Agriculture Research Center
P.O. Box 1157
Oxford, MI 38655

J. Lunin
U.S. Department of Agriculture
Science and Education
Administration
Agriculture Research
National Program Staff
Beltsville, MD 20705

H. Pionke
U.S. Department of Agriculture
Northeast Watershed Research
Laboratory
110 Research Building A
Pennsylvania State University
University Park, PA 10802

R. D. Wauchope
U.S. Department of Agriculture
Stoneville, MS 38776

R. A. Baker
U.S. Geologic Survey
National Space Technology
Laboratories
NSTL Station, MS 39529

K. Bencala
U.S. Geological Survey
MS/96
345 Middlefield Rd.
Menlo Park, CA 94025

N. Yotsukura
U.S. Geological Survey
Water Resources Division
National Center
12201 Sunrise Valley Dr.
Reston, VA 22092

No. of
Copies

ONSITE

50 Pacific Northwest Laboratory

D. B. Cearlock
D. W. Dragnich
P. C. Hays
E. A. Jenne
Y. Onishi (32)
W. L. Templeton
F. L. Thompson (4)
D. S. Trent
L. L. Wendell
Technical Information (5)
Publishing Coordination (2)